Modeling Membrane Dynamics on the Level of Organelles

Dissertation

zur Erlangung des Grades
“Doktor der Naturwissenschaften”
am Fachbereich für Physik, Mathematik und Informatik
der Johannes Gutenberg-Universität in Mainz

vorgelegt von

Maike Jung, geb. Lauf

geboren in Dernbach

Mainz, den 13. Januar 2021

Veröffentlichungen welche Teile dieser Dissertation beeinhalten:

"Energetics and Stability of Branched and Tubular Membrane Structures",
Maike Jung, Gerhard Jung, Hiroshi Noguchi und Friederike Schmid,
Manuskript in Bearbeitung

Zusammenfassung

Entwicklung eines Modells zur Beschreibung der Membrandynamik auf der Ebene von Organellen

Biomembranen sind allgegenwärtig in Zellen. Sie umhüllen nicht nur Organellen, sondern bilden auch hochdynamische, komplexe Strukturen wie z.B. tubuläre, schlauchartige Ausstülpungen oder verzweigte Netzwerke. Es ist eine herausfordernde Aufgabe, die Dynamik dieser Membranen zu untersuchen, da deren Deformationsprozesse auf relativ großen Zeit- und Längenskalen ablaufen. In dieser Arbeit werden dynamische Änderungen der Form von Membranen mithilfe von Computersimulationen betrachtet. Das verwendete Simulationsmodell ist ein 'dynamisch-trianguliertes' (dynamically-triangulated) Membranmodell, welches auf der Kontinuumbeschreibung des Helfrich-Hamiltonians basiert. Dieses Modell ermöglicht es, größere Zeit- und Längenskalen zu untersuchen als mit atomistischen oder 'vergröberten' (coarse-grained) Simulationsmethoden.

Im ersten Teil der Arbeit wird das Modell dazu verwendet, tubuläre Ausstülpungen von Vesikeln zu untersuchen, welche durch das Anlegen einer externen Kraft erzeugt werden. Die Ergebnisse werden anschließend mit theoretischen Näherungen und numerischen Energieminimierungen des Helfrich-Hamiltonians verglichen, welche sich die Rotationssymmetrie des Systems zunutze machen. Dieser Vergleich zeigt eine gute Übereinstimmung zwischen Theorie und Simulationen. Zusätzlich untersuchen wir die Bildung und Verschmelzung mehrerer tubulärer Ausstülpungen an Vesikeln. Im zweiten Teil der Arbeit liegt der Schwerpunkt auf der Bildung und Stabilität rein tubulärer und verzweigter tubulärer Strukturen, die ebenfalls durch externe Kräfte erzeugt werden. Wir beobachten, dass sobald die externe Kraft aufgehoben wird, beide Systeme instabil sind und sich zurück bilden. Dies deutet darauf hin, dass es in der Natur weitere Mechanismen zur Stabilisierung geben muss. Wir können zeigen, dass tubuläre Strukturen in der Tat metastabil sind, wenn das Oberfläche-zu-Volumen-Verhältnis fixiert wird. Tatsächlich ist dies eine natürlich vorgegebene Bedingung für geschlossene, undurchlässige Membranen. Verzweigte Strukturen können so allerdings nicht stabilisiert werden, was auf einen weiteren Stabilisierungsmechanismus hindeutet. Ein Mechanismus, welchen wir erfolgreich anwenden konnten, ist es, die Gesamtkrümmung der Strukturen zu fixieren.

Diese Ergebnisse zeigen, dass tubuläre Netzwerke, die in biologischen Zellen beobachtet werden, entweder durch die Verankerung an Organellen oder Filamenten, oder durch die Vorgabe der Gesamtkrümmung stabilisiert werden können. Letzteres kann auf krümmungsinduzierenden Proteinen oder auf einer Asymmetrie der beiden Flächen der Lipiddoppelschicht beruhen. Computersimulationen und insbesondere Kontinuum-Modelle sind demnach ein sehr wertvolles und nützlichen Mittel zur Interpretation und Ergänzung experimenteller Beobachtungen von Biomembranen.

Abstract

Modeling Membrane Dynamics on the Level of Organelles

Biological membranes are omnipresent in cells, not only enclosing organelles but also in the form of highly dynamical structures such as tubular protrusions or complex branched networks. Investigating the dynamics of these membranes can be a challenging task in both experiments and computer simulations, because of the time and length scales that need to be accessed. In this work, conformational membrane changes are investigated by performing computer simulations using a dynamically-triangulated membrane model, which is based on a continuum description of the Helfrich Hamiltonian. This description is relatively general and allows to access larger length and time scales than in typical atomistic or coarse-grained simulations.

In the first part of this thesis, the model is applied to study the formation of tubular structures from vesicles by pulling with an external force. Our findings are compared to theoretical approximations and minimal-energy solutions of the Helfrich Hamiltonian, exploiting the rotational symmetry of the structures. We find a very good agreement between the shapes found in theory and simulations. We also simulate the formation and coalescence of several tubes protruding from a vesicle. In the second part, we focus on the formation, energetics and stability of purely tubular and branched structures under the action of an external field and different global constraints. We find that both structures are unstable, when releasing the external force, which means that in nature other types of stabilization mechanisms must be present. We can show that when fixing the area to volume ratio of the structure, which is a natural constraint for closed impermeable membranes, tubes are metastable, while branches are still unstable. To stabilize these branches, an additional constraint therefore has to be set. One possibility which we successfully applied in this thesis is fixing the overall curvature of the system.

These findings show that tubular networks observed in biological cells need to be stabilized by either anchoring to organelles or filaments, or by controlling the overall curvature through curvature-inducing proteins or an area difference between the two monolayers of the lipid bilayer. Computer simulations of biological membranes and in particular continuum models thus provide a very valuable and useful tool for interpreting and complementing experimental observations.

Contents

1

Introduction

Biological cells, which are the building blocks of all living organisms, and most of their intracellular components are separated by membranes. These membranes are not only an important selective barrier between different parts of the cell, but also serve as a platform for biological and chemical reactions. A detailed understanding of membranes is therefore essential for a comprehensive understanding of all living organisms. While the static properties of membranes have been studied extensively and are well understood, their dynamic properties still raise many questions.

A typical biological membrane consists of a lipid bilayer in which proteins are embedded. The lipid and protein composition can vary greatly across the membrane, depending on the location and function of the specific membrane region. On a microscopic scale it is possible to simulate membranes in full detail, using ab-inito or atomistic simulations. In atomistic simulations all the atoms of the lipids and proteins and their interactions can be modeled explicitly and their dynamics can be investigated. Atomistic simulations are, however, computationally very expensive and can only be applied to small systems. With current state of the art simulation models, system sizes of $10 - 50\,\mathrm{nm}$ can be simulated for about $100 - 1000\,\mathrm{ns}$.[1] To go to larger scales, coarse-grained models have to be employed. In these models the degrees of freedom are reduced by grouping together several atoms or molecules to one functional unit. Decreasing the degrees of freedom can significantly reduce computational costs and therefore allow to investigate larger systems on longer timescales. However, even such mesoscopic coarse-grained models are still a long way from modeling entire cell organelles with a diameter of $\sim 10\,\mu\mathrm{m}$ and more than 10^9 lipids.

The aim of this thesis is to model and describe dynamical properties of membranes on even larger scales and model systems up to the size of entire cell organelles, using a continuum description of the membrane. Special focus lies on the formation of tubular structures and the branching of tubes. Tubular and branched structures have been observed experimentally and are omnipresent in cells. Some organelles, for example the endoplasmic reticulum, are made up almost entirely of a network of tubular and sheet-like structures. Other organelles like chloroplasts have thin tubular structures protruding from them. In the case of the chloroplasts, these protrusions dynamically form and retract and can become very long and narrow. The formation mechanism and function of these stromules is still a huge point of speculation. Our model is therefore used to investigate such structures with particular focus on their energetics and stability.

Mathematically, our model is based on the Helfrich formalism, in which a membrane is described as a two-dimensional surface in three-dimensional space, using methods from differential geometry. The model is rather general and does not contain information about the exact lipid and protein composition. Instead this information is condensed and represented by only a few model parameters, e.g. the bending rigidity of the membrane. In general this model cannot be solved analytically. One therefore requires a discretized version and relies on numerical solvers. For performing the simulations in this work, a dynamically-triangulated membrane model is employed. In this model the surface is discretized by vertices, which are connected by bonds, forming a triangular network structure. This is an efficient way to model closed vesicular structures and in addition allows to have control over the area and volume of the system.

The first objective of this work was to study the formation of tubular structures due to an external pulling force. In cells such a force could, e.g., be induced by motor proteins that pull on the membrane. To model this behavior, closed spherical vesicles were simulated and an external force was applied to one or more points of the membrane surface, pointing away from the vesicle center, thus deforming it. For large forces, tubular structures protruding from the vesicle could be observed. Their lengths and radii were analyzed and agree well with theoretical predictions for the equilibrium radius of a perfectly symmetric tube with fixed area. In addition, we have numerically determined the minimal-energy solutions of the system using shooting methods. These numerical solutions do not give any information about the tube formation process, which has been studied using the simulation model, but they allow to determine the final stable configuration of a rotationally symmetric tube-forming vesicle with an external pulling force. These results were compared to the computer simulations and we found nearly perfect agreement.

The second aim of this thesis was the investigation of branched structures, with particular emphasis on their stability and their energetics. First, coalescence of the tubular structures formed above was investigated. It could be observed that at a certain angle, which depends on the tube radius and the area to volume ratio of the system, merging of the tubes occurs. Then branched structures, i.e., structures with three tubular arms, were simulated and compared to a simple tubular structure. The simulations indicate that a branched structure is energetically even more favorable than a simple tube, but it is not stable in our basic model. The reason is that basically all branched structures are able to transform into a stromatocyte, which is known to be the global energy minimum for all structures with such a low volume to area ratio. This implies that branches have to be stabilized by other additional mechanisms, e.g. curvature inducing proteins, filaments which serve as scaffolds or an area difference between the individual layers of the lipid bilayer, which induces curvature. We modeled the latter mechanism by keeping the overall curvature of the system fixed, which indeed stabilizes the branched structures.

Additionally, vesicle motion induced by tubule generation was investigated. This model is motivated by the experimental observation of a correlation between long jumps in the movement patterns of chloroplasts and the number stromules. For this a simple model of a small vesicle confined by a big outer sphere was devised. Tubes protruding from the vesicle exert an external force and pull on the vesicle, creating a motion that is remotely connected to a continuous-time random walk.

The first part of this thesis is a brief introduction to biological systems and computer simulations. In Chapter 2 the composition of biological membranes and their properties are discussed. Then an introduction to computer simulations and simulation methods is given in Chapter 3, including a description of the dynamically-triangulated membrane model and the necessary mathematical background.

In the second part the simulation procedure is described. Results for vesicular tube formation due to an external force are presented in Chapter 4. In Chapter 5 these results are complemented by minimal-energy solutions of the Helfrich Hamiltonian. Both are compared to theoretical predictions and data from the literature.

In the next part of this thesis the focus lies on branched structures. First the coalescence of tubes is investigated in Chapter 6. Then branch and tubular structures are compared in Chapter 7 and the transition between them is simulated. Finally, the energies of the systems are analyzed to determine the energy of the neck structure, i.e. the region where the three tubes of the branch meet, and thus draw important conclusions on the stability of branched vesicular structures. Finally, in Chapter 8, the thesis is concluded with a summary and an outlook on possible applications of our results and on further studies that could be performed with the membrane simulation model. In addition, we present a basic model, which can be used to simulate vesicle motion due to tubule generation in Appendix C.

2

Biological Membranes

In this chapter a brief introduction to cell organelles and biological membranes is given. First, the functions and shapes of cell organelles are described, followed by the properties of biological membranes and important aspects that need to be considered for modeling them. Finally, a summary of what is known about tubular and branched structures in cells is given.

2.1 Biological Background

2.1.1 Cells and Organelles

Cells are the basic structural and functional units of all living organisms. They are therefore often referred to as their building blocks. Their sizes range from $1 - 100\,\mu\text{m}$ and depending on the cell type they contain various different organelles. Organelles are separated regions within the cell that have various specific functions

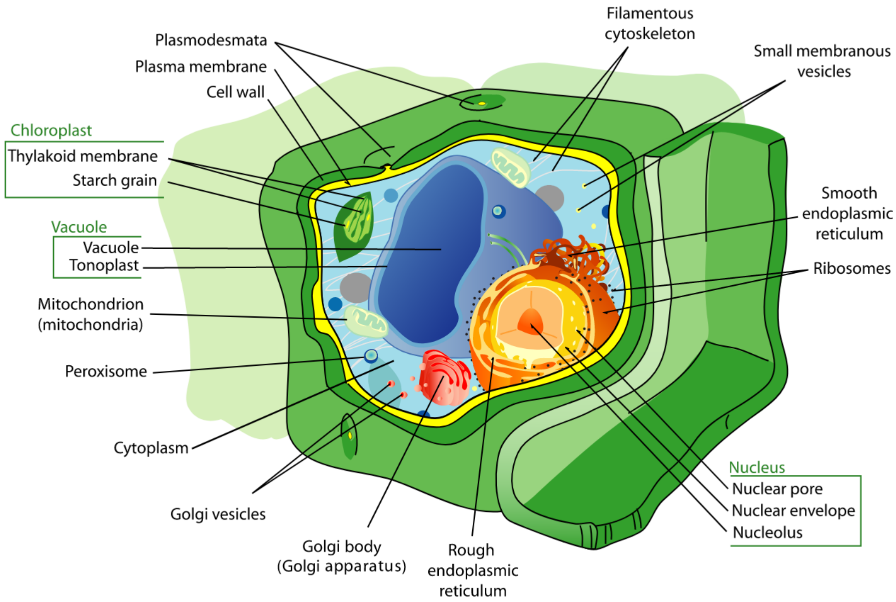

Figure 2.1: Illustration of the typical structure of a plant cell. It contains various different organelles, which all have specific functions. Taken from Ref. 2.

and most of these organelles are enclosed by a biological membrane. A sketch of a typical plant cell and its organelles is shown in Figure 2.1.

Organelles not just have various different functions, they also have different shapes and different sizes, all in the µm range. The nucleus is usually the biggest organelle and contains the DNA. Mitochondria are oval organelles that provide the cell with energy, whereas the endoplasmic reticulum is an interconnected network of tubular structures and sacs, where protein folding takes place and which transports proteins in vesicles. The entire cell is interspersed with the cytoskeleton, a dynamic network of filaments, which gives the cell its shape and mechanical stability, but is also involved in transport and signaling processes. In cells there are many more organelles, the above mentioned are just a few examples. A more detailed description can be found in standard textbooks, e.g. Ref. 3.

2.1.2 Biological Membranes

Most cells and organelles are enclosed by membranes. Cell membranes are usually referred to as plasma membranes, whereas the membranes of organelles are referred to as biological membranes. Membranes not just serve as a selective barrier between cells or organelles and their surroundings, they are also a platform for biological and chemical reactions. All membranes consist of a lipid bilayer in which proteins are embedded.

Lipids are amphiphilic molecules that have a hydrophilic polar head group and a hydrophobic non-polar tail group. If immersed in water, they automatically form a bilayer, with the polar heads oriented towards the water and the tails oriented towards each other, as shown in Figure 2.2. This is the energetically most favorable arrangement. Since the cytosol, which fills up the interior of the cells, is an aqueous solution, this formation automatically happens within the cell.

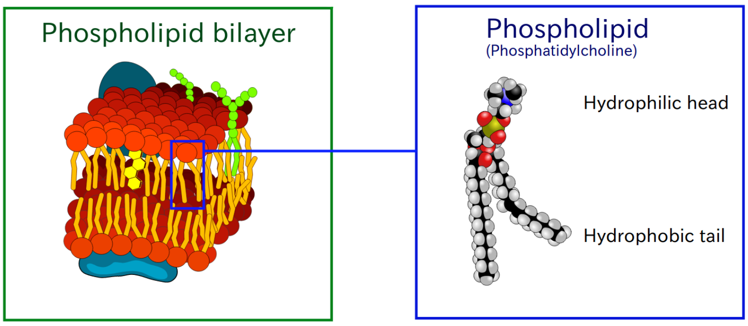

Figure 2.2: Sketch of a typical cell membrane. The lipids form a bilayer in which proteins (blue) and other molecular structures are embedded (left).
Composition of a phospholipd (right), with its hydorphilic head and hydrophobic tail. Adapted from Ref. 4.

A pure lipid bilayer has a thickness of about 5 nm, biological membranes a thickness of about $7-10\,\text{nm}$ due to the embedded proteins.[3] A biological membrane typically consist of many different types of lipids and proteins. The composition varies greatly across the different organelles and even within the organelles themselves, depending on the function of the specific membrane region.

A membrane patch of $1\,\mu\text{m}^2$ contains on the order of 10^6 lipids,[3] which is one of the reasons, why computer simulations of biological membranes can be very challenging. Another very important aspect of biological membranes is that they behave as two-dimensional fluids. This means that lipids can freely stream within their side of the bilayer. Neighboring lipids exchange places about 10^7 times per second. The switching of lipids between different layers, called flip-flop, on the other hand is greatly suppressed.

2.1.3 Branched and Tubular Structures

In biological cells various membrane network structures have been observed and found to be abundant, especially in the Golgi complex[7] and the endoplasmic reticulum.[8] Examples of such a network structure are visualized in Figure 2.3.[5;6] Both a pure network structure, c.f. Figure 2.3a, and a system in which the tubular structures interconnect individual invaginations, c.f. Figure 2.3b, are shown. Interestingly, it can also be observed that the branches of the network typically meet at Y-junctions with an angle of 120° between the individual tubes. This can be explained by the fact that the network can in this way minimize the total tube length and hence the energy of the system. This can be shown mathematically and

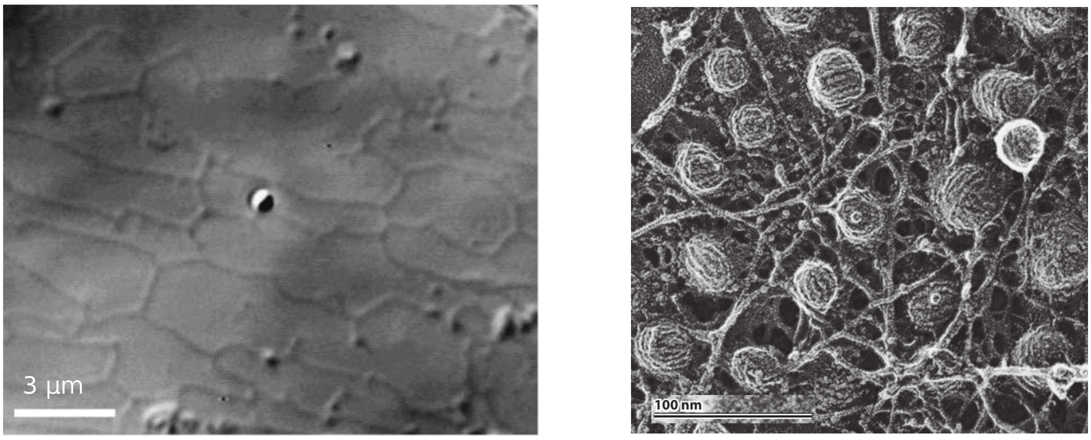

(a) The tubular mesh is stabilized by an underlying network of microtubules. The branches typically meet at trigonal vertices with 120° angles. The image was taken using DIC microscopy. Adapted from Ref. 5.

(b) Tubular connections between different caveolae, which are invaginations of the plasma membrane, formed by caveolin, a curvature-inducing protein. Adapted from Ref. 6.

Figure 2.3: Examples of typical tubular membrane networks.

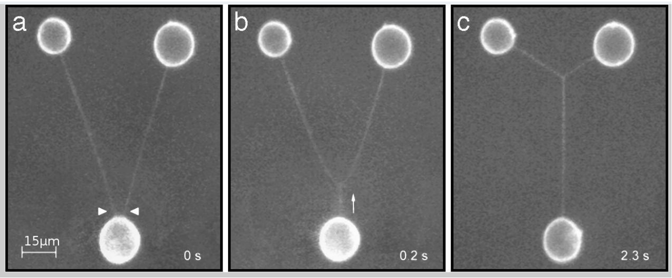

(a) Fluorescence micrographs of the time evolution of a surfactant network. The nanotubes coalesce, forming a three-way junction that propagates towards the state which has the shortest total tube length, i.e. the Fermat point. Adapted from Ref. 10.

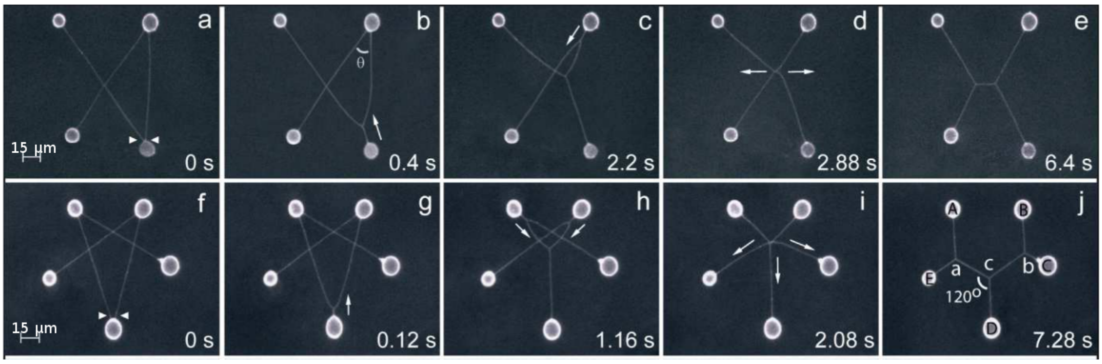

(b) Fluorescence microscopy images of the time evolution of a complex liposome network. In the final configuration the angles between the nanotubes at the Y-junctions are 120°. Adapted from Ref. 13.

Figure 2.4: Experimental observations of the time evolution of complex liposome network.

the position of the Y-junction where all the angles are exactly 120° is referred to as the Fermat point[a].

The formation of such Y-junctions and network structures has been thoroughly investigated in artificial networks,[10–13] an exemplary time evolution can be found in Figure 2.4. One can nicely observe the movement of the junctions towards the Fermat point described above. Interestingly, a similar observation has been made in dry foams in which the films between bubbles meet in triples, creating a junction which is usually called a plateau border. The angles between these films are always 120°.[14]

The formation of tubular structures and membrane networks can be induced by various different mechanisms, which can be classified into three different categories:[15] (i) formation by curvature-inducing proteins, (ii) formation by scaffolding and (iii) formation by force. These will be briefly summarized.

---

[a] The problem of finding the point in a triangle that minimizes the sum of the distances to the vertices was first addressed by the French mathematician Pierre de Fermat in the first half of the 17th century.[9]

(i): Curvature-inducing proteins have been widely observed in nature. This is shown in Fig. 2.3 using the example of caveolin, which anchors on the membrane surface acting effectively as a wedge, pushing the lipid headgroups apart and thus inducing spontaneous curvature.[6;16] Different mechanisms have been discussed, depending on the depth of protein insertion, which can induce either positive or negative curvature.[17;18] An important example for curvature-inducing proteins is reticulon which has been found to induce the tubular network structure in the endoplasmic reticulum.[19;20]

(ii): Another mechanism for tube formation is by scaffolding, in which proteins are polymerizing on the surface of the membrane, effectively forcing the membrane to adopt the shape of the proteins.[21;22] Interestingly, it is still controversial whether the polymerization actually leads to spontaneous curvature or whether spontaneous curvature also partly induces the polymerization, as has been observed in Ref. 22.

(iii): The most obvious way of creating tubular structure is by a force acting on a localized point on the membrane surface. This force can be induced by growing filaments which are connected to the membrane[23;24] or by molecular motors.[25–29] An important observation is that the pulling force induced by a single filament or motor has been shown not to be sufficient for tube formation,[25] thus requiring the formation of filament bundles[24] and a complex coordination of molecular motors.[26;27] The latter has been studied extensively in Refs. 27; 28 by direct comparison of *in vitro* experiments and stochastic simulations. It could be shown that at least $5 - 6$ motors, independently bound to different protofilaments, are necessary to achieve growth of membrane tubes.[27;28]

The function of tubular membrane networks is still under heavy debate and seems to strongly depend on the organelle. A recent review has intensively discussed potential physiological roles of the three-dimensional tubular network spanning the endoplasmatic reticulum,[8] including membrane trafficking, lipid metabolism and autophagy, i.e. the cleaning mechanism of the cell. The function of the tubular network in the Golgi apparatus appears to be the interconnection of different building blocks, which can also induce structural rearrangements during cell differentiation.[30] Membrane nanotubes have also been found to generally enhance intercellular transport.[31] In fact, the artificial formation of membrane networks could be an interesting way to improve intercellular communication and transport.[32]

The formation and stability of branched and tubular structures have also been studied via simulations and theory of coarse-grained models, as will be discussed in detail in Chapter 3 (simulations) and Chapter 5 (theory).

2.1.4 Stromules

A particular motivation for this work is the observation of tubular structures protruding from chloroplasts.[33–49] Chloroplasts are lens-shaped organelles with a length of $2-8\,\mu\mathrm{m}$, where photosynthesis takes place, another source of energy for the cell. These organelles are only present in plant cells. Interestingly, chloroplasts and other types of plastids can form very narrow and long protrusions, called stromules (stroma filled tubules). Some snapshots obtained from experiments can be found in Figure 2.5. Stromules are highly dynamic structures, which constantly form and retract, rapidly changing shape. They can reach lengths of up to $\sim 200\,\mu\mathrm{m}$ and have a diameter of $\sim 400-600\,\mathrm{nm}$.[40]

Stromules have actually been known for a relatively long time. The first observations were reported around the beginning of the 1900s.[50;51] However, stromules only became the focus of real interest and analysis around the beginning of the 21st century, where new imaging techniques allowed for better observations.[52] But even the past 20 years of detailed analysis could not answer some fundamental questions about stromules, namely why and under which conditions they form and what their function is. There are, of course, several hypotheses, e.g. the exchange of signals and metabolites[42;53] or the communication with the nucleus during environmental stress.[44;47–49] However, up to this point, no consistent theory has been proposed.

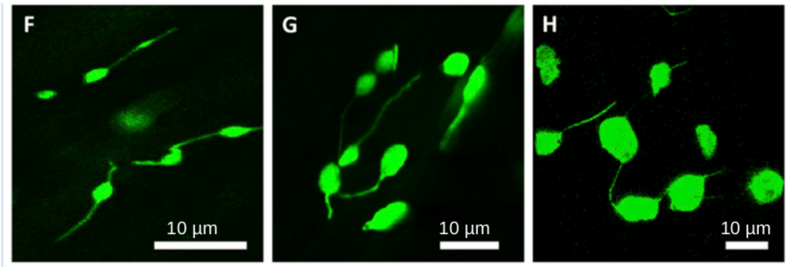

(a) Plastids (green blobs) and protruding stromules. Adapted from Ref. 42.

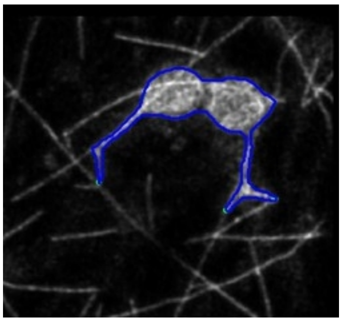

(b) Chloroplasts and branched stromules (blue contour) interacting with microtubules (white). Taken from Ref. 48.

Figure 2.5: Experimental observations of stromules.

3

Computer Simulations and Membrane Models

The era of computer simulations basically started, when the first computers were deployed in the 1940s. Early work by Nicholas Metropolis in 1953 laid the foundation for the Monte Carlo method,[54;55] a simulation technique based on stochastic sampling. A second method was developed around 1957 by Adler and Wainwright.[56;57] Their proposed molecular dynamics simulations are based on solving Newton's equations of motion to obtain the time evolution of a system. Both techniques are very commonly used today and applicable to all the different models that will be presented. They are both also used in this thesis.

Since the early pioneering work in the 1950s there has been a lot of development not just in simulation methods but also in computational power, making computer simulations a very powerful tool. Nowadays they play an essential role not just in physics but basically all fields of research. They have become an integral part of science, in addition to theory and experiments.

Modeling biological membranes is a very complex task. Processes take place on very different time and length scales and a typical membrane within a cell can contain hundreds of different types of lipids and is crowded with proteins. Whereas the lipid bilayer has a thickness of only $5 - 10\,\mathrm{nm}$, a typical cell organelle has a diameter of about $10\,\mu\mathrm{m}$. To solve such multiscale problems, different types of simulations and simulation models have been developed and specifically designed to analyze distinct processes on different scales.

These simulation models range from all-atom molecular dynamic simulations, where detailed molecular interactions are taken into account, via coarse-grained descriptions, to continuum models based on macroscopic phenomenological equations. The latter allow for the description of large membrane regions and shape changes, but in return lack the molecular detail. In the following an overview over the different simulation models is given and afterwards the two simulation techniques, i.e. Monte Carlo and molecular dynamics, are described.

The focus of this thesis lies on the description of entire cell organelles and their deformations, therefore a continuum model had to be employed. In this work a dynamically-triangulated surface model based on the Helfrich formalism is used. The model and the necessary mathematical background will be described in detail at the end of the chapter.

3.1 Simulation Models

The graph in Figure 3.1 shows the time and length scales covered by different simulation techniques. Quantum mechanical simulations and all-atom simulations, shown in the bottom left, cover only very short time and length scales, but are therefore very detailed. Continuum descriptions shown in the top right on the other hand allow to access large time and length scales, but in exchange lack molecular detail.

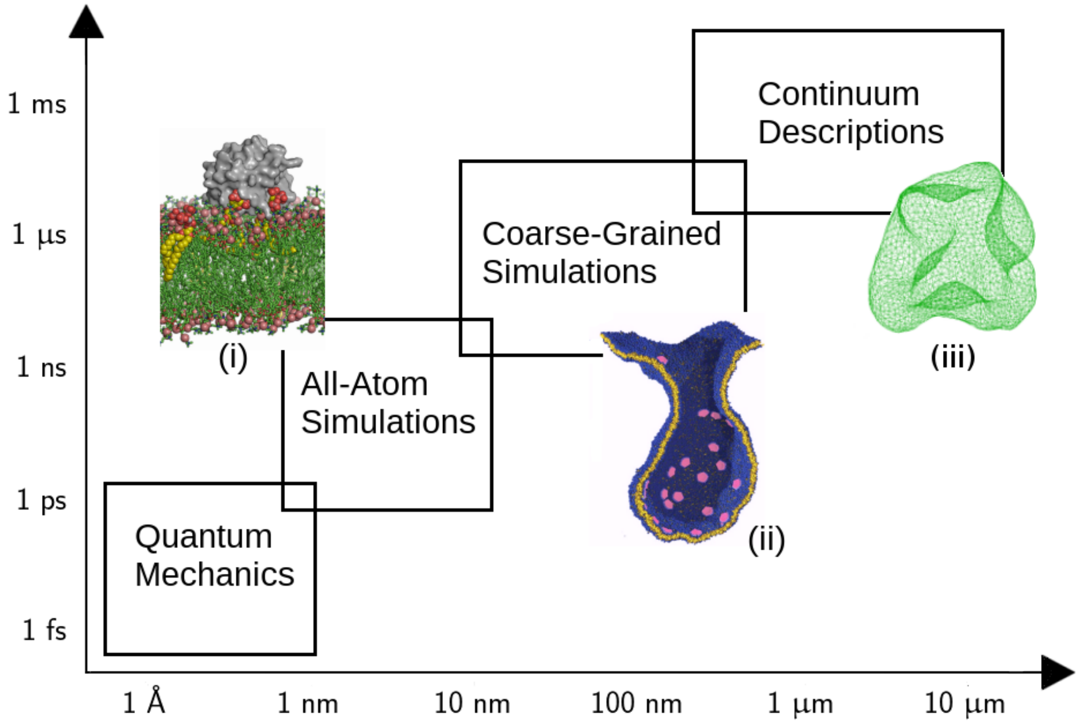

Figure 3.1: Overview of the different time and length scales accessible by different simulation techniques. Starting from quantum mechanical simulations in the bottom left at very short time and length scales all the way to continuum models in the top right.
(i) Protein-lipid interaction, taken from Ref. 58.
(ii) Budding induced by proteins, taken from Ref. 59.
(iii) Deformation of a vesicle, simulated using a dynamically-triangulated membrane model.

3.1.1 Ab Initio Simulations

Quantum mechanical or ab initio simulations allow to even take nuclei and their electronic structure into account. They are used for studying, e.g., chemical reactions, charge distribution and proton transfer,[60] but only on very short time and length scales. Their results, however, can give valuable input for higher-level simulations, i.e. to create atomistic and coarse-grained models of lipids and proteins.

3.1.2 All-Atom Models

All-atom simulations allow to take into account detailed interactions between atoms and molecules, i.e. each atom is modeled explicitly. These simulations are therefore very suited for studying fundamental membrane-related processes in great detail. Some examples are pore formation,[61–63] investigating the function of membrane proteins,[64;65] the interaction of proteins and lipids[58] or the dynamic organization or phase separation in multicomponent membranes.[66;67] Details can be found in recent reviews on modeling the effect of curvature remodeling proteins on vesicle deformation[68;69] (and references therein).

For these simulations usually atomistic force fields are used. These force fields are basically a set of many-body potentials that describe how atoms, bonds and molecules interact with each other. Force fields are typically parameterized using ab initio simulations or experimental data. A detailed overview of the most commonly used force fields can be found in Ref. 70.

The drawback of this detailed way of modeling, however, is that the time and length scales accessible are still rather limited. According to Ref. 1, state of the art atomistic simulations can reach times of $100 - 1000\,\mathrm{ns}$ and lengths of about $10 - 50\,\mathrm{nm}$. To go to larger scales, coarse-grained models have to be employed.

3.1.3 Coarse-Grained Models

In computer simulations coarse-graining refers to coarsening the level of representation. This means that instead of considering every atom individually, various atoms or molecules are combined into functional groups or interaction beads. This effectively reduces the number of particles in the system and it therefore speeds up the simulations.

There is a large variety of coarse-grained models, starting from models where 3-6 heavy atoms are grouped together (e.g. the MARTINI model[71;72]), all the way to representing one entire lipid or protein by only one single bead. The latter is also often referred to as super coarse-graining. Depending on the level of detail, these simulations can be up to three orders of magnitude faster than all-atom simulations, however, at the cost of loosing detailed information.

With these models a large variety of processes can be simulated. They are particularly suited for the investigation of large-scale (protein-induced) membrane remodeling processes, as e.g. the formation of membrane buds[59;73] or tubes.[74;75] One can also investigate membrane bilayer self-assembly,[76;77] raft formation in multicomponent membranes[78] and the phase behavior of lipid bilayers.[79;80]

3.1.4 Continuum Descriptions

To access even larger scales, especially for describing membrane shapes and topological changes, continuum descriptions are used. These models are based on describing the membrane as a smoothly curved mathematical surface. Information about the bilayer properties is only reflected in a few model parameters, such as the stiffness or bending rigidity, which means these model can only be applied when the molecular details are negligible.

To implement such a continuum description, there are two main approaches. One is using dynamically-triangulated surfaces, the other is a particle-based method. The model used in this thesis belongs to the first group and will be described in detail in Section 3.4. The necessary mathematical background for this model will be presented in Section 3.3.

In the particle-based models the surface is discretized by particles interacting via a set of potentials. These particles are, however, not interconnected by bonds. One unit segment or particle typically represents hundreds to thousands of lipids and/or proteins. These models are particularly useful for studying membrane self assembly[81–83] and deformations.[84–86] They have also been intensively used to study tubulation, for example by cooperatively growing filament bundles.[87]

3.1.5 Multiscale Models

Only very recently a new type of model has been proposed. By combining a continuum description with a finer atomistic or coarse-grained model it has been attempted to bridge the large gaps in the length and time scales of biological processes.[88–91]

One very promising approach has been proposed in Ref. 92. The authors access the different levels of resolution through a multi-scale scheme, combining a dynamically-triangulated membrane model with a coarse-grained model. The dynamically-triangulated membrane model allows to analyze large-scale conformational changes,

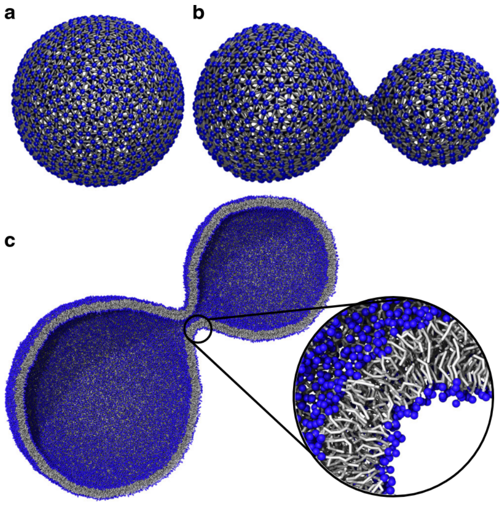

Figure 3.2: Exemplary simulation using a multiscale scheme. a) Original configuration of the vesicle. b) The vesicle is equilibrated using a dynamically-triangulated surface simulation. c) A backmapping scheme allows to add information about lipids using the MARTINI force field.[71;72] The system can now be simulated and checked for stability. Taken from Ref. 92.

while the local properties can be explored at coarse-grained resolution. The authors were for example able to simulate an entire mitochondrial structure, albeit so far only for a very short time, with different lipid compositions in the inner and outer membrane or the formation of a membrane bud as illustrated in Figure 3.2.

3.2 Simulation Techniques

3.2.1 Monte Carlo Simulations

In Monte Carlo (MC) simulations the desired quantities are approximated by repeated random sampling of a finite configuration space. The most straightforward sampling technique is direct sampling, in which a random point in the configuration space is chosen every move, allowing to calculate an ensemble average. Such a sampling can for example be applied to evaluate multi-dimensional integrals.

The problem when using direct sampling to calculate (canonical) phase space averages in computer models is that basically all configurations will have zero probability and therefore not contribute significantly to the phase space average. In these cases an importance sampling scheme is usually applied. In this technique, one starts with a certain initial configuration and can then create new configurations by small changes of the previous configuration. These changes are accepted according to the law of detailed balance. This ensures both consistency of the algorithm and efficiency of sampling. One very commonly used method is the Metropolis method.

The **Metropolis algorithm** works as follows:

```
1. calculate the energy of the system $E_{\text{old}}$
2. select one particle (or something equivalent) of the system at random
3. randomly displace this particle and calculate the new energy of the system $E_{\text{new}}$
4. if $E_{\text{new}} < E_{\text{old}}$:
        accept the displacement (move)
   else:
        accept it with the probability $P = \exp(-(E_{\text{new}} - E_{\text{old}})/\beta)$
5. return to step 1
```

This algorithm allows to efficiently switch between different states π_n of the system and clearly fulfills detailed balance, i.e., $P(\pi_n \to \pi_{n+1})/P(\pi_{n+1} \to \pi_n) = \rho(\pi_{n+1})/\rho(\pi_n)$, with the canonical probability density $\rho(\pi_n) = e^{-\beta H(\pi_n)}$. The canonical ensemble average of an observable A at temperature T (with inverse temperature $\beta = 1/(k_{\text{B}}T)$), can then be computed as $\langle A \rangle = \sum_n A(\pi_n)$, see for example Chapter 3 in Ref. 93.

This method can be applied to any kind of 'move', including simple translations of individual particles, but also more complicated structural rearrangements of polymers, making MC a very efficient sampling tool. It is, however, important to note that the time evolution of the system does not correspond to the real time evolution as defined by the Liouville operator.

3.2.2 Molecular Dynamics Simulations

To obtain the time evolution of a system, molecular dynamics (MD) simulations can be employed. In MD simulations, Newton's equations of motion

$$\vec{F}_i(t) = m_i \ddot{\vec{r}}_i(t) \qquad \text{with} \qquad \vec{F}_i(t) = -\vec{\nabla} U(\{\vec{r}_j\}, t) \tag{3.1}$$

are solved numerically. Here $\vec{r}_i$ denotes the position of particle i and m_i its mass. $\vec{F}_i$ is the force acting on this particle, which is determined by the potential U, and t is the time. The potential U describes the interactions between the particles in the system and depends on the underlying microscopic or coarse-grained model. The system corresponds to a microcanonical ensemble.

The quality of the simulations evidently depends on how accurately and efficiently Newton's equations of motion can be integrated. Over the years various integration schemes have been developed. A very popular and efficient one is the Velocity

Verlet algorithm,[94] which is based on the Verlet algorithm proposed by Verlet in 1967[95] and was then further extended:

$$\vec{r}_i(t+\Delta t) = \vec{r}_i(t) + \vec{v}_i(t)\Delta t + \frac{\vec{F}_i(t)}{2m_i}\Delta t^2 \tag{3.2}$$

$$\vec{v}_i(t+\Delta t) = \vec{v}_i(t) + \frac{\vec{F}_i(t) + \vec{F}_i(t+\Delta t)}{2m_i}\Delta t \tag{3.3}$$

where $\vec{v}_i$ is the velocity of particle i. This algorithm is symplectic, meaning that it describes a canonical transformation and conserves the phase space volume. This property is very important, in particular with respect to energy conservation.

In coarse-grained simulations, the simulation model does often not explicitly include the solvent, in which the particle, molecule or protein of interest is suspended. Instead, the solvent is included implicitly by extending the equations of motion and considering a Langevin equation:[96]

$$m_i\ddot{\vec{r}}_i(t) = -\vec{\nabla}U(\{\vec{r}_j\},t) - \lambda\vec{v}_i(t) + F^{\mathrm{R}}(t) \tag{3.4}$$

In this equation λ is the damping coefficient. The damping term, $-\lambda\vec{v}_i(t)$, mimics the systematic, dissipative interactions with the solvent particles, while the stochastic noise term, $F^{\mathrm{R}}(t)$, corresponds to thermal fluctuations, i.e. the random collisions of solvent particles with the suspended molecule.

The stochastic forces and dissipative interactions are connected by the fluctuation-dissipation relation, $\langle F^{\mathrm{R}}(t)F^{\mathrm{R}}(0)\rangle = 2\lambda k_{\mathrm{B}}T\delta(t)$, which allows us to control the temperature of the system. The configurations in the simulations are now sampled from a canonical phase space density. The noise is random and uncorrelated and usually drawn from a Gaussian probability distribution with zero mean, obeying $\langle F^{\mathrm{R}}(t)\rangle = 0$.

The description above is just a brief overview of the simulation techniques used in this work. Both MC and MD simulations can be used in a much wider context and have many more features and functions. A more detailed description of these two methods and computer simulations in general can be found in standard textbooks, for example Refs. 93; 97.

3.3 Continuum Model of Biological Membranes: Helfrich Hamiltonian

When looking at membranes on large scales, they can be described in a simplified way as two-dimensional surfaces embedded in three-dimensional space. This simplification is justified if it is not necessary to consider all the molecular details, i.e. the exact lipid and protein composition, and if the thickness of the bilayer is small compared to the overall size of the system. The typical size of an organelle or vesicle is three to four orders of magnitude larger than the thickness of the bilayer, therefore this is a valid approximation in our case.

For analyzing these two-dimensional surfaces, methods from differential geometry can be employed. This was first accomplished by Canham,[98] Helfrich[99] and Evans[100] in the early 1970s. They were able to derive a continuum-mechanical description to describe membrane surfaces on large scales. This theory is nowadays most commonly referred to as Helfrich theory, and it will be explained in detail in the following.

To determine the energy of the membrane, two main contributions are considered. The first contribution relates to stretching or compressing the membrane. The second term refers to the energy associated with bending the membrane. The energy can therefore be expressed by the following equation, commonly referred to as Helfrich Hamiltonian H:

$$H = H_{\text{stretch}} + H_{\text{bend}} \tag{3.5}$$

The stretching term H_{stretch} describes changes in the area of the membrane due to stretching and compression. It is given by:

$$H_{\text{stretch}} = \sigma_{\text{S}} \int \mathrm{d}A \tag{3.6}$$

with the surface tension σ_{S} and the integral over the area of the membrane A. The contribution of the first term, H_{stretch}, is assumed to be negligible in our simulations, because we include an additional constraint on the total surface area, c.f. Equation 3.12, thus this term gives a constant contribution and is omitted in this work.

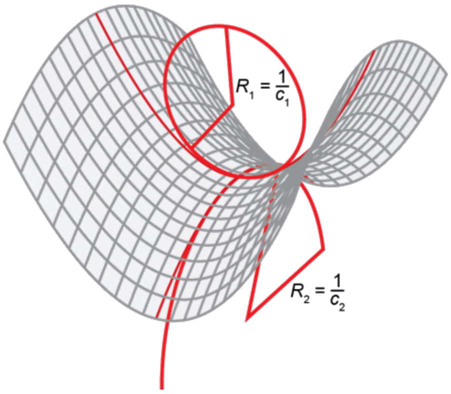

Figure 3.3: Illustration of the two principal curvatures c_1 and c_2 at a certain point on the membrane. The principal curvatures are the inverse of the curvature radii R_1 and R_2. Taken from Ref. 101.

The second term[a] describes how the membrane is affected by bending deformations:

$$H_{\text{bend}} = \frac{\kappa}{2} \int \mathrm{d}A(K - K_0)^2 + \bar{\kappa} \int \mathrm{d}AK_{\text{G}} \tag{3.7}$$

where κ and $\bar{\kappa}$ are material constants called curvature moduli. K is the total, K_0 the spontaneous and K_{G} the Gaussian curvature.

The total curvature is given by the sum over the two principal curvatures c_1 and c_2, $K = (c_1 + c_2)$, and the Gaussian curvature is given by $K_{\text{G}} = c_1 c_2$.[b] The spontaneous curvature K_0 is a material property that describes any curvature the membrane might have due to a lipid asymmetry in the bilayer or the shape of the lipids. For symmetric bilayers this factor is usually zero and would refer to a flat surface.

The two principal curvatures c_1 and c_2 can be described as the inverse of the curvature radii R_1 and R_2, which indicate how strongly the membrane is curved at a given point, as illustrated in Figure 3.3. The mathematical background and the derivation of these equations is given in Appendix B.1.

A description based on the Helfrich Hamiltonian given by Equations 3.5 - 3.7 is still relatively complex, but for closed vesicles and when investigating large scales, some further simplifications can be made. Throughout this work we will assume that K_0 is negligible, i.e. that there are no bilayer asymmetries. However, we will later reinstate a similar term, to investigate the effects of such bilayer asymmetries or curvature-inducing proteins on the stability of the system (see Section 7.4.4).

The second simplification concerns the Gaussian curvature K_{G}. According to the Gauss-Bonnet theorem,[102] integrating this term over a closed surface gives a constant contribution. Since throughout this work closed vesicles will be analyzed, this theorem can indeed be applied and this term can therefore be neglected.

Hence, the equation for the bending energy can be simplified and is given by:

$$H_{\text{bend}} = \frac{\kappa}{2} \int \mathrm{d}AK^2 \tag{3.8}$$

In general, this equation can not be solved analytically. One therefore requires a discretized version and has to rely on numerical solvers. The discretization employed in this work, a dynamically-triangulated membrane model, is described in the subsequent section.

---

[a] In the literature different representations of this equation exist. They mostly vary by a (historical) factor of two and can all be transformed into each other. Throughout this work, this definition will be used.

[b] We use the convention that c_1 and c_2 are both positive for a sphere.

3.3.1 Further Extensions

There are some further extensions that have been made to the 'classical' Helfrich Hamiltonian described above over the past decades. For most of this work the simple model given by Equation 3.8 is used. In the following one potential extension will be briefly introduced.

The term given by Equation 3.8 is usually referred to as the simple model. When including the spontaneous curvature K_0, as in Equation 3.7, this is referred to as the spontaneous curvature (SC) model. It is also possible to account for an area density difference in the two layers of the lipid bilayer, by setting a constraint on the area difference ΔA between the two monolayers forming a bilayer.

There are two techniques to include this area difference into computer simulations. In the bilayer couple (BC) model this value is set to the targeted area difference ΔA_0,[100;103;104] whereas in the area-difference elasticity (ADE) model[105–108] deviations from the targeted area difference are penalized by a nonlocal bending energy which is proportional to $E_{\text{bend}}^{\text{n.l.}} \sim (\Delta A - \Delta A_0)^2$. In the last part of this thesis we will employ the ADE model to stabilize tubular and branched structures.

3.4 Triangulated Membrane Model

For the simulations performed in this work, a dynamically-triangulated surface model was used. Similar to the particle-based models the membrane is described as a smoothly curved mathematical surface. The discretization is, however, slightly different. The surface is represented by vertices that are connected by bonds or tethers to form a triangular network structure. Again, one unit segment represents hundreds to thousands of lipids and proteins and the bilayer properties are reflected by the values of the model parameters. The model used is based on early work presented in Refs. 109–111. A good comparison between different ways of implementing the model can be found in Ref. 112.

A big advantage of this method of discretization is that the area and the volume of the system, e.g. a closed vesicle, can be easily controlled and fixed. Triangulated surface models allow to investigate a variety of problems, such as shape changes,[113–115] shape changes by adsorption of particles,[116–119] multicomponent membranes[120] and even vesicles in flow fields.[121] A few examples are shown in Figure 3.4.

In the following, the potentials, parameters and techniques used for the simulations will be listed.

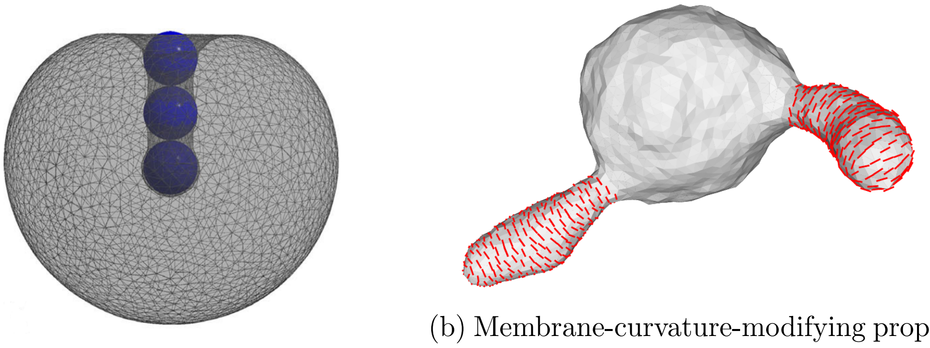

(a) Particles (blue) are wrapped by a membrane tube invagination that points into the vesicle. Taken from Ref. 116.

(b) Membrane-curvature-modifying properties are modeled by an in-plane nematic field (red). These nematogens aggregate and cause conformational changes. Taken from Ref. 115.

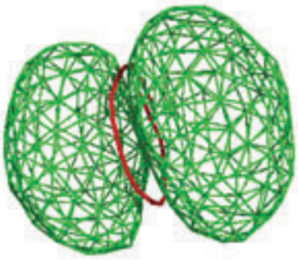

(c) Polymers (red) adsorbed on the membrane cause conformational changes. Taken from Ref. 117.

Figure 3.4: Some examples for the application of the dynamically-triangulated membrane model.

3.4.1 Model Parameters

The original code used in this work was written by Prof. H. Noguchi from the University of Tokyo[c], who courteously provided the source code of his program. It was then further adapted to target our specific problems. The model is described in detail in Ref. 122 and in the following the most important aspects will be highlighted.

The surface representing the membrane is discretized by N vertices which are connected by bonds or tethers to form a triangular network structure. This is shown in Figure 3.5 for a simple spherical vesicle. These vertices have an excluded volume and mass. In the simulations $N = 2562$ vertices were used, which results in $N_{\text{bond}} = 7680$ bonds and $N_{\text{t}} = 5120$ triangles. The latter can be calculated using Euler's formula[d]. If not otherwise specified the numbers above were used. For

---

[c] Institute for Solid State Physics, University of Tokyo, Chiba 277-8581, Japan

[d] L. Euler (1707-1783) is known to be the first to have discovered the relation between vertices V, edges E and faces F of a convex polyhedron, where $V - E + F = 2$.[123]

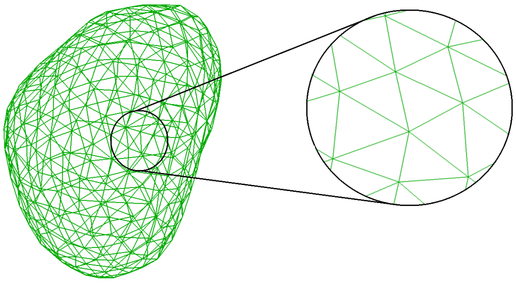

Figure 3.5: Triangulated network structure. The surface is discretized by a triangular mesh.

validation some simulations were performed with a larger number $N = 10242$ of vertices, which results in $N_{\mathrm{bond}} = 30720$ bonds and $N_{\mathrm{t}} = 20480$ triangles.

Curvature

The shape of the vesicle is mostly controlled by the curvature energy, which was described in the previous section and is given by Equation 3.8. This equation is now discretized as follows:[122;124;125]

$$U_{\mathrm{cv}} = \frac{\kappa}{2} \sum_i \frac{1}{\sigma_i} \left(\sum_{j(i)} \frac{\sigma_{i,j} \vec{r}_{i,j}}{r_{i,j}} \right)^2 \tag{3.9}$$

The value for the bending rigidity for lipid membranes is typically $\kappa = 20\, k_{\mathrm{B}}T$,[126] where $k_{\mathrm{B}}T$ is the thermal energy. The first sum goes over all vertices i and the second sum goes over all neighbors of the vertex i, $j(i)$, that are connected by bonds. The vector between vertices i and j is denoted by $\vec{r}_{i,j} = \vec{r}_i - \vec{r}_j$ and $r_{i,j} = \|\vec{r}_{i,j}\|$. $\sigma_{i,j}$ is the length of the bond in the dual lattice, which is given by $\sigma_{i,j} = r_{i,j}[\cot(\theta_1) + \cot(\theta_2)]/2$, where θ_1 and θ_2 are the angles opposite to the bond connecting i and j in the two triangles sharing this bond. The parameters are illustrated in Figure 3.6. The area of the dual cell of vertex i is given by $\sigma_i = 0.25 \sum_{j(i)} \sigma_{i,j} r_{i,j}$.

Bond and Repulsive Interactions

In order to perform molecular dynamics simulations a Stillinger-Weber potential[127] is used to describe bond and excluded-volume interactions between vertices. All vertices connected by tethers interact via the following attractive bond potential:

$$U_{\mathrm{bond}}(r_{i,j}) = b \begin{cases} \dfrac{a \exp[a/(l_{\mathrm{c0}} - r_{i,j})]}{l_{\max} - r_{i,j}} & (r_{i,j} > l_{\mathrm{c0}}) \\ 0 & (r_{i,j} \le l_{\mathrm{c0}}) \end{cases} \tag{3.10}$$

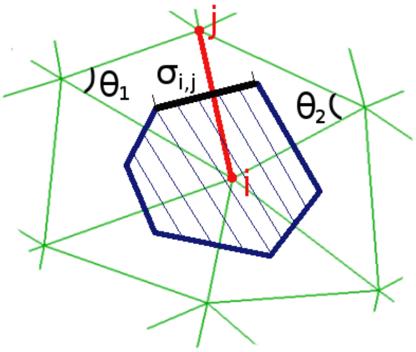

Figure 3.6: Illustration of the parameters needed for the calculation of the discretized curvature energy. In green the triangulated mesh is shown and in blue the dual lattice.

and at short distances all particles interact via a repulsive excluded volume potential:

$$U_{\mathrm{rep}}(r_{i,j}) = b \begin{cases} \dfrac{a \exp[a/(r_{i,j} - l_{\mathrm{c1}})]}{r_{i,j} - l_{\min}} & (r_{i,j} < l_{\mathrm{c1}}) \\ 0 & (r_{i,j} \geq l_{\mathrm{c1}}) \end{cases} \tag{3.11}$$

The numerical values for the parameters of the potentials are listed in Table 3.1, where the parameter a refers to the bond length and the parameter b is a constant energy prefactor. This bond length is set to one in all simulations. This is common practice and can be done because the system is scale invariant.

Parameter	Value	Description
$l_{\max}$	$1.33a$	maximum bond length
$l_{\min}$	$0.67a$	minimum distance between two vertices
l_{c0}	$1.15a$	cutoff length for U_{bond}
l_{c1}	$0.85a$	cutoff length for U_{rep}

Table 3.1: Parameters used for the bond and repulsive interactions.

Area and Volume Control

To keep the area A and volume V of the vesicle constant, constraint potentials are added:

$$U_{\mathrm{S}} = \frac{1}{2} k_{\mathrm{S}} (A - A_0)^2 \tag{3.12}$$

$$U_{\mathrm{V}} = \frac{1}{2} k_{\mathrm{V}} (V - V_0)^2 \tag{3.13}$$

Here k_{S} and k_{V} determine the strength of these constraints. A_0 and V_0 give the desired area and volume of the system.

Overall Potential

Finally, the overall potential used in the simulations is a combination of all the potentials described above:

$$U_{\mathrm{tot}} = U_{\mathrm{cv}} + U_{\mathrm{bond}} + U_{\mathrm{rep}} + U_{\mathrm{S}} + U_{\mathrm{V}} \tag{3.14}$$

The total Hamiltonian of the system is therefore:

$$H_0 = \sum_{i=1}^{N} \frac{\vec{p}_i^{\,2}}{2m} + U_{\mathrm{tot}} \tag{3.15}$$

where $\vec{p}_i$ are the momenta of the vertices and m their masses.

Application of an External Force

In the simulations an external force $\vec{F}_{\mathrm{ext}}$ on individual vertices will often be applied. This corresponds to a change of the Hamiltonian H_0 to:

$$H = H_0 - \sum_{j \in N_{\mathrm{f}}} \vec{F}_{\mathrm{ext},j} \vec{r}_j \tag{3.16}$$

where N_{f} is the set of vertices to which the external force $\vec{F}_{\mathrm{ext},j}$ is applied and $\vec{r}_j$ are the positions of these vertices.

3.4.2 Implementation

The simulation is a combination of molecular dynamics (MD) and Monte Carlo (MC) simulations. The vertices are moved using MD, while bond flipping, which models the fluidity of the membrane, is carried out using MC.

Vertex Dynamics

For integrating Newton's equations of motion the Velocity Verlet[94] formulation of the BBK integrator[128] is used. This corresponds to the discretization of the Langevin equation 3.4. Therefore, in addition to the force determined by the potentials, a random noise term and a systematic friction term are introduced. The new positions and velocities of the vertices are given by:

$$\vec{v}(t + \frac{\Delta t}{2}) = \frac{1 - \lambda \frac{\Delta t}{2m}}{1 + \lambda \frac{\Delta t}{2m}} \vec{v}(t - \frac{\Delta t}{2}) + \frac{\frac{\Delta t}{m}}{1 + \lambda \frac{\Delta t}{2}} [\vec{F}(t) + \vec{F}^{\mathrm{R}}(t)] \tag{3.17}$$

$$\vec{r}(t + \Delta t) = \vec{r}(t) + \vec{v}(t + \frac{\Delta t}{2}) \Delta t \tag{3.18}$$

The integration timestep is Δt, $\vec{F}$ the force determined by the potentials and $\vec{F}^{\mathrm{R}}$ the force due to random noise. λ is the friction coefficient and m the mass of the vertex.

The forces acting on the vertices can be determined by calculating the derivatives of the potentials with respect to the vertex positions $\{\vec{r}_i\}$. The forces due to the bond and repulsive potentials can be calculated in a relatively straightforward manner, because they directly and only depend on the distances between two vertices.

Calculating the force caused by the area, volume and curvature potentials is slightly different, because the potentials depend on overall properties of the system, namely the total area and volume. For the area contribution, the force acting on particle i is given by:

$$\vec{F}_{\mathrm{S},i} = -\frac{\mathrm{d}U_{\mathrm{S}}}{\mathrm{d}\vec{r}_i} = -\frac{\mathrm{d}U_{\mathrm{S}}}{\mathrm{d}A}\frac{\mathrm{d}A}{\mathrm{d}\vec{r}_i} \tag{3.19}$$

The first term can be easily calculated:

$$-\frac{\mathrm{d}U_{\mathrm{S}}}{\mathrm{d}A} = -k_{\mathrm{S}}(A - A_0) \tag{3.20}$$

The second term, $\frac{\mathrm{d}A}{\mathrm{d}\vec{r}_i}$, can now be calculated via geometrical relations. The total area is the sum over the area of each vertex A_i, which is given by the weighted sum over the area of all neighboring triangles A_α:

$$A = \sum_{i=1}^{N} A_i \qquad \text{with} \qquad A_i = \frac{1}{3} \sum_{\alpha \in \text{neigh. triangles}} A_\alpha . \tag{3.21}$$

Here and in the following quantities with greek indices denote triangles and roman indices denote vertices. A similar calculation can be performed for the volume contribution and the curvature potential.

The volume V enclosed by the membrane is calculated as:[113]

$$V = \sum_{\alpha=1}^{N_{\mathrm{t}}} V_\alpha \qquad \text{with signed subvolumes} \qquad V_\alpha = \frac{1}{3}(\hat{n}_\alpha \cdot \vec{R}_\alpha) A_\alpha \tag{3.22}$$

where $\hat{n}_\alpha$ is the unit normal vector of triangle α pointing outwards and $\vec{R}_\alpha$ is the position vector of one of the vertices of the triangle relative to an a reference point. This reference point can, in fact, be chosen arbitrarily and can even lie outside of the structure, because any additional contribution from outside the vesicle, will eventually be subtracted by another subvolume V_α. This, however, only works if the normal vectors are all pointing outside of the vesicle, i.e. one needs to know, where the inside and outside of the vesicle are.

In the very last part of this thesis, we will also consider a renormalized area difference[e] Δa, which is defined as:

$$\Delta a = \frac{1}{4\sqrt{\pi A_0}} \int \mathrm{d}AK = \frac{1}{4\sqrt{\pi A_0}} \sum_{i=1}^{N} |\vec{H}_i| \frac{\vec{H}_i \cdot \hat{n}_i}{|\vec{H}_i \cdot \hat{n}_i|} \tag{3.23}$$

where $\vec{H}_i$ is the oriented curvature contribution of vertex i,

$$\vec{H}_i = \sum_{j(i)} \frac{\sigma_{i,j}\vec{r}_{i,j}}{r_{i,j}}. \tag{3.24}$$

Here, the term $\vec{H}_i \cdot \hat{n}_i / |\vec{H}_i \cdot \hat{n}_i|$ gives the orientation of the curvature, i.e. if it is convex (+1) or concave (-1) using the surface normal vector $\hat{n}_i$, as the average orientation of the neighboring triangles. The normalization is chosen such that a sphere has an area difference of $\Delta a = 1$. The force is given by the respective derivative.

Bond Flips

Biological membranes behave as two-dimensional fluids, as described in Section 2.1.2. This means that lipids can freely stream within their bilayer and hence the membrane behaves as a two-dimensional fluid. To model this fluidity, bond flips are introduced. This means that a bond can be flipped between the two possible diagonals of two adjacent triangles, as illustrated in Figure 3.7. These moves are accepted or rejected using the Metropolis Monte Carlo method, described in Section 3.2.1.

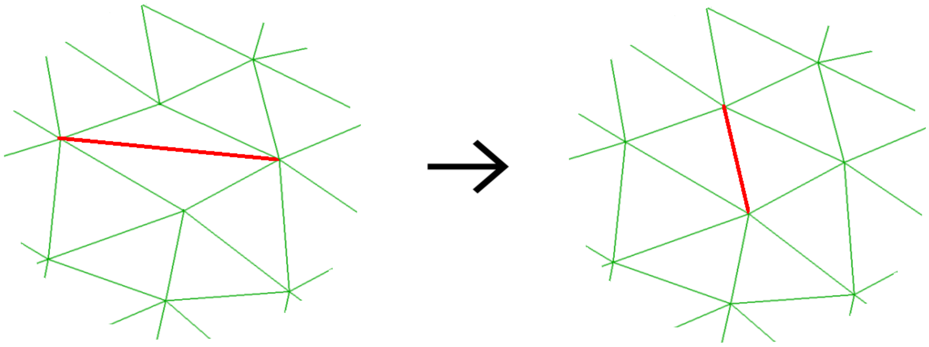

Figure 3.7: Illustration of a bond flip. The red bond was flipped using the Metropolis Monte Carlos method.

---

[e] The area difference ΔA is usually given by $\Delta A = 2h \int \mathrm{d}AK$, where h is the thickness of the membrane.[112] However, different conventions exist,[100;103–108;112;113] which makes it more convenient to use the renormalized area difference Δa that is one for a sphere.

Every 20 MD steps bond flips are carried out. For this, N_{bond} edges are randomly chosen and attempted to be flipped. For each chosen bond, the energy difference between the configurations is calculated and the flip is then accepted with a certain probability according to the Metropolis Method.

3.4.3 Units and Parameters

The units in the simulations are given by $\sigma = a$ (unit of length), $\epsilon = \frac{\kappa}{20}$ (unit of energy) and $\tau = \sigma\sqrt{m\epsilon^{-1}}$ (unit of time). In the simulations all units were set to one. All quantities reported in the following will be given in terms of these units, except when it is explicitly stated otherwise. In most simulations the remaining parameters are set to $b = 80$, $\lambda = 1$, $k_{\mathrm{S}} = 2$, $k_{\mathrm{V}} = 1$, $\Delta t = 10^{-4}$ and $k_{\mathrm{B}}T = 1$. Some simulations were performed at a lower temperature, to reduce thermal fluctuations, as will be discussed in the respective sections.

4

Computer Simulations of Vesicles: Tube Formation

To investigate tubular structures, it was first analyzed how the shape of a closed vesicle is affected by an external pulling force. For large enough forces the formation of tubes could be observed and a new final stable configuration, a vesicle with one or two tubes, was reached. This shape evolution was analyzed with particular emphasis on the equilibrium tube length and radius. The latter can also be derived from theory and our simulation results are in good agreement with the theoretical predictions.

After a brief introduction to our method, the different shapes obtained will be illustrated. It will then be analyzed how the length and radius of the tubes evolve over time and depend on the strength of the external force. Finally, our results obtained from simulations will be compared to theoretical predictions.

4.1 Methodology

A relevant quantity that characterizes our system is the reduced volume ν of the vesicle. The reduced volume is a dimensionless quantity, which gives the ratio between the volume V and area A of a closed structure:

$$\nu = \frac{3V}{4\pi R_{\mathrm{s}}^3} = \frac{6\sqrt{\pi}V}{A^{3/2}} \tag{4.1}$$

The reduced volume is normalized in such a way that $\nu = 1$ for a perfect sphere. The radius R_{s} is the radius of a sphere with given surface area $A = 4\pi R_{\mathrm{s}}^2$.

The starting configuration for all simulations was a stable closed vesicle. This configuration was obtained by simulating the vesicle without any external forces. Since the reduced volume ν of tubular geometries varies from that of a sphere ($\nu = 1$), all simulations were carried out for three different reduced volumes, namely $\nu = 0.6$, 0.7 and 0.8.

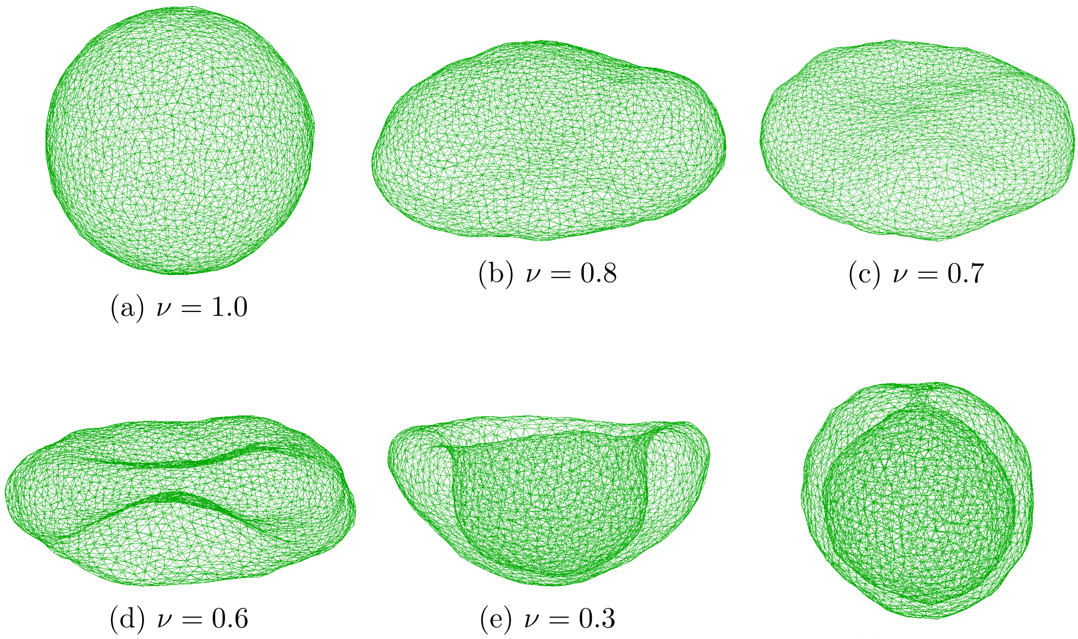

(a) $\nu = 1.0$

(b) $\nu = 0.8$

(c) $\nu = 0.7$

(d) $\nu = 0.6$

(e) $\nu = 0.3$

(f) $\nu = 0.2$

Figure 4.1: Shapes of the vesicle for different reduced volumes ν. This Figure and all following visualizations of membranes were created using ParaView.[129]

4.2 Equilibration without External Forces

Even without applying an external force, a vesicle can be deformed by varying its area to volume ratio ν, as shown in Refs. 113; 130. Varying the area to volume ratio can also be easily achieved in our simulations. Vesicles with different reduced volumes were simulated and their shapes analyzed. Some snapshots can be found in Figure 4.1. These shapes nicely match those reported in the literature, both theoretical and experimental.

For a reduced volume of $\nu = 1.0$, a perfect sphere is obtained. By reducing ν, the sphere starts to deform. For $\nu = 0.8$ and $\nu = 0.7$, a slightly elongated, prolate shape is observed. Decreasing the reduced volume to $\nu = 0.6$ leads to the formation of an oblate shape, the typical shape of a red blood cell. By decreasing the reduced volume even further, to $\nu = 0.3$ and $\nu = 0.2$, a stromatocyte forms, which is basically a smaller sphere within a bigger outer sphere with a (small) connective neck.

All simulations were carried out at a finite temperature T. This causes small thermal fluctuations of the surface, which can be seen when taking a closer look at the configurations in Figure 4.1. By decreasing the temperature, these fluctuations would vanish and the shapes would be perfectly smooth. The focus of this thesis, however, is the modeling of real biological systems. Simulations were therefore (mostly) carried out at a finite temperature.

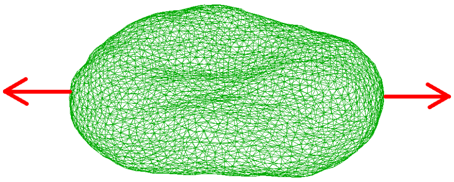

Figure 4.2: Snapshot of a vesicle; the external forces were applied in opposing directions, as illustrated by the two red arrows.

4.3 Shape Evolution due to External Forces

It was then investigated how the shape of a vesicle changes, when applying a constant external force $\vec{F}_{\text{ext}}$, with $F_{\text{ext}} = |\vec{F}_{\text{ext}}|$. The formation of one or two tubes was investigated. In the case of one tube an arbitrary point was chosen to which an external force was applied. In the other case the two points furthest apart[a] were chosen and opposing forces applied, as illustrated in Figure 4.2. Either a constant force or a stepwise increasing force was used, depending on the properties that were investigated.

Applying an external force on the membrane clearly changes its stable configuration. An exemplary time evolution of the shape can be found in Figure 4.3. In this case a constant force was applied on opposing poles. If the force is strong enough the vesicle first starts to elongate and forms a 'lemon' shape (see Figure 4.3b). When simulating longer, the formation of tubes can be observed, which lengthen over time (see Figure 4.3c). The resulting stable configuration is a sphere with two tubes (see Figure 4.3d). The final state and length of the tubes depends on the external force. This dependence will be investigated in detail in the subsequent sections.

Snapshots of the final stable configurations for different forces and different reduced volumes can be found in Figures 4.4 and 4.5. In Figure 4.4 only one external force was applied, whereas in Figure 4.5 two forces in opposing directions were applied. A complete catalog of the shapes for all forces and reduced volumes can be found in Appendix A.1.

Various shapes formed for the different external forces and reduced volumes. The onset of the tube formation starts at $F_{\text{ext}} \approx 40 - 50$. As one would intuitively expect, the tube length increases for higher forces. In addition one also obtains longer tubes for smaller reduced volumes. It is also interesting to see that, even when applying two opposing forces, only one tube forms in the lower force regime, see Figures 4.5d-4.5f. Only when going to higher forces a vesicle with two tubes is obtained.

---

[a] It should be noted that it is not relevant which points are initially chosen. Due to the fluidity of the membrane the first thing that would happen to two arbitrarily chosen vertices is that they would move as far apart as possible, without deforming the membrane. To speed up the process, the two points furthest apart were therefore directly picked and the simulations started from there.

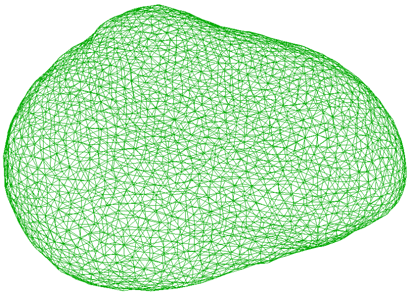

(a) starting configuration

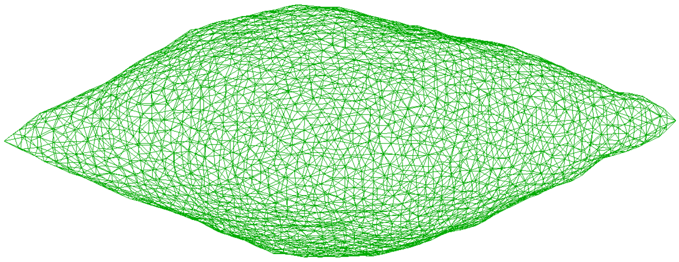

(b) 'lemon' shape

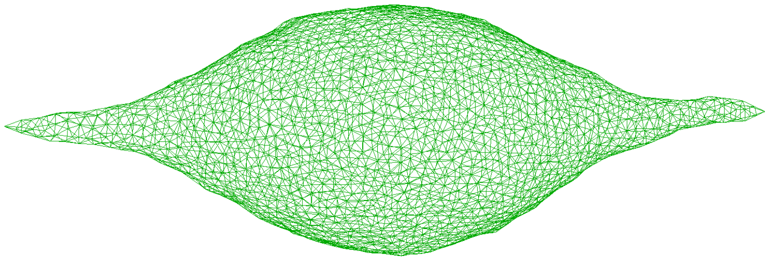

(c) tube formation

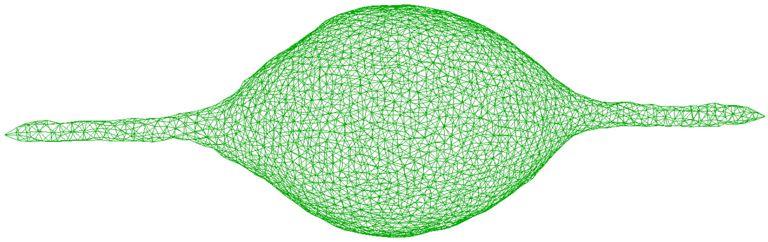

(d) final stable configuration - sphere with two tubes

Figure 4.3: Snapshots of the time evolution of a vesicle with applied external forces. The new stable configuration consists of a sphere with two tubes and is reached via a lemon shaped state ($\nu = 0.8;\ F_{\text{ext}} = 120$).

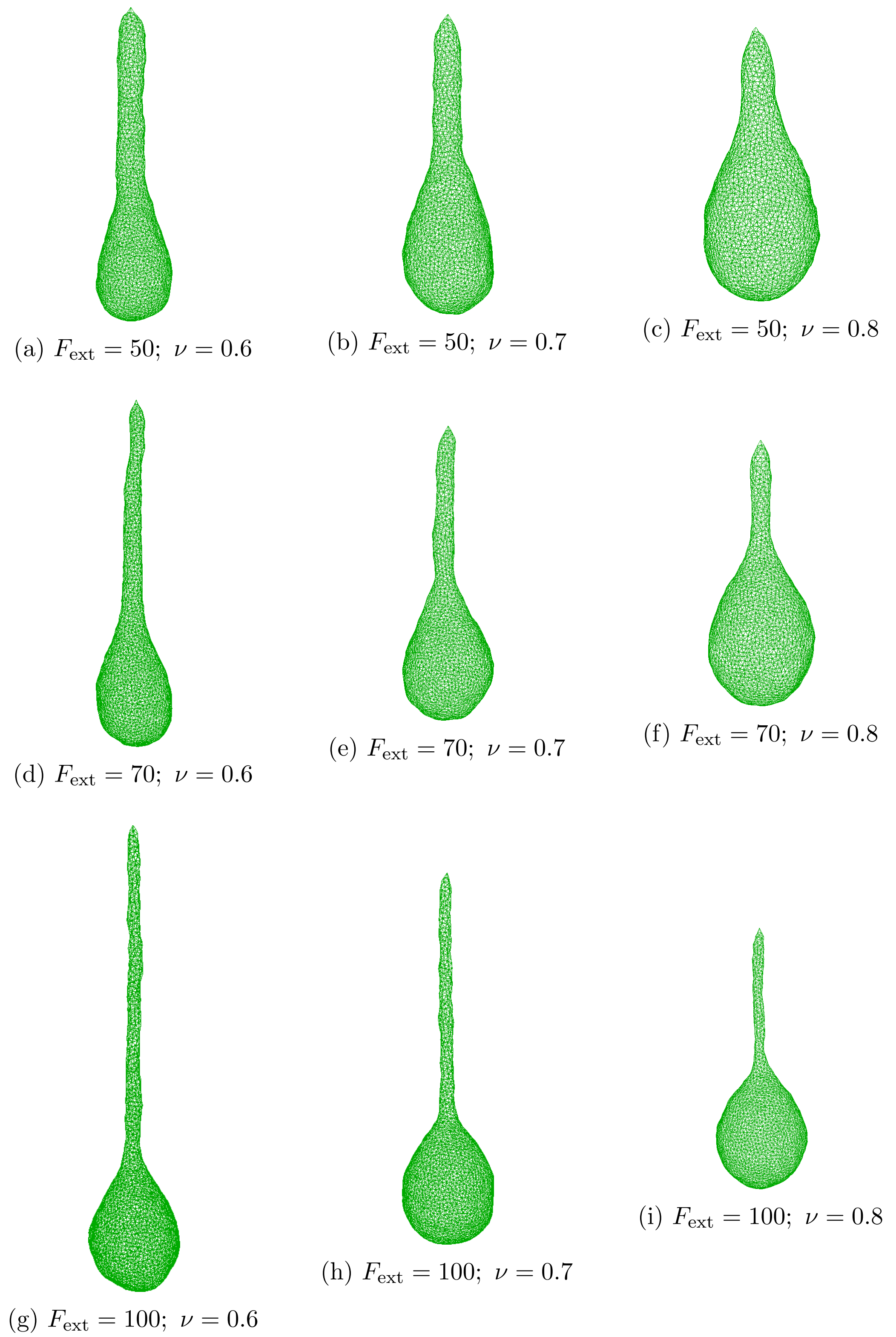

(a) $F_{\text{ext}} = 50;\ \nu = 0.6$

(b) $F_{\text{ext}} = 50;\ \nu = 0.7$

(c) $F_{\text{ext}} = 50;\ \nu = 0.8$

(d) $F_{\text{ext}} = 70;\ \nu = 0.6$

(e) $F_{\text{ext}} = 70;\ \nu = 0.7$

(f) $F_{\text{ext}} = 70;\ \nu = 0.8$

(g) $F_{\text{ext}} = 100;\ \nu = 0.6$

(h) $F_{\text{ext}} = 100;\ \nu = 0.7$

(i) $F_{\text{ext}} = 100;\ \nu = 0.8$

Figure 4.4: Final stable configurations for a vesicle with one external force applied. Shapes for different forces F_{ext} and different reduced volumes ν are shown.

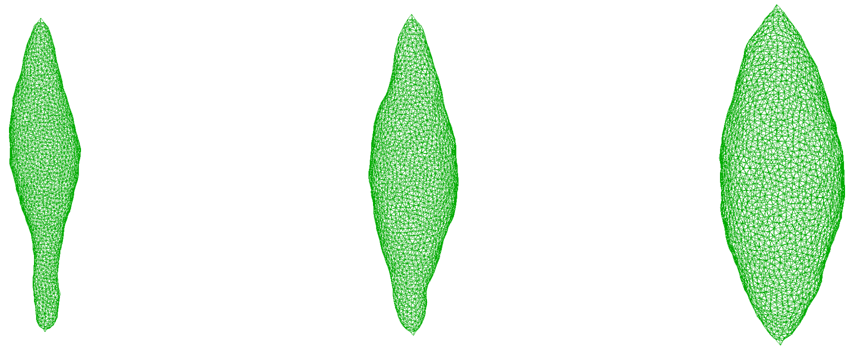

(a) $F_{\text{ext}} = 50;\ \nu = 0.6$

(b) $F_{\text{ext}} = 50;\ \nu = 0.7$

(c) $F_{\text{ext}} = 50;\ \nu = 0.8$

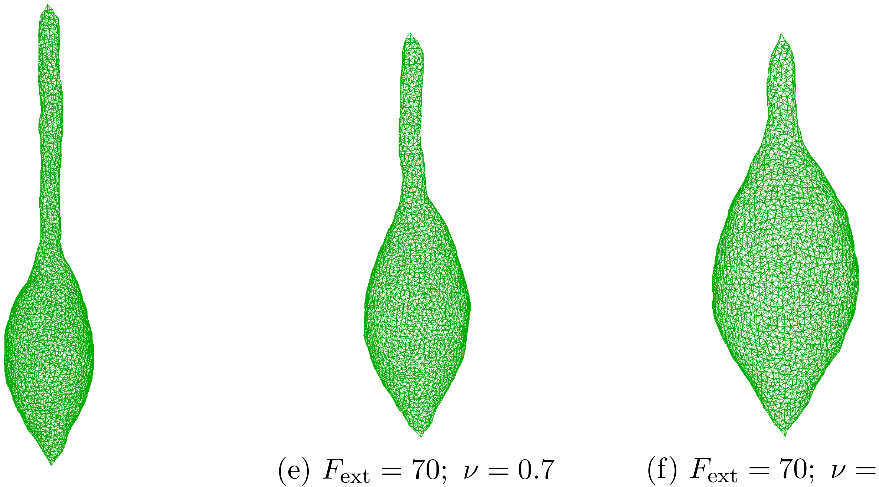

(d) $F_{\text{ext}} = 70;\ \nu = 0.6$

(e) $F_{\text{ext}} = 70;\ \nu = 0.7$

(f) $F_{\text{ext}} = 70;\ \nu = 0.8$

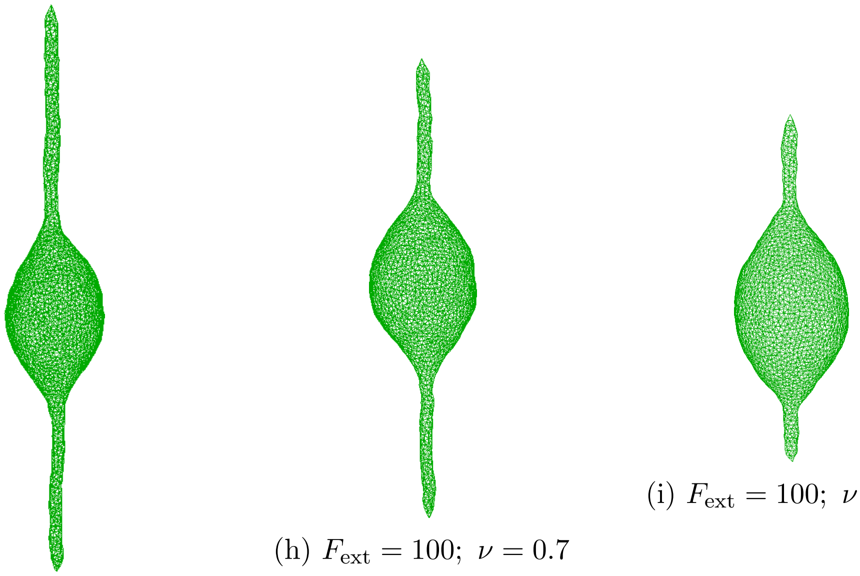

(g) $F_{\text{ext}} = 100;\ \nu = 0.6$

(h) $F_{\text{ext}} = 100;\ \nu = 0.7$

(i) $F_{\text{ext}} = 100;\ \nu = 0.8$

Figure 4.5: Final stable configurations for a vesicle with two opposing external forces applied. Shapes for different forces F_{ext} and different reduced volumes ν are shown.

It should also be noted that our simulation model works really well for forces until $F_{\mathrm{ext}} \approx 130$. For higher forces, the tubes get very thin and the maximum resolution of the triangular mesh is reached. Meaningful results can therefore only be reported for forces up to $F_{\mathrm{ext}} \approx 130$. In Section 4.8 simulations with a more detailed mesh and therefore higher resolution were performed, which confirm this estimate.

4.4 Length of the Tubes

In this section the tube length depending on the external force is investigated. First, it is analyzed how the tube length evolves over time, when the external force is applied. Then the dependence of the length of the new final stable configuration on the strength of the external force is determined. When talking about length in the subsequent sections, this actually refers to the distance between the ends of the two tubes, i.e., the distance ℓ_{T} between the two points furthest apart in the vesicle[b][c].

4.4.1 Length Evolution

It was investigated how the length of the configuration changes over time, with a constant external force applied. This evolution is shown in Figure 4.6. At first the length steadily increases until it reaches a plateau value, which indicates that the new final stable configuration is reached. As to be expected the stronger the forces, the longer the tubes are. For long times, one can also observe thermal fluctuations in the length of the final stable configuration.

In Figure 4.7 the force was increased stepwise (red curve) and afterwards decreased stepwise (blue curve). Every $t = 2000$ the force was increased or decreased by $\Delta F_{\mathrm{ext}} = 20$, starting at $F_{\mathrm{ext}} = 0$ and ending at $F_{\mathrm{ext}} = 120$. One can see that the plateau values are independent of the length of the previous configuration, thus there is no hysteresis effect.

4.4.2 Length of the Final Configuration

It was further investigated how the length of the final stable configuration, and hence the tube length, depends on the strength of the external force. For this a constant external force F_{ext} was applied and the system was simulated long enough, to ensure

---

[b] $\ell_{\mathrm{T}} = \max(\{|\vec{r}_i - \vec{r}_j|, \forall_{i,j} \in N\})$ with the positions of the vertices $\vec{r}_i$ and the total number of vertices N.

[c] To obtain the tube length one simply has to subtract the diameter of the vesicle, which is just a constant offset. We chose to work with the end-to-end distance because it was easier to handle and compare to our results obtained from direct minimization and to data from the literature.

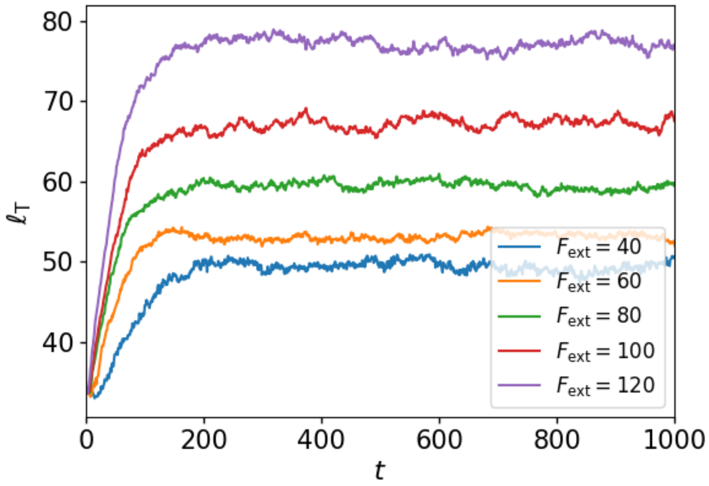

Figure 4.6: Time evolution of the length ℓ_T for different applied forces F_{ext} at $\nu = 0.8$. The starting configuration was a relaxed vesicle. The evolution looks similar for $\nu = 0.6$ and $\nu = 0.7$.

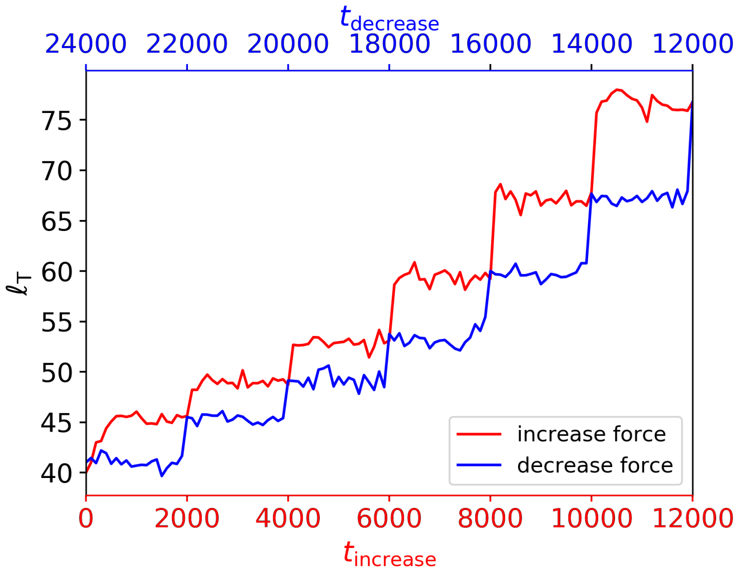

Figure 4.7: Time evolution of the length ℓ_T of the structure for increasing (t_{increase}; red curve) and then decreasing (t_{decrease}; blue curve) the force stepwise. Every $t = 2000$ the force was increased and then decreased by $\Delta F_{\text{ext}} = 20$ ($\nu = 0.8$).

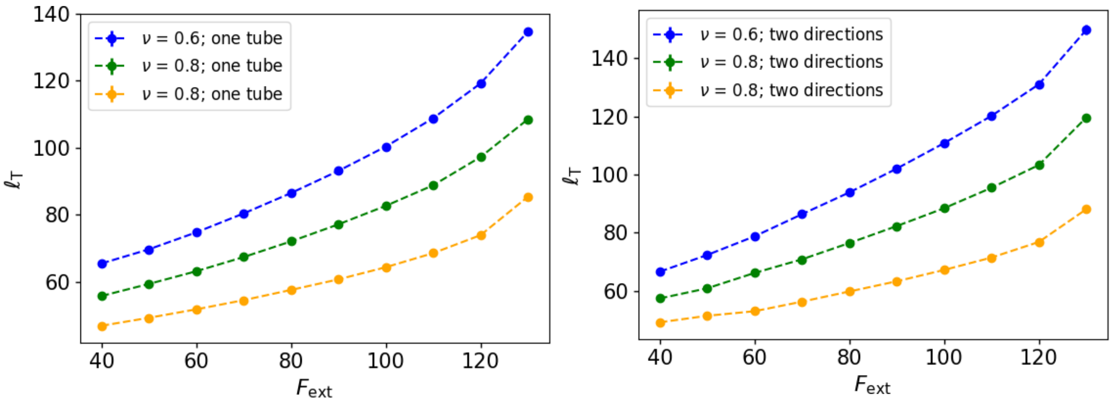

(a) Pulling in one direction.

(b) Pulling in two opposing directions.

Figure 4.8: Length ℓ_T of the stable configuration depending on the external force F_ext for pulling in one or two directions for different reduced volumes ν.

that the equilibrium configuration shown in Figure 4.6 is reached. This length dependence on the force is shown in Figure 4.8a for one tube and in Figure 4.8b for two tubes. Each data point was averaged over 100 independent runs, to minimize the effects of thermal fluctuations.

As already seen in Figure 4.6 the length increases for increasing forces. It is also interesting to see that the lengths differ depending on the reduced volumes ν. For a lower reduced volume one obtains longer structures. The effect of whether the force is applied in one or two directions on the total length is very small. The only difference is that, when pulling in two directions, the structures are slightly more elongated.

4.5 Tube Radius

In this section the radius of the tubes is studied. For this the stable final configurations obtained in the previous section were used. For each data point, it was again averaged over 100 independent configurations. The equilibrium tube radius can also be estimated theoretically and the simulation results will be compared to this theory.

4.5.1 Theoretical Tube Radius

The equilibrium tube radius R_0 can be approximated by:[25;131]

$$R_0 = \frac{2\pi\kappa}{F_\mathrm{ext}} \propto \frac{1}{F_\mathrm{ext}} \tag{4.2}$$

and only depends on the external force F_{ext} applied and the bending rigidity κ. Since κ is a material constant, the equilibrium tube radius is inversely proportional to the external force F_{ext}.

This equilibrium tube radius can directly be derived from the Helfrich Hamiltonian given in Equation 3.7, assuming a perfectly axisymmetric tube with fixed area and open ends. The derivation can be found in Appendix B.2.

4.5.2 Tube Radius from Simulations

To determine the tube radius from the simulations, the vesicle was aligned along an axis and then divided into slabs. For each slab the average radius was determined by projecting the slab onto a plane perpendicular to the alignment axis and then calculating the average distance to the center of mass of the projected vertices inside one slab. This allowed to find the contour of our system and the radius of the tubes. The division into slabs is necessary, because of small undulations of the tube due to the thermal fluctuations, and also useful to remove any contributions from the vesicular part.

An exemplary contour is shown in Figure 4.9. The red data points represent the vertices and the blue line the contour determined with the method described above. To calculate the tube radius, it was averaged over the radii in the tubular part of the structure.

A comparison between the theoretically predicted tube radius and the results obtained by simulations is shown in Figures 4.10a and 4.10b. As predicted by the theory the radius decreases with increasing force. For lower forces the simulation results are, however, slightly higher than predicted. For intermediate forces the agreement is quite good and for higher forces the simulation results are a bit too low.

The deviations for low forces could be due to the fact that the tubes are not yet too pronounced and have a slight 'lemon' shape, which would result in a larger radius.

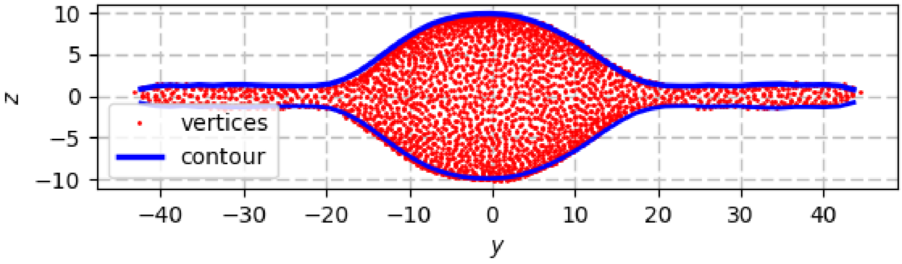

Figure 4.9: Determination of the vesicle contour (blue line). The red points are the vertices of the vesicle. This contour can be used to determine the average tube radius ($\nu = 0.7$; $F_{\text{ext}} = 100$).

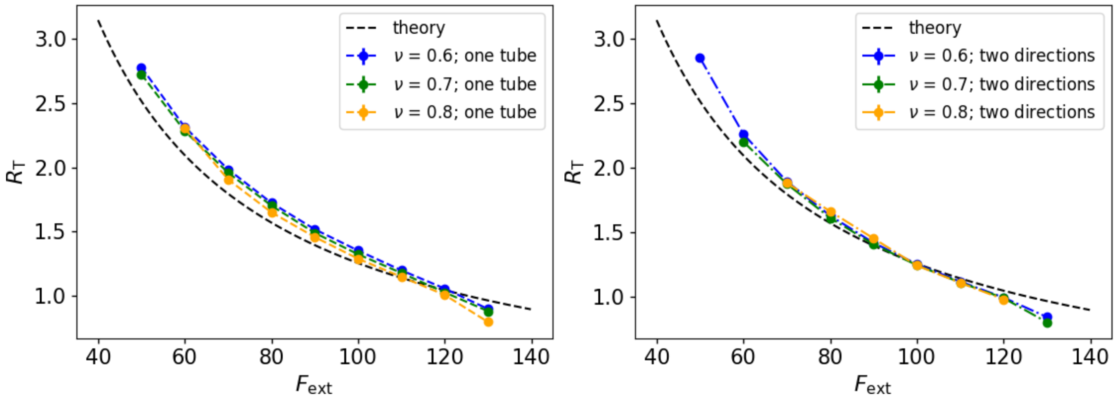

(a) Pulling in one direction.

(b) Pulling in two directions.

Figure 4.10: Tube radius R_{T} of the final configuration for different external forces F_{ext}. Shown is the theoretical prediction according to Equation 4.2 (black curve) and our simulation results for the different reduced volumes ν.

For high forces, the resolution of the mesh is reached, as mentioned previously. This also shows that for obtaining meaningful results, one should not perform simulations for forces higher than $F_{\mathrm{ext}} \approx 130$.

Overall the agreement between theory and simulations is quite good. The simulations show the same trend as predicted by the theory and are relatively close to the predicted values. One has to, however, be careful with the interpretation of the results for too high forces, as discussed above.

4.6 Energies of the System

It is also interesting to study the energies of the different configurations discussed above. In the following the different energy contributions described in Section 3.4.1 are analyzed. In Figure 4.11 the time-dependent energy is shown for an initially relaxed vesicle to which an external force is applied. When applying the force, the vesicle immediately starts to deform and hence the curvature energy increases, until the system has reached the new final stable configuration. The work necessary to reach this energetically higher state was generated by the external force as defined in Equation 3.15. This work will be analyzed in more detail in Section 7.3.

One can clearly see that the energy of the system U_{tot} (black) is dominated by the curvature energy U_{cv} (red). All other energies give a small, roughly constant contribution. The energies from the bond and pair potential (U_{bond} in turquoise and U_{rep} in orange) are in the order of 200 and the energies due to the volume and area potential (U_{V} in blue and U_{S} in green) in the order of 10. The small fluctuations in the energy are again due to thermal fluctuations.

When analyzing the curvature energy of the final stable configurations for different

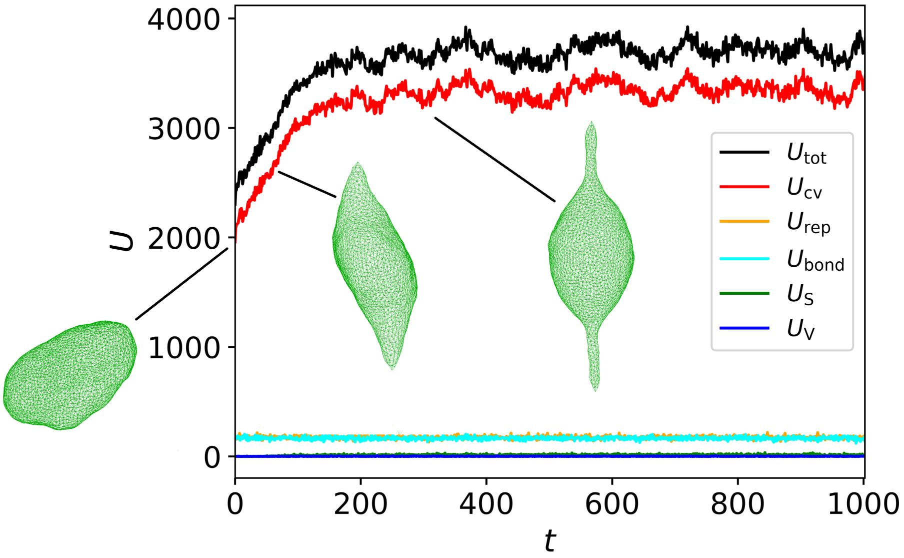

Figure 4.11: Time evolution of the energies U when applying an external force $F_{\mathrm{ext}} = 100$ to a relaxed vesicle ($\nu = 0.8$). The total energy of the system U_{tot} (black) is dominated by the curvature energy U_{cv} (red). The inserts show the conformation of the system.

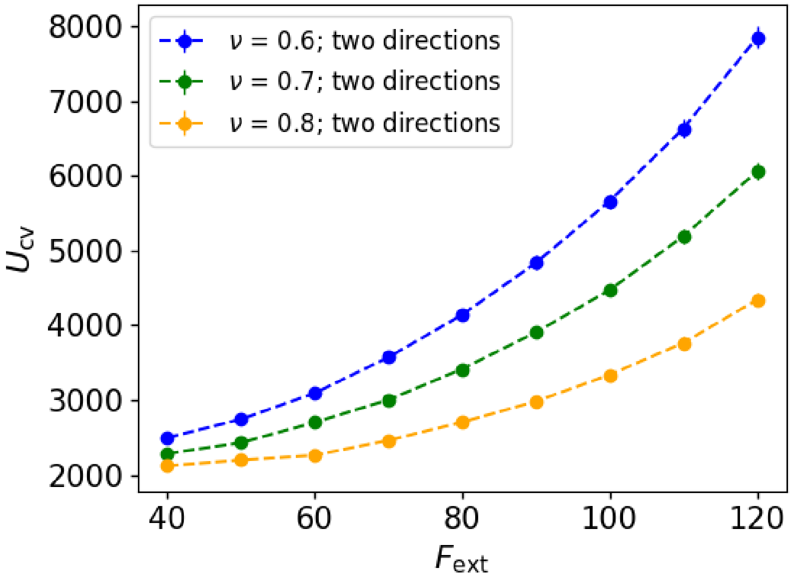

Figure 4.12: Curvature energy U_{cv} of the final stable configurations for different forces F_{ext}, pulling in two directions, and different reduced volumes ν. The data looks similar for pulling in one direction.

forces, one expects an increase with increasing force. This is the case, because the stronger the force, the longer and thinner the tubes get, and hence the system is curved more strongly. This is confirmed by the data shown in Figure 4.12. For all reduced volumes the curvature energy increases for increasing forces. It is highest for $\nu = 0.6$, in which case the vesicle was deformed the most and had the longest tubes.

This shows that the curvature energy is the most dominant energy contribution and hence an important characteristic of the system. It will be closely monitored and is an important quantity for further studies.

4.7 Other Membrane Parameters

In this section we studied several other membrane parameters, namely the surface pressure Π, the Laplace surface tension γ and the pressure difference between the inside and the outside of the vesicle ΔP. In the following these parameters will be briefly motivated and it will be analyzed how they behave in our system.

Pressure Difference ΔP

The volume of the vesicle is constrained by the harmonic potential $U_{\mathrm{V}} = \frac{1}{2}k_{\mathrm{V}}(V - V_0)^2$, c.f. Equation 3.13. Therefore the pressure difference is given by:

$$\Delta P = -k_{\mathrm{V}}\langle V - V_0 \rangle = p_{\mathrm{in}} - p_{\mathrm{out}} \tag{4.3}$$

with the volume constraint parameter $k_{\mathrm{V}} = 1.0$, the volume of the vesicle V and the target volume V_0. p_{in} is the pressure inside and p_{out} the pressure outside of the vesicle.

The pressure difference for the different reduced volumes, for pulling in two opposing directions, is shown in Figure 4.13. One can observe that the pressure inside the vesicle is larger than outside and that the pressure difference increases steadily with increasing force. The fluctuations are relatively high, which is due to the (small) fluctuations of the volume. The volume constraint parameter k_{V} was set to one in these simulations. For a more stable volume, one would need to increase the value of k_{V}.

Surface Pressure Π

Similarly to the pressure difference, the surface pressure can be derived from the constraints on the surface area $U_{\mathrm{S}} = \frac{1}{2}k_{\mathrm{S}}(A - A_0)^2$, c.f. Equation 3.12:

$$\Pi = -k_{\mathrm{S}}\langle A - A_0 \rangle \tag{4.4}$$

In the simulations the area constraint parameter was $k_{\mathrm{S}} = 2.0$, A it the surface area of the vesicle and A_0 the target surface area.

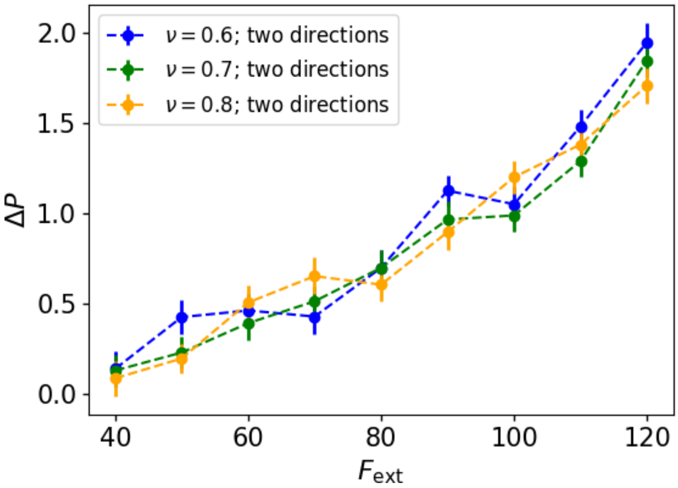

Figure 4.13: Pressure difference ΔP between the inside and the outside of the vesicle depending on the external force F_{ext}, for different reduced volumes ν.

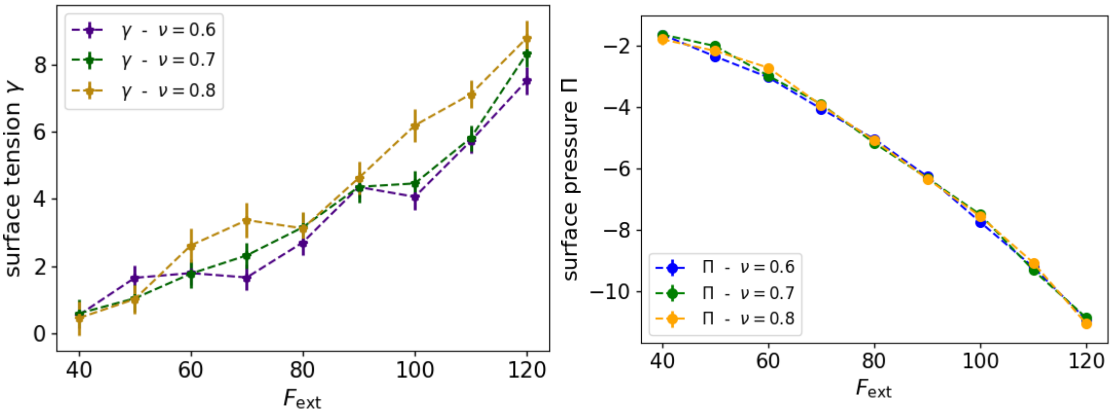

(a) Laplace surface tension γ.

(b) Surface pressure Π.

Figure 4.14: Laplace surface tension γ and surface pressure Π in the final configuration depending on the external force F_{ext} for different reduced volumes ν.

Laplace Surface Tension γ

The Laplace surface tension γ can be derived from the Young-Laplace equation,[132;133] which directly relates it to ΔP:

$$\Delta P = p_{\text{in}} - p_{\text{out}} = \frac{2}{R_C}\gamma \tag{4.5}$$

with

$$R_C = \frac{3V}{A} \tag{4.6}$$

being the effective thermodynamic radius for any closed vesicle.[134]

Using these equations the Laplace surface tension can be expressed as:

$$\gamma = \Delta P \frac{3V}{2A} \tag{4.7}$$

The behavior of both the Laplace surface tension and the surface pressure can be found in Figure 4.14. The absolute values for both quantities increase with increasing force, where the Laplace surface tension is slightly above the surface pressure, however, they have different signs.

4.8 Larger Number of Vertices

To verify that the number of vertices N used, i.e. the discretization of the mesh, is fine enough to properly resolve the investigated tubular vesicles, simulations with a larger number of vertices were performed. The number of vertices was increased to $N = 10242$. This evidently slows down the simulations significantly, which is why this setting was only used for control runs and not for performing the entire analysis.

First, the time evolution of the length of the system was analyzed, when applying a constant external force. This evolution can be found in Figure 4.15. Similar to the simulations with smaller N (c.f. Figure 4.6), the length increases until a new stable final configuration is reached and the length is roughly constant. Values from this new equilibrium region will be used to compare them to the simulations with smaller N.

In order to compare the two systems quantitatively, the values for the lengths and forces had to be rescaled, because in the simulations the bond length a is set to one, which leads to an increased system size for larger numbers of vertices $N = 10242$. Since we require them to have the same size, we rescale the unit of length $\sigma_{N=10242} = \sqrt{A_0^{N=10242}/A_0^{N=2562}} = 2$ (and similarly the unit of time $\tau_{N=10242}$). This rescaling can be safely performed because the systems investigated are scale invariant. After rescaling some of the units are not equal to one anymore, therefore we will explicitly state the units until the end of this section.

A comparison between the lengths and the tube radii can be found in Figures 4.16a and 4.16b. Both generally show a good agreement for lower forces, but for forces larger than $F_{\text{ext}} \approx 130\kappa\sigma_N^{-1}$ there are large deviations. This is exactly the region where the resolution of the $N = 2562$ mesh becomes insufficient, as discussed before. For forces lower than $F_{\text{ext}} \approx 130\kappa\sigma_N^{-1}$ the lengths and radii for $N = 2562$ are slightly above the values for $N = 10242$. The deviations are, however, relatively small, so the effect of the discretization in this region is quite small.

For the simulations with $N = 10242$ the agreement of the tube radius with the theoretical values is very good until $F_{\text{ext}} \approx 220\kappa\sigma_N^{-1}$. For higher forces, the resolution of the mesh becomes insufficient, which is also confirmed by analyzing simulation snapshots. As a rough estimate, simulations with $N = 10242$ could thus be used for forces of up to $F_{\text{ext}} \approx 210 - 220\kappa\sigma_N^{-1}$.

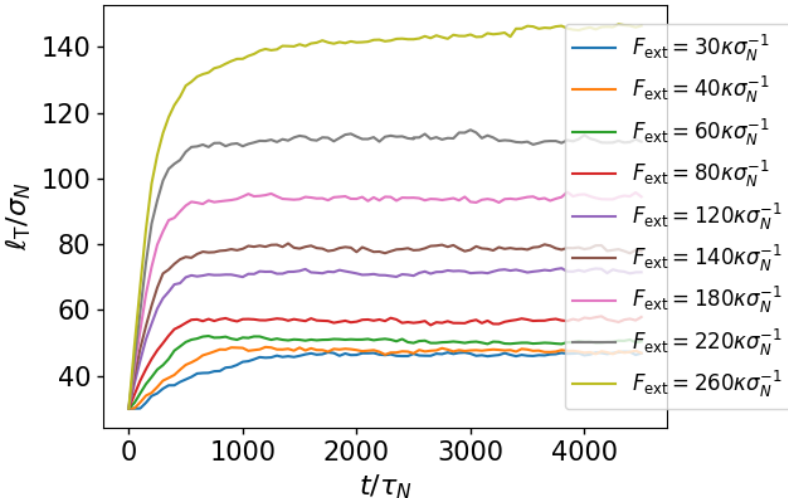

Figure 4.15: Time evolution of the rescaled length ℓ_{T} when applying a rescaled external force F_{ext} for a larger number of vertices $N = 10242$ ($\nu = 0.8$). (The values were rescaled to match the simulation with $N = 2562$ vertices, as described in the text.)

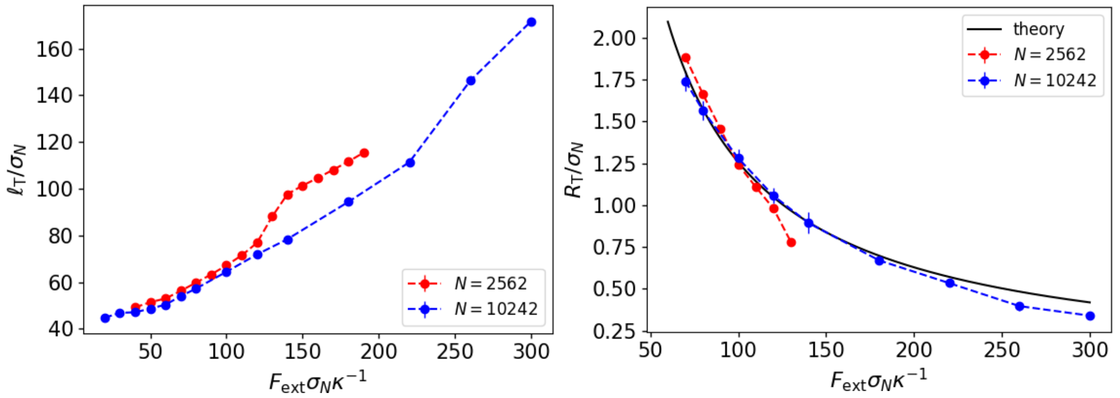

(a) Length

(b) Radius

Figure 4.16: (Rescaled) length ℓ_{T} and tube radius R_{T} obtained for different (rescaled) forces F_{ext} from simulations with $N = 2562$ (red) and $N = 10242$ (blue) vertices. The theory corresponds to Equation 4.2. (The values were rescaled to match the simulation with $N = 2562$ vertices, as described in the text.)

Finally, the contours of the two systems were compared. This is exemplarily shown in Figure 4.17 for three different forces. Generally the agreement is very good. There is only a slight deviation in the total length of the structures. As observed before, the contours for $N = 10242$ are slightly shorter than for $N = 2562$.

From this analysis it can be concluded that a finer discretization leads to slightly more accurate results. For performing simulations with $F_{\mathrm{ext}} > 130\kappa\sigma_N^{-1}$ the finer discretization with $N = 10242$ is necessary to obtain meaningful results. For forces $F_{\mathrm{ext}} < 130\kappa\sigma_N^{-1}$ the smaller mesh with $N = 2562$ is sufficient. Since the focus of this work lies on the regime $F_{\mathrm{ext}} < 130\kappa\sigma_N^{-1}$, only the discretization with $N = 2562$ will be used in the following.

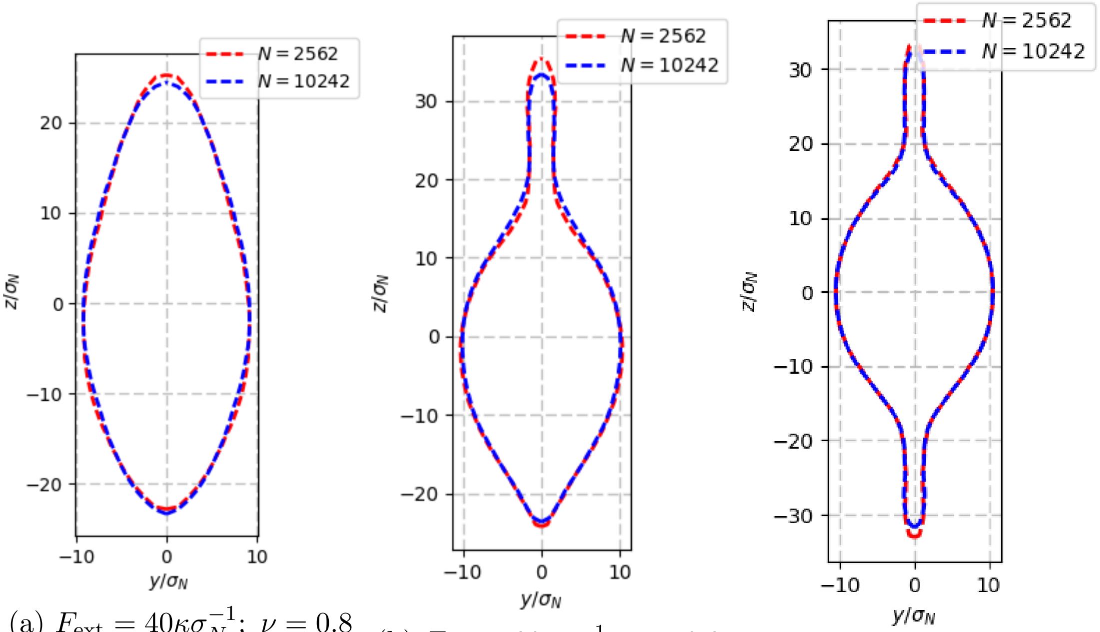

(a) $F_{\text{ext}} = 40\kappa\sigma_N^{-1};\ \nu = 0.8$ (b) $F_{\text{ext}} = 80\kappa\sigma_N^{-1};\ \nu = 0.8$ (c) $F_{\text{ext}} = 100\kappa\sigma_N^{-1};\ \nu = 0.8$

Figure 4.17: Comparison between the contours of simulations with $N = 2562$ (red) and $N = 10242$ (blue) vertices for different (rescaled) external forces F_{ext}. (The values were rescaled to match the simulation with $N = 2562$ vertices, as described in the text.)

4.9 Discussion of the Results

Performing simulations using a dynamically-triangulated surface model enabled us to model tube formation on closed spherical vesicles due to an external pulling force. The results obtained for the tubular structures show a good agreement with theoretical predictions. The model was further validated by performing simulations with a finer discretization, showing that the model can reliably be applied for external forces of up to $F_{\text{ext}} \approx 130$. Our analysis thus indicates that the quality of the numerical results can be systematically improved using finer discretizations, as shown in Ref. 112. From this analysis we would assume that all deviations from the theory could be caused by discretization effects due to the finite number of vertices N.

The simulations also showed that an important quantity of the system is its curvature energy. It is the dominant and most important contribution to the total energy of the system. It will be a relevant quantity for further analysis and monitored closely. The curvature energy of the vesicles is currently higher than in an idealized system, due to undulations of the surface caused by thermal fluctuations. To reduce the effects of these fluctuations, simulations at low temperatures will be performed.

This first analysis showed that the simulation model is well suited for modeling and analyzing vesicular and tubular structures. To further validate the model, minimal-energy solutions of the Helfrich Hamiltonian, which allow to analyze shapes of vesicles with an external force applied, will be calculated. This method will be presented in the next chapter and the results compared to the simulations.

5

Analytical Solutions of Axisymmetric Tube-Forming Vesicles

To validate the simulation method and results, the problem of obtaining tubular structures pulled from vesicles was described and investigated analytically and compared to the results obtained in the previous section. In the literature several such analytical approaches can be found, e.g. different approaches solving the shape equations derived from the Helfrich theory described in Section 3.3, see Refs. 25; 135–145. Other approaches used purely dissipative dynamics,[146] interior-point-methods[147;148] or a more direct approach that directly minimizes a target function.[149;150]

These methods were originally applied to a simple vesicle to calculate the shapes of red blood cells or other general shapes, see Refs. 136; 139; 141–145; 151; 152. There have also been several approaches made to investigate the formation of tubular structures protruding from vesicles. However, in Refs. 25 and 135 only the tubular part was considered, while in Ref. 153 the tubular part and the vesicle were analyzed separately. Our objective in this work, is to treat the tubes and the vesicles as a combined system. This has been done in Refs. 146–148, where a nanorod was put into the vesicle to mimic e.g. actin filaments, while others used an external force.[138;149;150;154;155] The latter is what has been done in this thesis.

First, the more traditional approach of solving the shape equations will be discussed. This approach, however, has some strong limitations for more complex structures. We therefore had to switch to a more direct method, which allows to minimize the energy of a deformed vesicle. This method performed very well and we were able to obtain stable results. These will be compared to the simulation results and data from the literature.

5.1 Shape Equations

As described in Section 3.3 the bending energy of a vesicle can be described by the following equation:

$$E_{\text{bend}} = \frac{\kappa}{2} \int \mathrm{d}A (K - K_0)^2 \tag{5.1}$$

where K and K_0 are the mean and spontaneous curvature respectively. κ is a material constants called curvature modulus.

The energetically most favorable conformation of a structure can in principle be obtained by minimizing this equation under certain constraints that describe the state of the system, i.e. constraints on the total area and volume of the vesicle. As mentioned previously, it is however generally not possible to find an analytical solution for this minimization problem. One therefore has to make simplifications, taking properties of the system, like symmetries, into account. In the following the simplifications that can be made for a closed (spherical) vesicle and a convenient parameterization will be presented. Both the bending energy and the constraints will be expressed in this parametrization.

5.1.1 Parametrization

In the following the vesicle tube system is assumed to be axisymmetric. This seems to be a good approximation, as shown by the simulations performed in the previous chapter, and it can also be understood from the fluidity of the membrane, which automatically aligns the symmetry axis of the vesicle with the direction of the external force. The system can therefore be parameterized by the arc length S of the contour of the vesicle and the angle $\psi(S)$ between the tangent and the x-axis as illustrated in Figure 5.1. Similar parameterizations have previously been used in e.g. Refs. 139; 151.

The parameterization of the vesicle is therefore given by:

$$r(S,\phi) = \begin{pmatrix} x(S)\cos(\phi) \\ x(S)\sin(\phi) \\ z(S) \end{pmatrix} \tag{5.2}$$

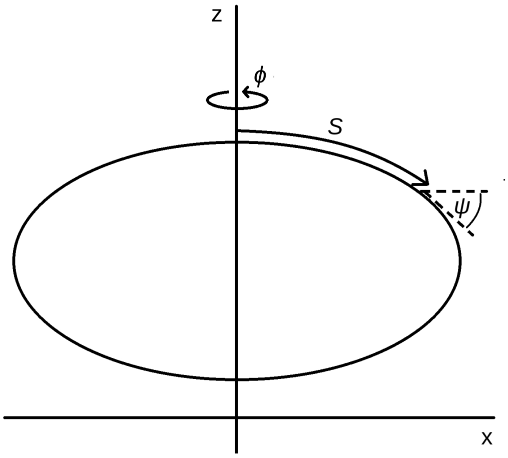

Figure 5.1: Illustration of the parameterization used for the vesicle. The system is axisymmetric and characterized by the arc length S and the angle $\psi(S)$.

where the following geometrical relations are required to hold:

$$\dot{x} = \frac{\partial x}{\partial S} = \cos(\psi) \tag{5.3}$$

$$\dot{z} = \frac{\partial z}{\partial S} = -\sin(\psi) \tag{5.4}$$

In this and all further expressions the dot denotes the derivative with respect to S.

Using this parameterization, the mean curvature and the differential dA can be expressed in the following way:[139;151]

$$K = \frac{\sin(\psi)}{x} + \dot{\psi} \tag{5.5}$$

$$\mathrm{d}A = x\mathrm{d}\phi\mathrm{d}S \tag{5.6}$$

A detailed derivation of these equations can be found in Appendix B.3. The term that has to be minimized therefore simplifies to:

$$E(\psi, x, z) = \frac{\kappa}{2}\int (K - K_0)^2 \mathrm{d}A = \kappa \int_0^{2\pi}\int_{S_0}^{S_1} \frac{x}{2}\left(\frac{\sin\psi}{x} + \dot{\psi} - K_0\right)^2 \mathrm{d}S\mathrm{d}\phi \tag{5.7}$$

$$= 2\pi\kappa \int_{S_0}^{S_1} \frac{x}{2}\left(\frac{\sin\psi}{x} + \dot{\psi} - K_0\right)^2 \mathrm{d}S \tag{5.8}$$

5.1.2 Shape Equations

To mimic the simulations performed in the previous section, Equation 5.8 has to be minimized, while keeping the area A and the volume V of the vesicle constant. In the given parameterization A and V can be expressed as:

$$A = 2\pi \int_{S_0}^{S_1} x\mathrm{d}S \tag{5.9}$$

$$V = \pi \int_{S_0}^{S_1} x^2 \sin\psi \mathrm{d}S \tag{5.10}$$

By introducing Lagrange multipliers Σ and P and by solving $\delta F = \delta(E + \Sigma A + PV) = 0$, with the variation δ, the shape equations can now be obtained.[143;151] However, the earlier considered constraints $\dot{x} = \cos(\psi)$ and $\dot{z} = -\sin(\psi)$ also need to be taken into account. To obtain this the Lagrange functions $\gamma(S)$ and $\eta(S)$ are introduced.

In the simulations an external force is pulling on the poles of the vesicle in opposing directions. This is described by a 'force' f, which acts on the length of the vesicle, i.e. $z(S_1) - z(S_0)$. Here f is in fact a Lagrange multiplier.

The shape equations for a general vesicle with external pulling force can now be obtained by demanding that the following function has zero variation:

$$\begin{aligned}
F(\psi, x, z, \gamma, \eta) &= E(\psi, x, z) + \varSigma A + PV + f(z(S_1) - z(S_0)) \\
&\quad + 2\pi\kappa \int_{S_0}^{S_1} \left[\gamma(\dot{x} - \cos\psi) + \eta(\dot{z} + \sin\psi)\right] \mathrm{d}S \\
&= 2\pi\kappa \int_{S_0}^{S_1} \left[\frac{x}{2}\left(\frac{\sin\psi}{x} + \dot{\psi} - K_0\right)^2 + \bar{\varSigma} x + \frac{\bar{P}}{2} x^2 \sin\psi \right. \\
&\quad \left. - \bar{f}\sin\psi + \gamma(\dot{x} - \cos\psi) + \eta(\dot{z} + \sin\psi)\right] \mathrm{d}S \\
&=: 2\pi\kappa \int_{S_0}^{S_1} L \mathrm{d}S
\end{aligned} \tag{5.11}$$

Three rescaled parameters were introduced:

$$\bar{\varSigma} = \frac{\varSigma}{\kappa}, \quad \bar{P} = \frac{P}{\kappa} \quad \text{and} \quad \bar{f} = \frac{f}{2\pi\kappa} \tag{5.12}$$

Using the variational principle one can now derive the following set of differential equations (derivation see Appendix B.3):

$$\ddot{\psi} = \frac{\sin\psi\cos\psi}{x^2} + \frac{\bar{P}x}{2}\cos\psi + \gamma\frac{\sin\psi}{x} + \eta\frac{\cos\psi}{x} - \frac{\dot{\psi}\cos\psi}{x} - \bar{f}\frac{\cos\psi}{x} \tag{5.13}$$

$$\dot{\gamma} = \frac{1}{2}(\dot{\psi} - K_0)^2 - \frac{\sin^2\psi}{2x^2} + \bar{\varSigma} + \bar{P}x\sin\psi \tag{5.14}$$

$$\dot{\eta} = 0 \tag{5.15}$$

$$\dot{x} = \cos\psi \tag{5.16}$$

$$\dot{z} = -\sin\psi \tag{5.17}$$

Considering a closed axisymmetric vesicle and taking boundary conditions into account, these equations simplify to:

$$\ddot{\psi} = \frac{\sin\psi\cos\psi}{x^2} + \frac{\bar{P}x}{2}\cos\psi + \gamma\frac{\sin\psi}{x} - \frac{\dot{\psi}\cos\psi}{x} - \bar{f}\frac{\cos\psi}{x} \tag{5.18}$$

$$\dot{\gamma} = \frac{1}{2}(\dot{\psi} - K_0)^2 - \frac{\sin^2\psi}{2x^2} + \bar{\varSigma} + \bar{P}x\sin\psi \tag{5.19}$$

$$\dot{x} = \cos\psi \tag{5.20}$$

$$\dot{z} = -\sin\psi \tag{5.21}$$

with the following initial conditions:

$$\psi(0) = 0;\ \psi(S_1) = \pi \tag{5.22}$$

$$\gamma(0) = \gamma(S_1) = 0 \tag{5.23}$$

$$x(0) = x(S_1) = 0 \tag{5.24}$$

To solve these equations numerically an additional variable $U = \dot{\psi}$ is introduced. This reduces the system to a set of five first order differential equations.

Before one can now solve these equations, there is one more small problem with the boundary conditions that has to be considered. At $S = 0$ it is required that $x(0) = 0$, which leads to a division by zero in Equation 5.18. To circumvent this the following new initial conditions $\psi(0) = \epsilon$ and $x(0) = \frac{\sin\epsilon}{U(0)}$, with $\epsilon > 0$ and arbitrarily small, are introduced. The resulting equations we are attempting to solve are thus given by:

$$\dot{\psi} = U \tag{5.25}$$

$$\dot{U} = \frac{\sin\psi\cos\psi}{x^2} + \frac{\bar{P}x}{2}\cos\psi + \gamma\frac{\sin\psi}{x} - \frac{U\cos\psi}{x} - \bar{f}\frac{\cos\psi}{x} \tag{5.26}$$

$$\dot{\gamma} = \frac{1}{2}(\dot{\psi} - K_0)^2 - \frac{\sin^2\psi}{2x^2} + \bar{\Sigma} + \bar{P}x\sin\psi \tag{5.27}$$

$$\dot{x} = \cos\psi \tag{5.28}$$

$$\dot{z} = -\sin\psi \tag{5.29}$$

with the modified initial conditions:

$$\psi(0) = \epsilon \tag{5.30}$$

$$U(0) = u \tag{5.31}$$

$$\gamma(0) = 0 \tag{5.32}$$

$$x(0) = \frac{\sin\epsilon}{u} \tag{5.33}$$

$$z(0) = 0 \tag{5.34}$$

5.2 Solutions of the Shape Equations

We have numerically solved the shape equations given by Equations 5.25-5.34 above. First, we looked at some simple structures without an external force and then added the external force, to see whether the formation of tubular structures can be observed. For this analysis the software Mathematica[156] was used, as well as my own implementation of a Runge-Kutta[157;158] method. Both solvers led to the same results.

Without an external force it was relatively easy to obtain some simple basic shapes, as shown in Figure 5.2. These also match the shapes obtained with our simulations very well, c.f. Figure 4.1. The solutions were, however, very unstable. A slight variation in one of the initial conditions could lead to a crash of the solver, or obscure and unphysical shapes. These instabilities were also reported in Refs. 138 and 154, in which the tubular part of a tube protruding from a vesicle was approximated. When trying to reproduce the results for one-component membranes in Ref. 143 a slight variation of the initial conditions led to contradicting results.

These instabilities were even worse, when the term including the external force $\bar{f}$ was added and it was not possible to find stable meaningful solutions with a tubular part. It is of course possible that we simply did not explore a large enough fraction of the parameter space and a more detailed scan would have led to a set of parameters that provided a sensible solution. However, even if we had found one set of parameters that somehow resembled a tubular vesicle, this would not have been satisfactory. What we had hoped to obtain was a stable system or parameter range, where increasing $\bar{f}$ would lead to more elongated structures. However, due to the instabilities observed, caused by small variations of the initial parameters, this did not seem possible and plausible.

Another problem of this approach is that the area and volume are only controlled by Lagrange multipliers, which are a priori unknown. They therefore have to be adjusted in an optimization procedure to meet the area and volume constraints. Similar to previous work[138] this was done manually, while also more complicated methods exist.[155] However, as in the simulations, we want to keep the volume and

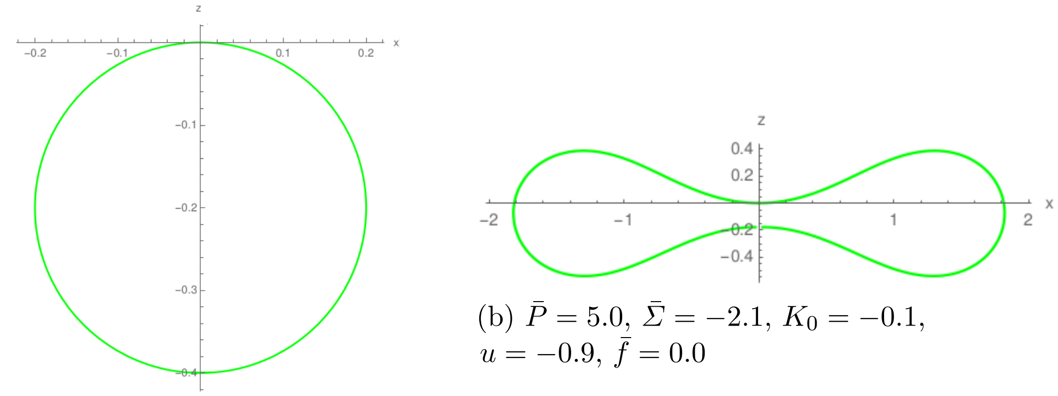

(a) $\bar{P} = 5.0$, $\bar{\Sigma} = -1.0$, $K_0 = -0.1$, $u = 5.0$, $\bar{f} = 0.0$

(b) $\bar{P} = 5.0$, $\bar{\Sigma} = -2.1$, $K_0 = -0.1$, $u = -0.9$, $\bar{f} = 0.0$

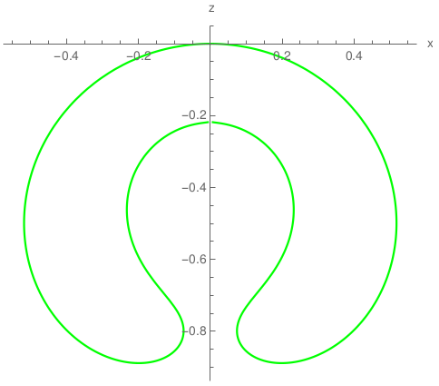

(c) $\bar{P} = 5.0$, $\bar{\Sigma} = -1.0$, $K_0 = -0.1$, $u = 1.88$, $\bar{f} = 0.0$

Figure 5.2: Numerical solutions of the shape equations given by Equations 5.25-5.34 without an external force. The parameters used can be found in the captions ($\epsilon = 10^{-25}$).

area (almost) constant and have better control over these parameters. We therefore changed our method to a technique that allows to do this, as will be discussed in the next section.

5.3 Direct Minimization

Due to the difficulties encountered in the previous section, we changed our approach to a more direct method. The objective is the minimization of the energy functional given in Equation 5.8 with an external force:

$$E(\psi, x, z) = 2\pi\kappa \int_{S_0}^{S_1} \left[\frac{x}{2} \left(\frac{\sin\psi}{x} + \dot{\psi} - K_0 \right)^2 - \frac{f}{2\pi\kappa} \sin\psi \right] \mathrm{d}S \tag{5.35}$$

$$= 2\pi\kappa \int_{S_0}^{S_1} \bar{L} \mathrm{d}S \tag{5.36}$$

At the same time we want to keep the area A and volume V of the vesicle fixed. Therefore two additional terms in the form of harmonic potentials are introduced, that are taken into account during the minimization. The resulting energy functional that has to be minimized is therefore:

$$E = 2\pi\kappa \underbrace{\int_{S_0}^{S_1} \bar{L} \mathrm{d}S}_{\text{Lagrange term}} + \underbrace{\frac{1}{2} k_{\mathrm{A}} (A - A_0)^2 + \frac{1}{2} k_{\mathrm{V}} (V - V_0)^2}_{\text{Mayer term}} \tag{5.37}$$

A_0 and V_0 are the target values for the area and volume respectively and k_{A} and k_{V} are constants determining the strength of the constraints. Minimizing this type of equation is called a Bolza problem[a], containing a Lagrange and a Mayer term. The Lagrange term falls into the same category as the term in the previous section, but the area and volume constraint are treated differently. In fact, this approach directly corresponds to the area and volume potentials introduced for the simulations (see Section 3.4.1).

To describe the axisymmetric vesicle tube system, the aforementioned constraints still need to hold. Therefore the following constraints in the form of differential equations have to be added:

$$\dot{\psi} = u \tag{5.38}$$

$$\dot{x} = \cos\psi \tag{5.39}$$

$$\dot{z} = -\sin\psi \tag{5.40}$$

$$\dot{V} = \pi x^2 \sin\psi \tag{5.41}$$

$$\dot{A} = 2\pi x \tag{5.42}$$

---

[a] This type of problem was first formulated by the German mathematician O. Bolza in 1913.[159]

Equations 5.41 and 5.42 are directly derived from Equations 5.10 and 5.9. This type of problem is called an optimal control problem (OCP).[160]

To solve this problem we used the open source software environment ACADO Toolkit[b].[161;162] This software package is specialized on optimal control problems and provides algorithms for solving them, which makes it ideally suited for our problem. Our implementation of the equations can be found in Appendix D. The results of the numerical minimization and a comparison to the simulations can be found in the next section.

5.4 Results from the Direct Minimization

5.4.1 No External Forces

First, the algorithm was tested without an external force. It performed very well as shown in Figure 5.3. Similar prolate, oblate and stromatocyte shapes as observed in simulations and calculated from solving the shape equations could be obtained, c.f. Figures 4.1 and 5.2.

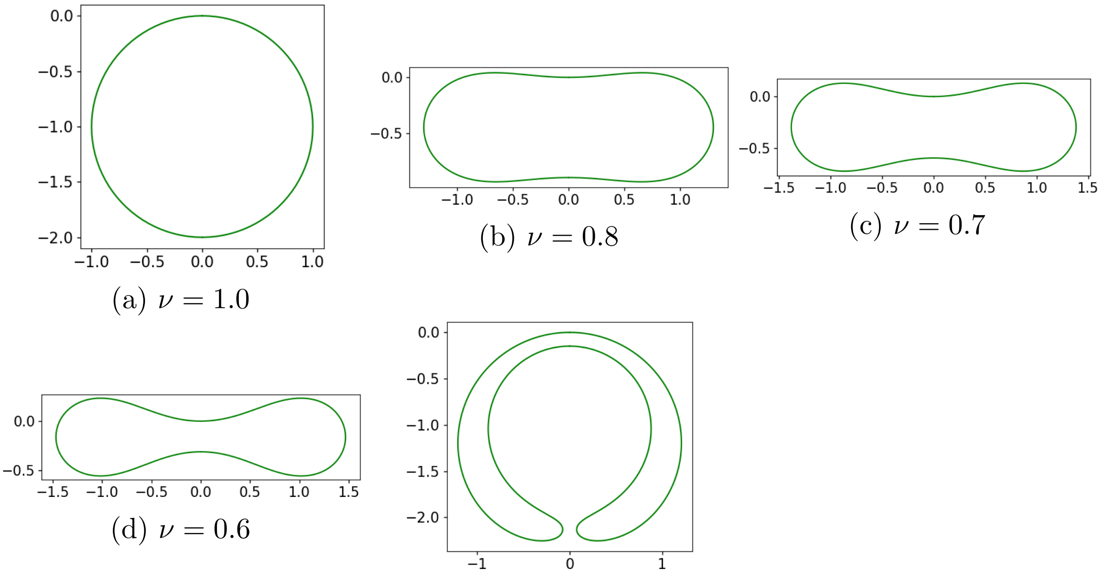

(a) $\nu = 1.0$

(b) $\nu = 0.8$

(c) $\nu = 0.7$

(d) $\nu = 0.6$

(e) $\nu = 0.3$

Figure 5.3: Numerical solutions of the direct minimization method without an external force. The system was tested for different reduced volumes ν.

---

[b] More information about the software can be found under `http://www.acadotoolkit.org/`.

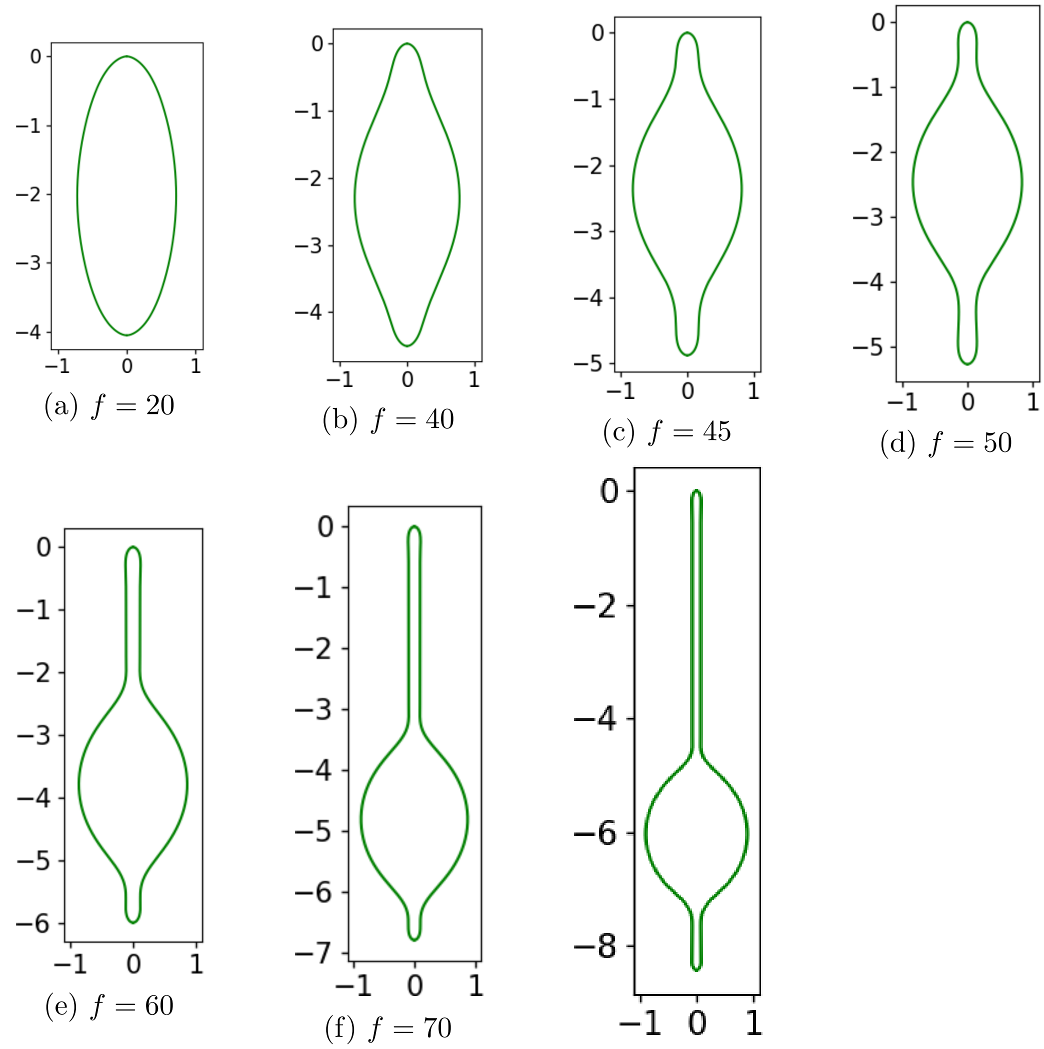

(a) $f = 20$ (b) $f = 40$ (c) $f = 45$ (d) $f = 50$

(e) $f = 60$ (f) $f = 70$ (g) $f = 90$

Figure 5.4: Shapes obtained from direct minimization for different forces f. If the forces are strong enough, tubular structures form ($\nu = 0.8$).

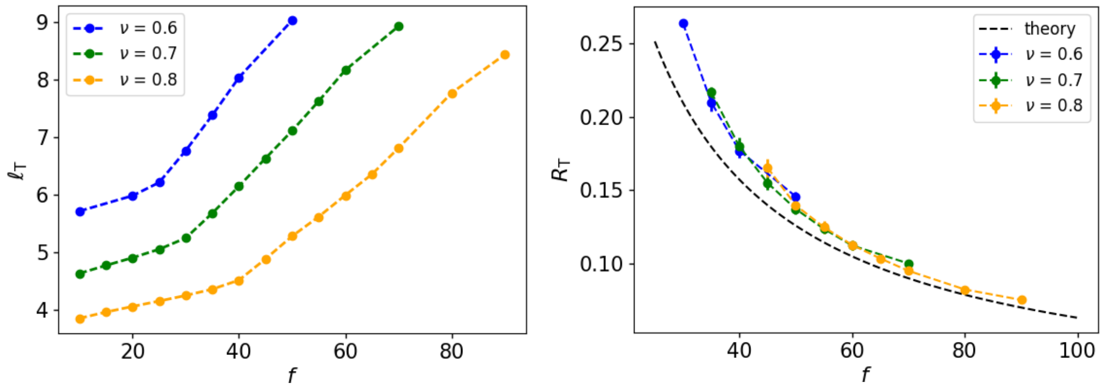

(a) total length (b) tube radius

Figure 5.5: Length ℓ_{T} and tube radius R_{T} of the shapes obtained from direct minimization for different forces f and different reduced volumes ν. The theory corresponds to Equation 4.2.

5.4.2 Vesicles with External Forces Applied

In the next step, the external force f was added, to see whether elongated and tubular structures can be observed. The minimizer performed in fact very well and an elongation of the structures for increasing forces could be observed, and for high enough forces even the formation of tubes. Some exemplary shapes for a reduced volume of $\nu = 0.8$ are shown in Figure 5.4 and a whole set of shapes obtained for different reduced volumes and forces can be found in Appendix A.2.

For high enough forces, tubes protruding from the vesicle are obtained, see Figures 5.4c and 5.4d. As observed in the simulations, lower forces lead to the elongation of the vesicle, but not yet to tubular structures. For forces just before the tube-forming threshold, the system is again in a 'lemon' shape, see Figure 5.4b.

One interesting observation is that the vesicle is not always in the center of the structure, i.e. the system is not entirely mirror symmetric. Instead the vesicle is closer to one end of the structure. Some slight shifts have also been observed in the simulations (c.f. Appendix A.1), but using direct minimization this effect seems to be more prominent. Clearly, the position of the vesicle in Figure 5.4g does not affect the total energy, as long as the tubes on both sides have the same radius, which is the case in this system. In Figure 5.4f it is possible that the structure is not in the absolute energy minimum since the radii of the tubes show a slight discrepancy, but also in this case the difference to the absolute energy minimum can be assumed to be very small.

5.4.3 Tube Length and Radius

The lengths of the structures and the radii of the tubes were determined to compare them to the simulation results. When increasing the external force, the tubes became more elongated and the radius decreased, as was the case in the simulations. The lengths and radii for different reduced volumes depending on the force can be found in Figure 5.5. As it was the case for the simulations, longer structures are obtained for lower reduced volumes and the radius is again also slightly above the theoretically predicted value. We explain the latter by slight deviations from the constraint on the surface area A_0. However, increasing k_{A} destabilized the system.

5.5 Comparison to Simulations

5.5.1 Note on Rescaled Units

The systems investigated are scale invariant, as mentioned previously (c.f. Section 3.4.1). In order to compare the simulation results to the results from direct minimization, the lengths and forces therefore need to be rescaled in the same manner. The rescaling used in this work is also commonly used in the literature and will allow us to conveniently compare our results to data reported in previous work.[146;147] The rescaled units that will be introduced in the following will be used whenever the corresponding quantity is marked with a superscript $'$.

The length is typically rescaled by R_S, which is the effective radius of the vesicle, i.e. the radius of a sphere with area A_0. In our case A_0 will refer to the area of the vesicle, which is fixed in the simulations and in the numerical solutions presented in this chapter. The rescaled unit of length is thus:

$$\sigma' = \frac{\sigma}{R_\mathrm{S}} \qquad \text{with} \qquad R_\mathrm{S} = \sqrt{\frac{A_0}{4\pi}} \tag{5.43}$$

The unit of energy is rescaled in the following way:

$$\epsilon' = \frac{\epsilon}{4\pi\kappa} \tag{5.44}$$

Thus the force f is rescaled as $f' = \frac{fR_\mathrm{S}}{4\pi\kappa}$. In the simulations $R_\mathrm{S} = 12.92$ and $\kappa = 20$ were used and for the direct minimization $R_\mathrm{S} = 1.077$ and $\kappa = 1$. For the rest of this section these rescaled units will be used for all lengths and forces.

5.5.2 Contour

First, the contours obtained from simulations and direct minimization were compared. Some sample contours can be found in Figure 5.6. The overall agreement is very good, however when looking in more detail there are some small deviations. Especially when it comes to the position of the vesicle, there are shifts, as seen in Figure 5.6c. The overall length and the radius, however, agree nicely.

5.5.3 Length and Radius

Finally, the lengths and tube radii were compared to the simulations and data from the literature. In Figure 5.7 the results from direct minimization are compared to the simulations, exemplary for $\nu = 0.7$. The agreement for the length is very good,

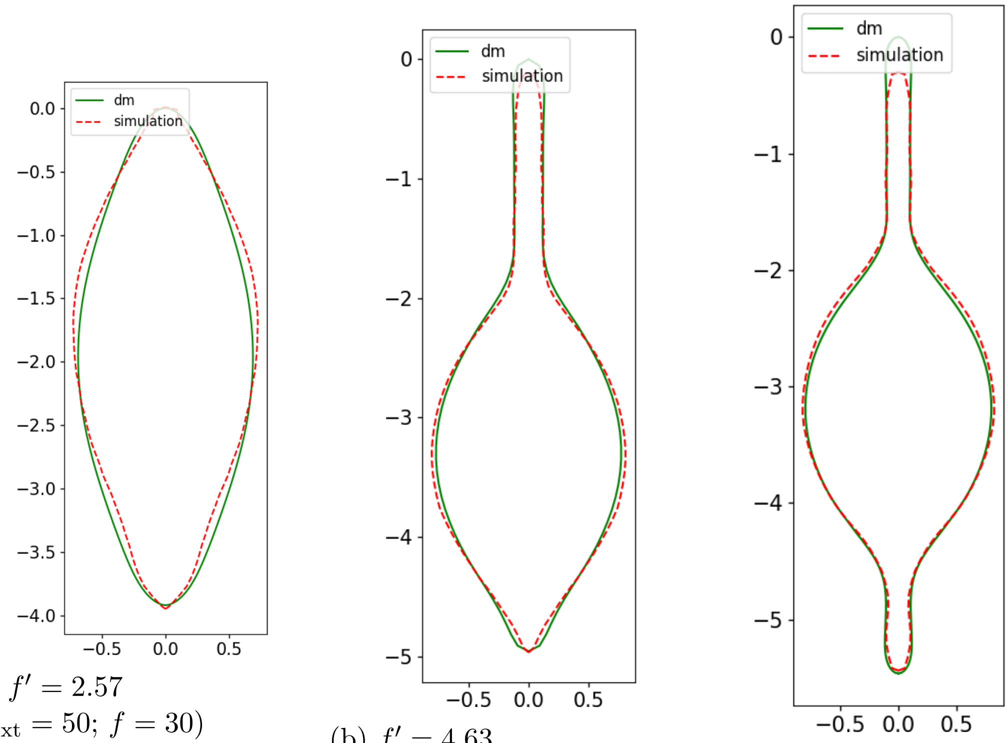

(a) $f' = 2.57$
($F_{\text{ext}} = 50$; $f = 30$)

(b) $f' = 4.63$
($F_{\text{ext}} = 90$; $f = 54$)

(c) $f' = 5.14$
($F_{\text{ext}} = 100$; $f = 60$)

Figure 5.6: Comparison of the contours obtained from direct minimization (dm) and simulations for different rescaled forces f' ($\nu = 0.8$). In parenthesis the values for the fores used in the simulations, F_{ext}, and direct minimization, f, are given.

whereas there are some slight deviations for the tube radius. These are, however, quite small given the length scales.

To further determine how our numerical model and our simulation model perform, they were compared to similar numerical optimization tools and analytical solutions found in the literature. In Ref. 153 the authors derived a theoretical approximate function for the tube length depending on the force f and the reduced volume ν:

$$l \simeq (1 - \nu^{2/3}) f \tag{5.45}$$

A comparison can be found in Figure 5.8, where the simulation results are shown in red, the results from direct minimization in green and the theoretical prediction in blue[c]. For $\nu = 0.6$ and $\nu = 0.7$ all three methods agree very well. For $\nu = 0.8$ the results from the simulations nicely match the theory, but there are some deviations for the direct minimization results for higher forces. The method might not be working reliably in this regime.

There is also a strong deviation from the theory for lower forces. This is, however,

---

[c] It should be noted that a constant offset (independent of ν) was added to the theory, to be able to compare it to our results. This offset is the diameter of the vesicle, which had to be added, because in the theory only the tubular part is considered, whereas we are looking at the length of the entire structure.

to be expected, because in the theory only a tube is considered, whereas in the simulations and the direct minimization method a vesicle with tubes is modeled. In this low force regime, the system does not have any tubes yet, but is only an elongated vesicle. As soon as the formation of tubes starts, the results agree with the theory very well.

In the literature, we could find two studies of a vesicle tube system, that were similar to our analysis, but used different methods. Both groups looked at axisymmetric vesicles with encapsulated rods, that formed tubular structures. In Ref. 146 the system was studied by solving dissipative dynamics for the Lagrangian nodes of a closed curve to find the energy minimum. Vesicles with an infinitely thin encapsulated rod, mimicking the cytoskeleton, were analyzed. This rod is introduced by an external force. The results are shown in orange (Shibuya et. al.) and have the same trend as our results from simulations, direct minimization and theory. For lower forces, they match our results very well, but for higher forces, they are significantly below our data and the theoretical prediction.

In the second study, see Ref. 147, the authors obtained their results by numerical optimization of the vesicle rod system. They were able to obtain different shapes, depending on rod diameter and type. Their results are shown in violet (Wu et. al.) and show the same trend as our results, but predict a slightly shorter length for high forces, which could be caused by the finite size of the rod in their system.

Overall, the agreement between the simulations and the results obtained from direct minimization is very good. The results are also consistent with data and theory reported in the literature.[146;147;153] This is another important indicator that the simulation model is performing well and can be reliably used for modeling vesicles and tubular structures. In the next chapter it will be employed to simulate the coalescence of tubes.

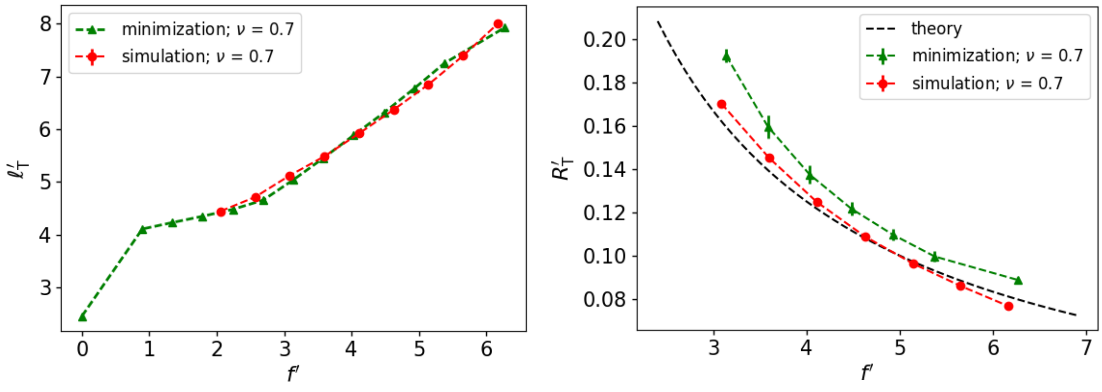

(a) total length (b) tube radius

Figure 5.7: Comparison of the lengths ℓ'_T and tube radii R'_T obtained from direct minimization and simulations ($\nu = 0.7$). The theory corresponds to Equation 4.2.

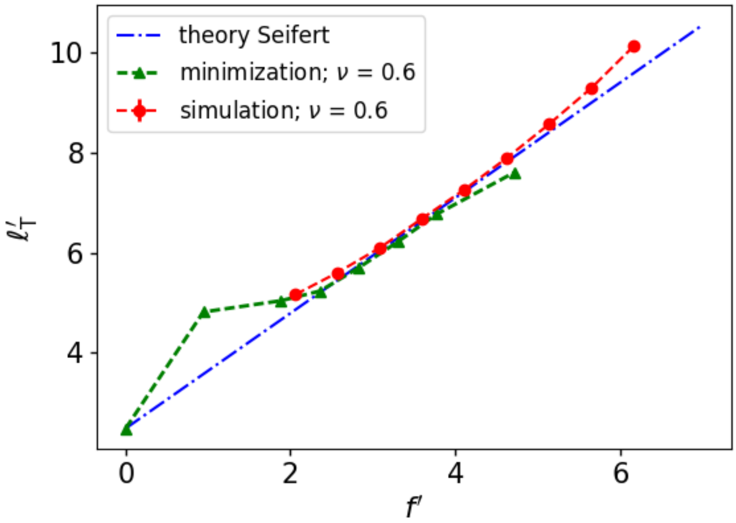

(a) $\nu = 0.6$

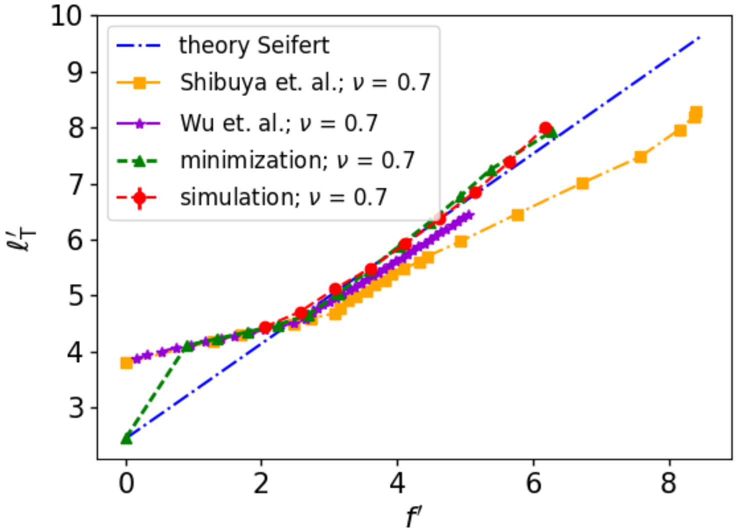

(b) $\nu = 0.7$

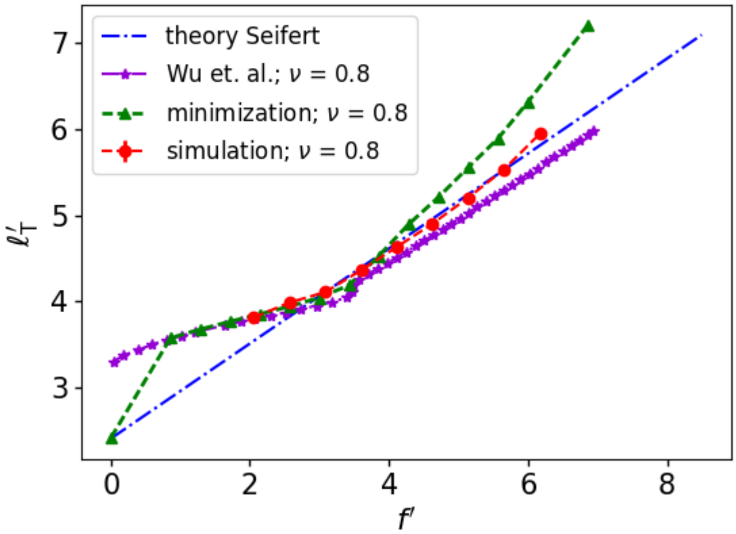

(c) $\nu = 0.8$

Figure 5.8: Comparison of the length ℓ'_T obtained from simulations (red) and direct minimization (green) to data from the literature for different reduced volumes ν. The theoretical prediction[153] given by Equation 5.45 is shown in blue. Results from two different optimization methods are shown in violet[147] and orange.[146]

6

Coalescence and Branching in Vesicle-Tube Systems

In this chapter we take a closer look at the coalescence and branching of tubular structures. Using the tubular vesicles simulated in Chapter 4 and a symmetric vesicle with four tubes, it was investigated at which angle between the tubes coalescence occurs. We compared these results to the theoretical predictions in Ref. 163. Afterwards, we studied the reverse process, i.e. branching of one tube into two.

6.1 Coalescence of Tubes

To investigate the coalescence of tubes, vesicles with two and four tubes respectively were simulated. By changing the angle α_T between two of the tubes, coalescence of the tubes could be observed at a certain angle $\alpha_\mathrm{T,c}$. Whether or not coalescence occurs was investigated for different applied external forces F_ext and reduced volumes ν of the system.

6.1.1 Symmetric Vesicles with Four Tubes

First, a symmetric configuration of a vesicle with four tubes was simulated. These configurations were generated from a closed spherical vesicle by applying external forces in four different directions. In the starting configuration the angle between the tubes was exactly $\alpha_\mathrm{T} = 90°$, as illustrated in Figure 6.1a. Then the angle between each pair of tubes was decreased. For small enough angles coalescence could be observed, as shown by the exemplary time evolution in Figure 6.1. The tubes start to merge in a zipper-like mechanism, until only one larger tube is remaining. This zipper-like merging mechanism has also been observed experimentally[10;11;163] and in simulations.[25;164]

The angle at which coalescence occurs was then determined for three different forces and is shown in Figure 6.2. If coalescence occurred, this is marked by a red circle, and if no coalescence occurred, this is marked by a blue square. One can observe

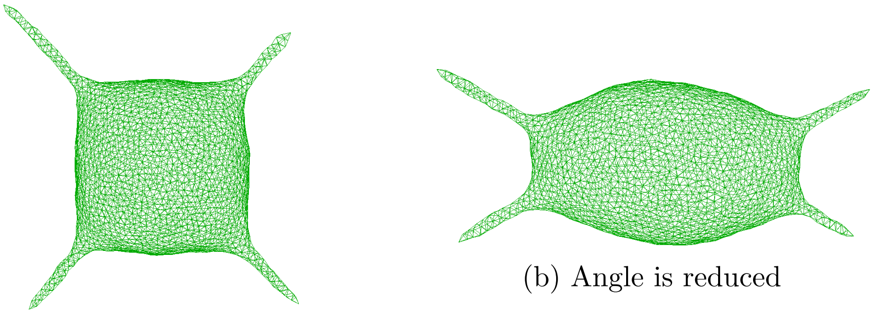

(a) Initial configuration

(b) Angle is reduced

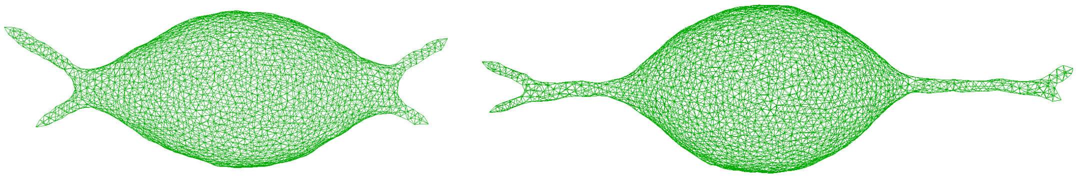

(c) Onset of coalescence

(d) Continuation of coalescence

Figure 6.1: Time evolution of a coalescence process.

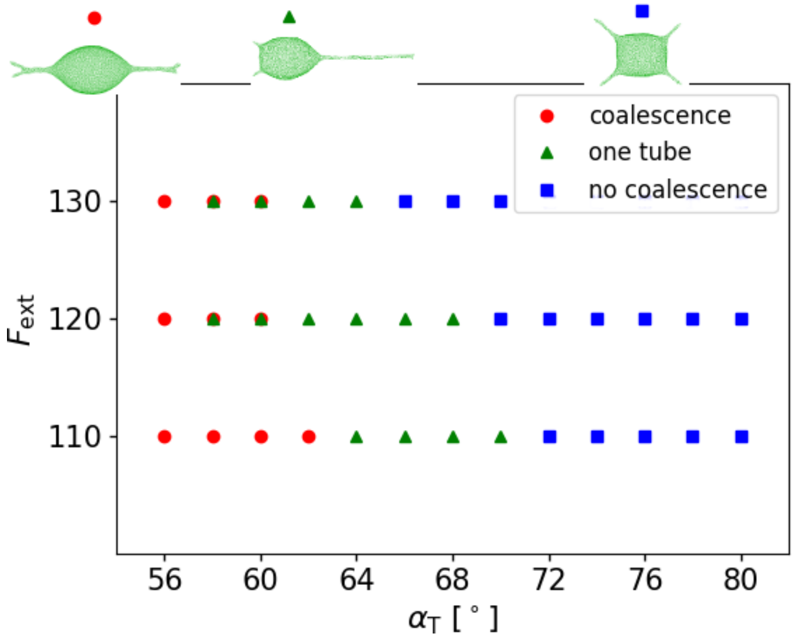

Figure 6.2: Angles α_{T} and forces F_{ext} for which coalescence was investigated ($\nu = 0.8$). If coalescence occurs, this is marked with a red circle, and no coalescence with a blue square. In the region between coalescence and no coalescence asymmetric configurations with only one tube were observed (green triangle).

a slight shift in the onset of the coalescence region for lower forces. This can be explained intuitively, because for lower forces the tubes are thicker, which means that they can touch each other and start to coalesce, where thinner tubes cannot.

In some cases an asymmetric final configuration with only one tube on one side was reached. This occurred for angles α_{T} in the intermediate region between coalescence and no coalescence and is marked by a green triangle. For each configuration 10 runs were performed, to see whether this is an occasionally occurring process or happens repeatedly. The red square for coalescence indicates that in the majority of the runs a symmetric end configuration with two tubes was reached, whereas the green triangle indicates that in the majority of cases an asymmetric end configuration with only one tube was reached. There was, however, no overlap with the no coalescence region, i.e. for all the runs performed either coalescence or no coalescence was observed. To compare these results to the theoretical predictions in Ref. 163, we had to slightly adapt our methodology and analyzed the coalescence of vesicles with two tubes.

6.1.2 Vesicles with Two Tubes

In this case the starting configuration was a symmetric tubular vesicle, where the angle between the tubes was exactly $\alpha_{\mathrm{T}} = 180°$, as shown in Figure 6.3a. This angle was then subsequently decreased. Before performing the simulations, however, it has to be taken into account that changing the angle causes an asymmetry in the forces, which means that the entire system would be dragged in one direction. To avoid this vesicle movement, two different approaches were employed.

In the first method a counter force was applied to all vertices, to balance the asymmetric pulling force on the tubes. The strength of this force depends on the angle and is the same for all vertices. This method corresponds to the vesicle being trapped in a viscous environment, which could for example be the cytoplasm or a dense network of filaments.

In the other approach, some of the vertices were always kept at a fixed position. In the simulations seven vertices and their neighbors were fixed, while the rest could move unperturbed. This second method corresponds to parts of the vesicle being anchored to other larger and heavier parts within the cell, which could also be filaments or even other cell organelles.[165]

The time evolution of an exemplary coalescence process of a vesicle with two tubes, that was stabilized using the first method, can be found in Figure 6.3. The process looks very similar to the one simulated for the four tube system, but the end-configuration is a vesicle with (only) one long tube. It could again be observed that if the angle between the tubes was reduced below a certain critical angle $\alpha_{\mathrm{T,c}}$,

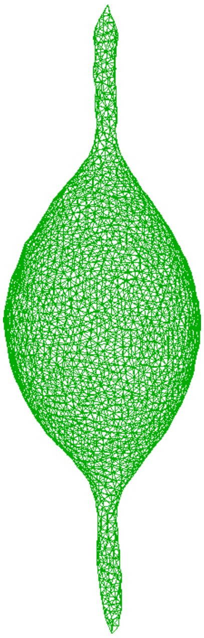

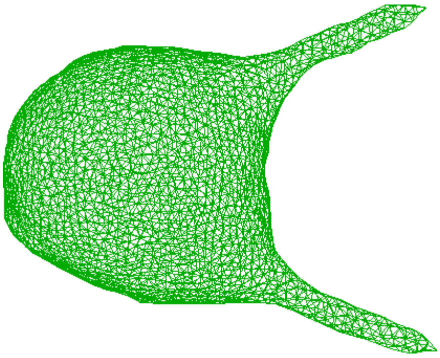

(b) Angle is reduced

(a) Initial configuration

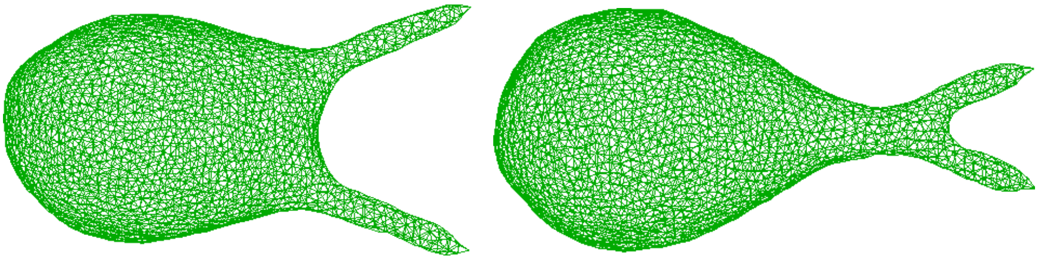

(c) Angle is reduced further

(d) Onset of coalescence

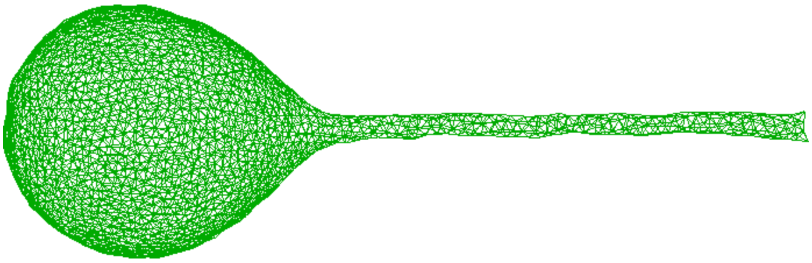

(e) Tubes completely merged

Figure 6.3: Time evolution of a coalescence process for a vesicle with two tubes.

coalescence occurred. Whether or not coalescence occurs was monitored for various angles for different forces F_{ext} and reduced volumes ν. The results obtained for the two different stabilization mechanisms can be found in Figure 6.4. As in the figure above, the red circles denote the occurrence of coalescence and the blue squares stand for no coalescence. Both systems show a slight shift in the onset of the coalescence region to larger angles for lower forces, as was observed in the four tube system and can be explained by the same mechanism.

One interesting observation is that the angle $\alpha_{\text{T,c}}$ for the onset of coalescence is different for the two systems. It is significantly higher for tubes stabilized using the second mechanism. At first this might seem counter intuitive, but when taking a closer look at the evolution of the vesicle, it could be observed that the vesicles that were only anchored to a few fixed points can become much more stretched than the ones stabilized by a homogeneous counter force. In this stretched elongated state the two tubes can get considerably closer than in the less strongly deformed system obtained by the first method, which means that coalescence can already occur at larger angles.

We were also able to compare our results for the onset of coalescence, $\alpha_{\text{T,c}}$, to an approximate analytical solution derived in Ref. 163:

$$\alpha_{\text{T,c}} \approx 4\sqrt{\frac{R_{\text{T}}}{R_{\text{v}}(1+\frac{R_{\text{v}}}{L_{\text{T}}})}} \tag{6.1}$$

where R_{T} is the radius and L_{T} the length of the tube, and R_{v} the radius of the vesicle. In our simulations R_{v} can be approximated by $R_{\text{v}} \approx R_{\text{S}} \approx 12.92$ and the length of the tube is given by $L_{\text{T}} \approx \frac{1}{2}\ell_T - R_{\text{S}}$. This derivation is based on geometrical relations for a system where $R_{\text{T}} \ll R_{\text{v}}$, and it is assumed that the tube only deforms the membrane slightly around the contact region.

Given these approximations, the simulation results agree very well with the approximate solution given by Equation 6.1, as shown in Figure 6.4a. Both methods show the same trend, but differ by $\Delta\alpha_{\text{T}} \approx 4^{\circ}$. The biggest factor causing this discrepancy is most likely the fact that the membrane is deformed relatively strongly around the tube-vesicle contact point, as can be seen e.g. in Figures 6.3b and 6.3c, while in the theory of Ref. 163 idealized vesicles are considered.

Finally, the coalescence angle $\alpha_{\text{T,c}}$ was investigated for different reduced volumes ν of the vesicle. This analysis was only performed for the first stabilization method, but we would expect similar results for the second one. The results are shown in Figure 6.5. One can observe a clear shift of the boundary to lower angles for lower reduced volumes, for which the tubes are longer and more pronounced.

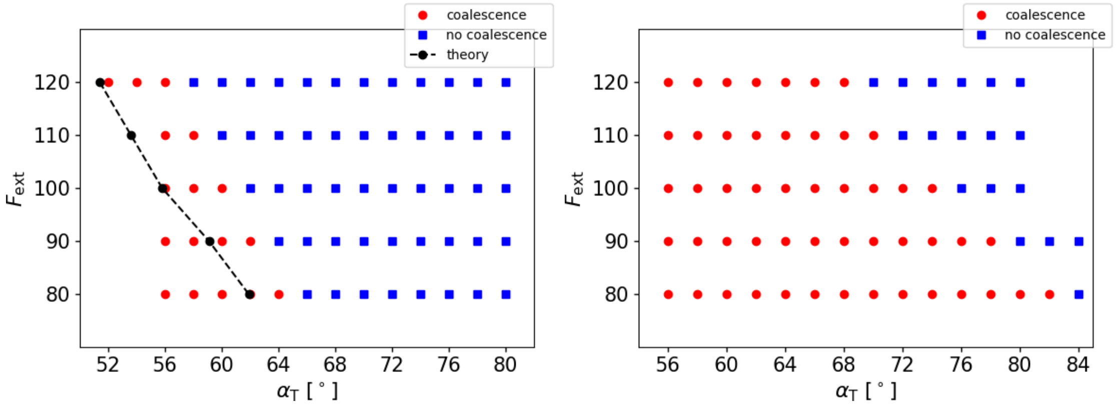

(a) Method 1: Counter force on all vertices. (b) Method 2: Some vertices are fixed.

Figure 6.4: Coalescence angle for the two tube system for $\nu = 0.8$. Two different methods were applied for keeping the system stationary. The theory corresponds to Equation 6.1.[163]

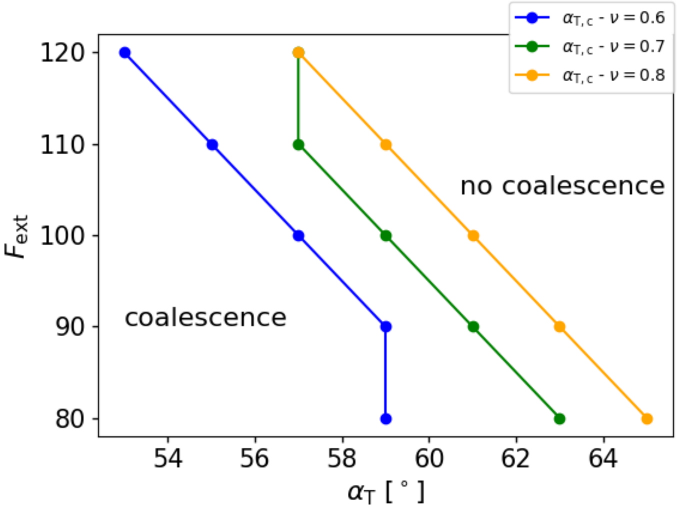

Figure 6.5: Critical angle $\alpha_{\mathrm{T,c}}$ for the onset of coalescence for different reduced volumes ν.

6.2 Branching of Tubes

After simulating the coalescence of tubes, the reverse process, i.e. the branching of one tube into two, was investigated. We looked at two different methods, as illustrated in Figure 6.6. In the first one, two external forces were applied at the end of the tube, pulling in different directions. In the other, an obstacle was placed in front of the tube and the tube pulled towards it.

It was, however, not possible to simulate branching of tubes with neither of these methods. In the first system, the tube simply elongated, slightly deforming the tip of the tube, as illustrated in Figure 6.7. This was the case for all forces and angles between the forces. In the second method, the tube simply moved around the obstacle, no matter whether the obstacle was pointlike or elongated.

With the methods described above, it was therefore not possible to split a tube protruding from a vesicle into two. This process might be hindered by the fixed reduced volume ν of the system. In experiments one typically has one large vesicle that serves as a lipid reservoir, allowing to manipulate tubular structures.[26;163;166–168] In the simulations however, the tube and the vesicle are strongly coupled. A second tube would require a large amount of extra surface area, which would have to be taken from the vesicular part, modifying the volume and thus be potentially hindered by our area and volume constraints that fix the area to volume ratio.

To investigate branched structures we therefore slightly adjusted the setup of the simulations. By removing the constraint on the volume and applying external forces, branched and tubular structures without a vesicular part can be investigated. This method will be explained in the next chapter.

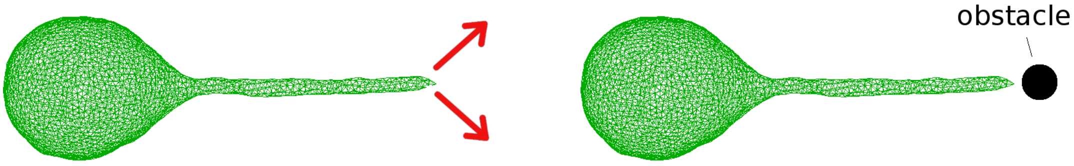

(a) Method 1: Two external forces (illustrated by the red arrows), pull at the end of a tube at a certain angle.

(b) Method 2: An obstacle is positioned in front of the tube and the vesicle pulled towards it.

Figure 6.6: Different approaches for simulating the branching of tubes.

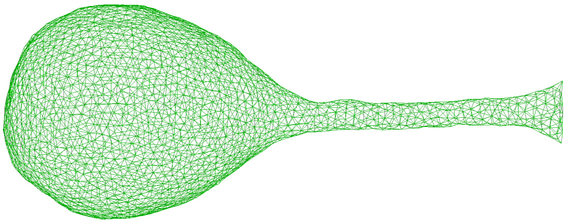

Figure 6.7: Intermediate configuration of the branching simulations. The tip of the tube slightly deforms, but no branch forms ($\nu = 0.8$).

7

Formation and Stability of Tubular and Branched Structures

Up until now, vesicles with tubular protrusions generated by external pulling forces have been analyzed. When removing these forces, the tubular structures immediately retract and a stable spherical, prolate or oblate vesicle forms, depending on the reduced volume (c.f. Fig. 4.1). In nature tubular membrane structures, however, often occur in the form of complex networks, without direct connection to vesicles (see e.g. Fig. 2.3a). It is now well established in the literature that tubular networks can be generated under the influence of curvature-inducing proteins (see e.g. the review paper in Ref. 68), or under the influence of an external force.[15] However, quantitative studies addressing the stability of tubular networks or their building blocks are very rare.

In 1991, Seifert *et al.* calculated the phase diagram for spontaneous-curvature models of lipid bilayers, based on the Helfrich model.[130;151] They found a manifold of interesting shapes that have also been discussed previously in this work. Similarly, in Ref. 169 the phase behaviour of fluid vesicles for various pressure differences was calculated. In particular, the authors found that the transition between the prolate structure and the stromatocyte is of second order, i.e. there is a finite energy barrier between these structures.

Similar energy barriers have then been observed in membrane tube formation[170] via experiments and computer simulations. This opens up the possibility to create a metastable tubular network using either curvature-inducing proteins or molecular motors. Metastability of tubes has also been analyzed in detail via computer simulations, using a similar triangulated membrane model as in this work.[113] The authors have explicitly shown that there is a free energy barrier between the tubular structures they created and the minimum-energy shapes, which are oblate and prolate structures for thick tubes and stromatocytes in the case of thin tubes. Under extreme conditions, these tubular structures can even become stable.[171] Keeping this in mind, it is not surprising that also tubular networks, such as the one observed in the endoplasmic reticulum, are highly dynamic structures,[172] in which new tubes are constantly created and existing tubes are merged or dissolved.

While the (meta)stability of tubes has been analyzed in detail, a network has a second fundamental building block, i.e. the junctions or branches in which several tubes merge. As already discussed in Chapter 2, it has been observed experimentally that these branches always consist of three connecting tubes, meeting at an angle of 120°.[10;11;13] Whenever this constraint is not fulfilled remodeling of the network occurs. A detailed analysis, similar to the one for cylindrical tubes, however, is missing.

In this chapter, we therefore analyze the formation, energetics and stability of the two building blocks of tubular networks discussed above: cylindrical tubes and branches. Our goal is the extension of the analysis of stability for simple tubular structures presented in Ref. 113 to branches. This will allow to draw important conclusions on the (meta)stability of tubular membrane networks.

7.1 Characterization of Tubular and Branched Structures

At first, we investigated the properties of branch and tubular structures, i.e. we compared their lengths and radii and then matched these results to theoretical predictions for a tubular structure. These results were complemented using the direct minimization method described in Chapter 5. Afterwards, we examined the energies of both systems, to determine which one is energetically more favorable. In the following the structure in Figure 7.1a will be referred to as a tubular structure or tube and the configuration in Figure 7.1b as a branched structure or branch.

To obtain these structures the simulation program and parameters described in Section 3.4 were used. The only difference compared to the previous simulations is that the volume constraint was set to zero. This allows the system to freely

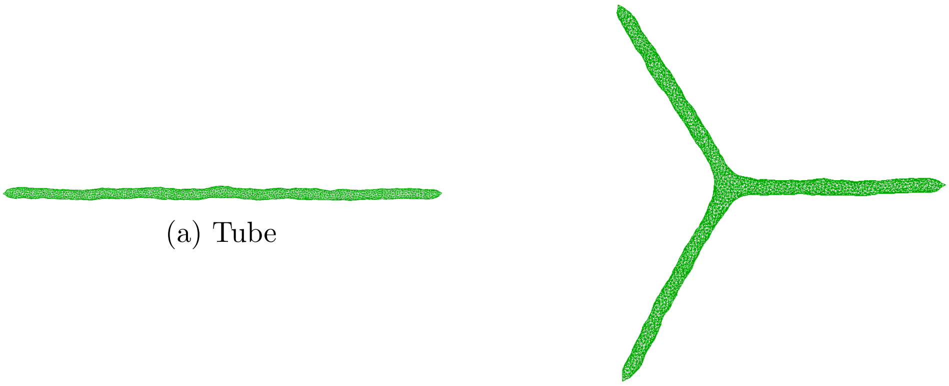

(a) Tube

(b) Branch

Figure 7.1: Tubular and branched structures, which will be investigated in the subsequent sections.

change its volume, while keeping the area constant. This situation corresponds to the creation of a tubular network, in which the tube or branch is effectively permeable. In nature one usually pulls the tubes out of large vesicles, which thus have a volume and an area reservoir. The tubular and branched structures were now obtained by simulating a spherical vesicle and applying an external force F_{ext} in two or three different directions, respectively. The reduced volume can now freely adjust; one therefore obtains pure tubular structures instead of tubular structures with a spherical part in the middle, as was the case in Chapter 4.

7.1.1 Length and Radius

First, we determined and analyzed some basic properties of the structures, namely the tube radius R_{T} and the overall length ℓ_{T}. The radius is again given by Equation 4.2 as:

$$R_{\text{T}} = \frac{2\pi\kappa}{F_{\text{ext}}} \tag{7.1}$$

and the length of the tubular structure is given by:

$$\ell_{\text{T}} = \frac{A}{2\pi R_{\text{T}}} \tag{7.2}$$

$$= \frac{AF_{\text{ext}}}{4\pi^2\kappa} \tag{7.3}$$

using simple geometric relations[a]. A is the total area of the structure, F_{ext} is the strength of the external pulling force and κ is the bending rigidity, a material constant.

The length and the radius of the tubular structure are simply given by the total length of the structure and the average radius in the tubular part (removing the caps at the two ends of the tube). For the branch structure, the overall length was defined as the total length of all the arms, where the length of one arm is given by the distance from the center of mass of the branch structure to the tip of the respective arm. The radius is then calculated by averaging the radii of the tubular parts in all three arms.

A comparison of the simulation results to the theoretically predicted values can be found in Figure 7.2. For each force 100 independent simulations were performed. Length and radius were averaged over the values obtained for the final stable configuration of each independent run. The simulation results for the tube and the branch are shown in green and blue respectively and the values from Equations 7.3 and 7.1 are shown in red.

---

[a] The tubular structure consists of a tube with two caps, which are (in good approximation) half spheres. The total length is therefore given by $\ell_{\text{T}} = L_{\text{tube}} + 2L_{\text{cap}} = L_{\text{tube}} + 2R_{\text{T}}$, and the total area by $A = A_{\text{tube}} + 2A_{\text{cap}} = 2\pi R_{\text{T}} L_{\text{tube}} + 4\pi R_{\text{T}}^2$. Using these two relations the total length can be expressed as $\ell_{\text{T}} = \frac{A}{2\pi R_{\text{T}}}$.

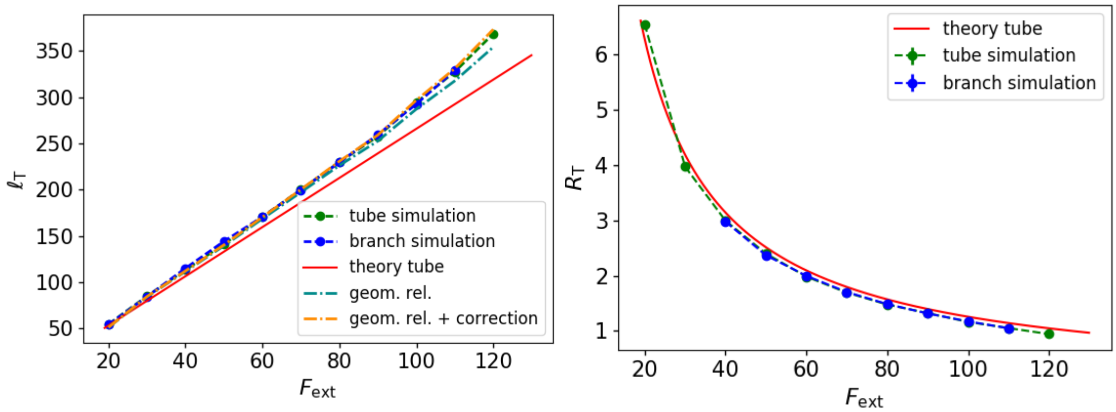

(a) Length

(b) Radius

Figure 7.2: Total length ℓ_{T} and tube radius R_{T} of the branch (blue) and tubular structures (green) for different external forces F_{ext}, compared to the analytical solutions for the tubular structure (red) given by Equations 7.3 and 7.1. The geometrical relation from Equation 7.2 is shown in light blue. The same relation with a correction, accounting for the discretization of the mesh, is depicted in orange.

The overall length ℓ_{T} and the radius R_{T} of the tube and branch structures match very well for all external forces F_{ext}. The radii of both structures also match the theory very well, they are only slightly below the predicted values. There is, however, a relatively large deviation, when looking at the total tube length for higher external forces. This can be explained by the slight deviation in the radius, when looking at Equation 7.2. The surface area A of our structures is very large compared to the tube radius R_{T}. A small deviation in the radius therefore leads to large discrepancies in the length.

To check our simulations for consistency, we therefore also calculated the length by using Equation 7.2 and the radius measured in the simulations. Using this geometric relation, one obtains the light blue dashed curve in Figure 7.2a, which is already very close to the determined values for the branch and tube structures.

Additionally, there is one further correction that can be made. For thin tubes, the resolution of the triangulated mesh used in the simulations might have problems to properly resolve the structures. When looking at the cross-section of a tube approximated by a triangular mesh, it is not a perfect circle, but rather a polygon. The number of sides of the polygon depends on the resolution of the mesh and the radius of the circle. Because the circumference of the polygon is smaller than the one of a circle, this leads to longer tubes, since the overall area is fixed. For a good resoltuion this effect is marginal, but it might become relevant for thin tubes. This deviation can be calculated and the derivation can be found in Appendix B.4. With this correction one obtains the dashed orange curve in Figure 7.2a, which matches the simulations very well. The effect is, however, very small and only slightly relevant for thin long tubes.

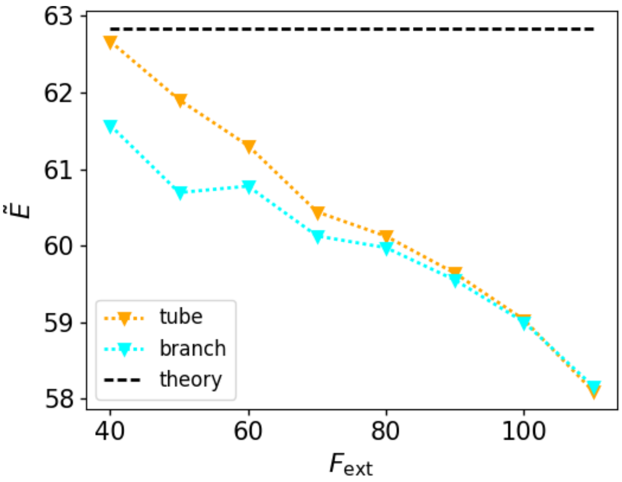

Figure 7.3: Modified energies $\tilde{E} = E_{\mathrm{cv,T}} R_{\mathrm{T}} / l_{\mathrm{T}}$ from simulations for different external forces, F_{ext}, and the theoretical value for a tube. The latter is given by $\tilde{E} = \pi\kappa$. The curvature energy of the tube was calculated using the method that will be presented in Section 7.2.

The finite resolution of the mesh is likely also the reason for the discrepancy between the theoretical value of the radius and the results from simulations. When investigating the energy of the system (see Section 7.2) one can show that the simulated tube has a lower curvature energy than predicted theoretically for the same radius ($E_{\mathrm{tube}} = \pi\kappa \frac{l_{\mathrm{T}}}{R_{\mathrm{T}}}$). This is illustrated in Figure 7.3, where a modified energy $\tilde{E} = E_{\mathrm{cv,T}} R_{\mathrm{T}} / l_{\mathrm{T}}$ is shown for different forces. One can clearly observe that the simulation values deviate from the theoretical tube value $\tilde{E}_{\mathrm{tube}} = \pi\kappa$. While these results indicate that there are small discretization effects in our simulations, we can similarly show that they are controllable and will only marginally affect our results.

The overall agreement between branch and tubular structures is very good. This is important, because they will be further compared and analyzed in later studies. The theory and the geometrical corrections respectively also match the simulations very well.

Lower Temperatures

To determine the effects of small undulations of the membrane surface due to thermal fluctuations, the analysis described above was also performed at a lower temperature T. The end-configurations obtained by the simulations above were cooled down continuously to a temperature of $T = 10^{-6}$. A comparison between the lengths ℓ_{T} and radii R_{T} for both temperatures can be found in Figure 7.4.

The results for $T = 1$ are again shown in green and blue for the tube and branch structures respectively and the results for $T = 10^{-6}$ are shown in orange for the tube and in light blue for the branch. All four curves almost overlap for both the

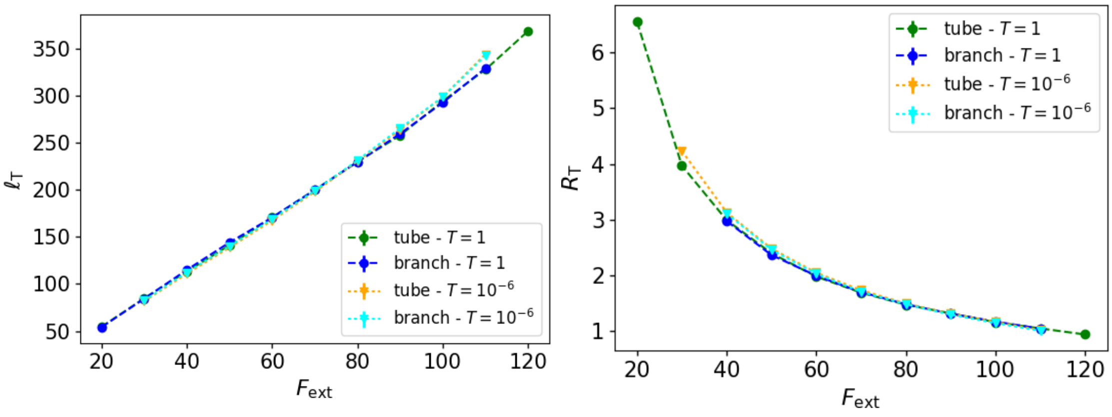

(a) Length

(b) Radius

Figure 7.4: Comparison of the lengths ℓ_{T} and the tube radii R_{T} of the tube and branch structures for different external forces F_{ext} at two different temperatures T.

length ℓ_{T} and the tube radius R_{T}. The temperature therefore does not seem to affect the overall shape of the systems.

7.1.2 Comparison to Results from Direct Minimization

Tubular structures, as shown in Figure 7.1a, can also be calculated using the direct minimization method derived in Section 5.3. The method was applied as described above, but no constraint on the volume was set. As in the simulations, this allows the reduced volume to adjust freely. A comparison of the contours obtained by the different methods, as well as the tube lengths ℓ'_{T} and radii R'_{T} can be found in Figures 7.5 and 7.6 respectively. Note that for the comparison the rescaled units presented in Section 5.5.1 were used. This is again denoted by a superscript $'$.

The shapes were compared and are exemplarily shown for three different external forces f'. For all forces the agreement between the contours obtained from simulations and from direct minimization is relatively good. There are some small deviations in the total length, but the overall shape matches very well. When directly comparing the lengths ℓ'_{T} and radii R'_{T} one also observes a very good agreement. The radius in the simulations is slightly below the one obtained from direct minimization, but the deviations are relatively small.

7.1.3 Curvature Energy

Finally, we compared the curvature energies, U_{cv}, of the two structures. Since the tube radius and the overall length are roughly the same, the only difference between the two structures is the neck structure and an additional cap in the branch structure. The caps are the end-points of the tube, (roughly) resembling a

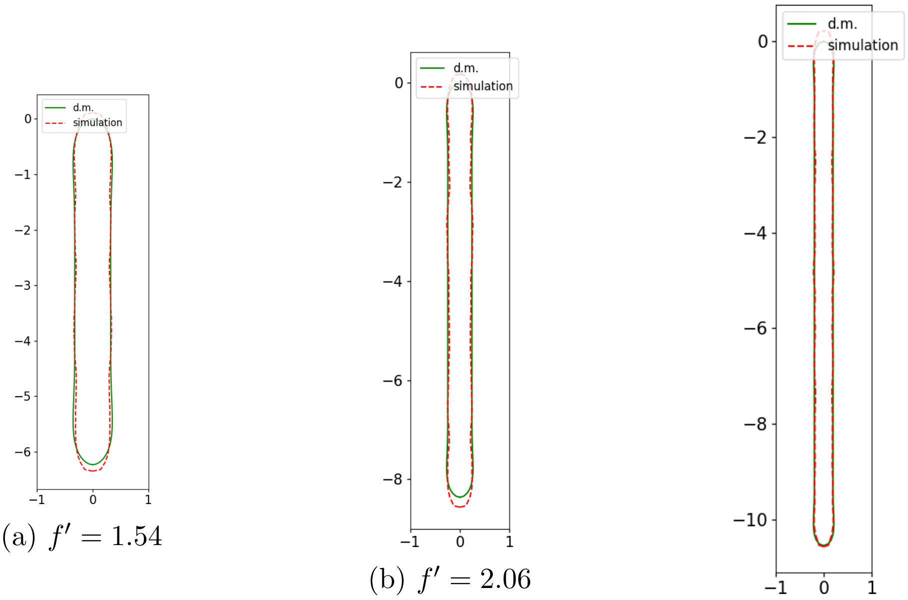

(a) $f' = 1.54$

(b) $f' = 2.06$

(c) $f' = 2.57$

Figure 7.5: Comparison of the contours obtained from simulations (red) and direct minimization (d.m.) (green) of the tubular structure, for different external forces f'.

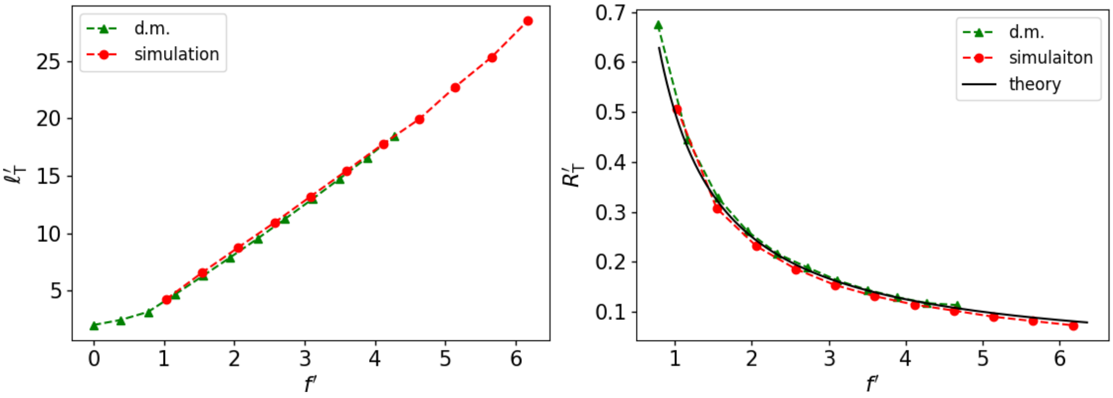

(a) Length

(b) Radius

Figure 7.6: Lengths ℓ'_{T} and radii R'_{T} of the tubular structures for different external forces f', as determined by simulations, shown in red, and results from direct minimization (d.m.), shown in green. The theory corresponds to Equation 7.1.

hemisphere, and the neck is the part in the branch structure, where the three tubes meet. This is illustrated in Figure 7.7.

A comparison of the curvature energy, U_{cv}, for different external forces, F_{ext}, is shown in Figure 7.8. The energies of both structures are found to be very similar. Additionally, we calculated the curvature energies for the simulations performed at $T = 10^{-6}$, to determine the effects due to thermal fluctuations.

For $T = 10^{-6}$ the curvature energies for both the branch and the tube structure are below the energies measured at $T = 1$. This is not surprising, because small undulations of the membrane surface, caused by the finite temperature T in the system, contribute significantly to the curvature energy. At low temperatures, this is not the case, because the membrane surface is much smoother.

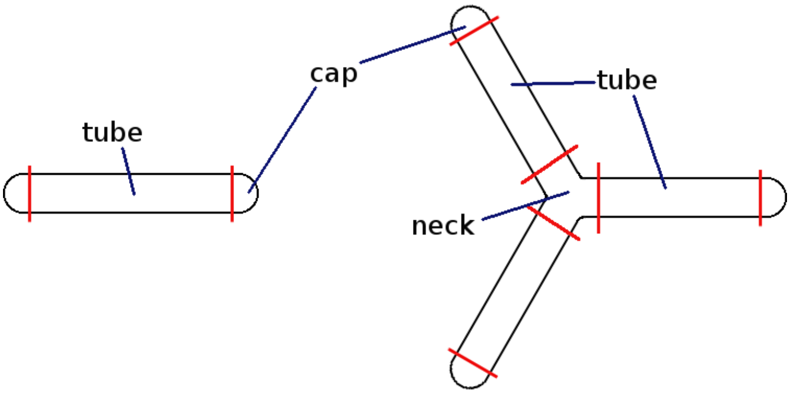

Figure 7.7: Sketch of a tubular and a branched structure. Both can be compartmentalized into a tube part and caps, and (for the branched structure) a neck part.

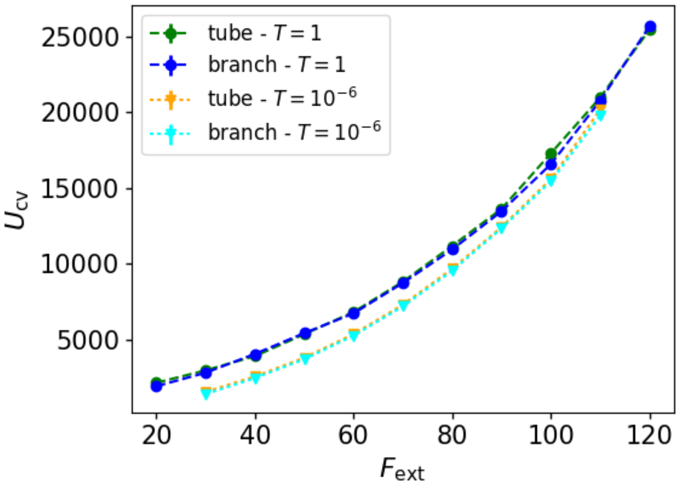

Figure 7.8: Curvature energy, U_{cv}, for the tube (green; orange for $T = 10^{-6}$) and the branch (blue; light blue for $T = 10^{-6}$) for different forces F_{ext} at two different temperatures T. The energies of both systems are very similar for both temperatures, but the curvature energy is reduced at $T = 10^{-6}$.

7.2 Curvature Energy of the Tube and Branch Building Blocks

It is interesting to see that the energies of both systems are very similar, even if their structure is different. To investigate this further, we split up the systems into their different components (tube, neck and cap) and determined their individual curvature energies. We are particularly interested in the neck energy, because the neck is the component which distinguishes a branch from a simple tube.

The tubular structure can be split into a tube part and two caps, the branch structure into a tube part, three caps and a neck part, as illustrated in Figure 7.7. The analysis was carried out at low temperatures, i.e. $T = 10^{-6}$, to eliminate additional contributions to the curvature energy due to thermal fluctuations.

7.2.1 Calculation of the Energy of the Components

To determine the energy of the neck and cap structure, one first has to take a look at the curvature energy, E_{cv}, of the tube and branch structure. These curvature energies are given by those of the different components:

$$E_{\text{cv,tube}} = E_{\text{t}} + 2E_{\text{cap}} \tag{7.4}$$

$$E_{\text{cv,branch}} = E_{\text{t}} + 3E_{\text{cap}} + E_{\text{neck}} \tag{7.5}$$

E_{t} is the energy of the tubular part, E_{cap} the energy of a cap and E_{neck} the energy of the neck structure.

The curvature energies of the components could in theory be determined by simulations at low temperatures, when defining regions for the cap and the neck structure. It is, however, difficult to determine where exactly the the neck part and the caps start, which would make this analysis imprecise and dependent on these cutoff conditions.

We therefore decided to compare the energy of a component (cap or neck) to the energy of a corresponding tubular structure. Hence, two new quantities are introduced:

i) A new length l^{mod}, which refers to the length a component would have if it were a simple tube with open ends. This is illustrated in Figure 7.9 for the cap and is done accordingly for the neck. This quantity can be easily calculated from the area A of the component and the radius of the tube R_{T}, which can be extracted in the simulations from the tubular part of the structures:

$$l^{\text{mod}} = \frac{A}{2\pi R_{\text{T}}} \tag{7.6}$$

ii) The energy per tube length e of the tubular part:

$$e = \frac{E_{\text{t}}}{l_{\text{t}}} \tag{7.7}$$

where l_{t} is the length of the tubular part illustrated in Figure 7.7 and E_{t} its energy. This quantity can be easily calculated for the tubular structure. For the branched structure, it is given by the average over the three connecting tubes: $e = \frac{1}{3}\sum_{i=1}^{3}\frac{E_{\text{t},i}}{l_{\text{t},i}}$.

With these two quantities, it is now possible to calculate the energy difference between having a cap at the end of the tube, compared to this end region being tubular:

$$\begin{aligned} \Delta E_{\text{cap}} &= E_{\text{cap}} - l^{\text{mod}} e & (7.8) \\ &= E_{\text{cap}} - \frac{A_{\text{cap}}}{2\pi R_{\text{T}}} e & (7.9) \end{aligned}$$

The same calculation can be performed for the neck region:

$$\begin{aligned} \Delta E_{\text{neck}} &= E_{\text{neck}} - l^{\text{mod}} e & (7.10) \\ &= E_{\text{neck}} - \frac{A_{\text{neck}}}{2\pi R_{\text{T}}} e & (7.11) \end{aligned}$$

Using these definitions, it is, in principle, irrelevant how the neck and cap regions were defined, i.e. where the cutoffs were set, because any (potential) additional tubular part will simply be subtracted later. The only requirement for the cutoff is that it is large enough to include all parts of the component that are different from the tubular part. Using this technique, one can therefore determine the pure energy differences of the cap and neck structures. The cutoff r_{cut} can be determined empirically, by increasing it stepwise and analyzing the convergence of ΔE with increasing r_{cut}. This minimum cutoff thus also gives a good estimator of the size of the individual components. In our simulations we found a minimum cutoff $r_{\text{cut}} > 7$ for the caps and $r_{\text{cut}} > 18$ for the neck structures.

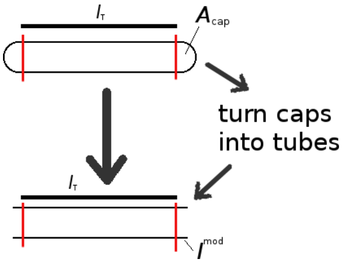

Figure 7.9: Introduction of a new length l^{mod} that characterizes the components. The modified length is given by Equation 7.6.

7.2.2 Cap and Neck Energies

The energy differences obtained for the cap and neck structures using Equations 7.8 and 7.10 are shown in Figure 7.11. The energy per tube length of the tubular part is shown in Figure 7.10.

The energy per tube length e increases linearly for increasing forces F_{ext}. This is to be expected, because the tubes are thinner for higher forces and therefore more strongly curved, which means they have a higher curvature energy. The energy per tube length is almost the same in the tubular and branched structure, because they have a very similar tube radius, as shown in Figure 7.4.

The cap energies ΔE_{cap}, shown in Figure 7.11a for the tube and branch structure, are also very similar. This is the case, because the cap structure is the same in the tube and branch system, which therefore confirms the definitions and calculations discussed above. The slight deviation is due to a small difference in the tube radius. In an ideal system, one would assume the cap to be a half-sphere. The cap energy difference would therefore be given by $\Delta E_{\text{cap}} = 4\pi\kappa - \pi\kappa\frac{l_{\text{T}}}{R_{\text{T}}}$. From our definition of the modified tube length $l_{\text{T}} = \frac{A_{\text{HS}}}{2\pi R_{\text{T}}}$, with $A_{\text{HS}} = 2\pi R_{\text{T}}^2$, one can thus immediately conclude that $\Delta E_{\text{cap}} = 3\pi\kappa \approx 188$. Due to the external pulling force in the simulations, however, which produces more pointy caps, we find that the cap energy is slightly larger than the theoretical expectation. Interestingly, the energy in the simulations appears to converge against the theoretical value for larger forces. This is likely due to the small radius of the structure, which does not allow for very pointy caps any more.

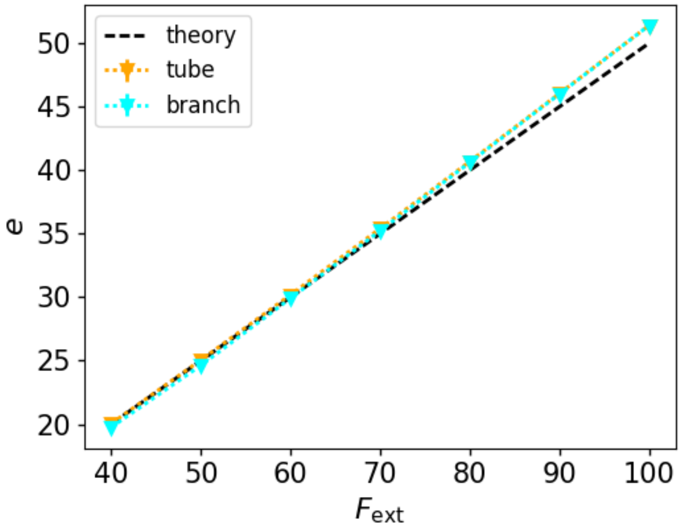

Figure 7.10: Energy per tube length e of the tubular part of the tube (orange) and branch structures (light blue) for different external forces F_{ext}. The black dashed line (theory) can be derived from Equation 7.7 and the theoretical tube radius, c.f. Equation 4.2, and is given by $e = \frac{F_{\text{ext}}}{2}$.

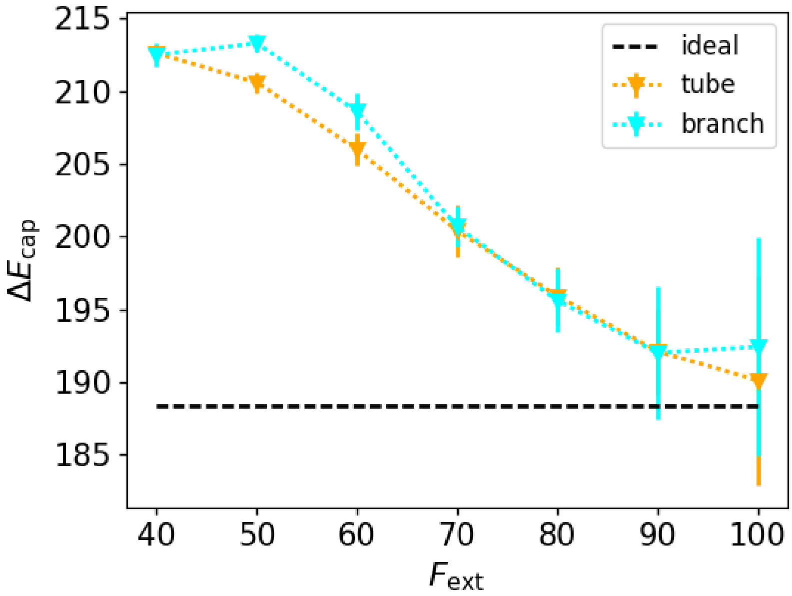

(a) Cap energy ΔE_{cap}. The black dashed line (ideal) corresponds to the theoretical value for the cap being a perfect half-sphere.

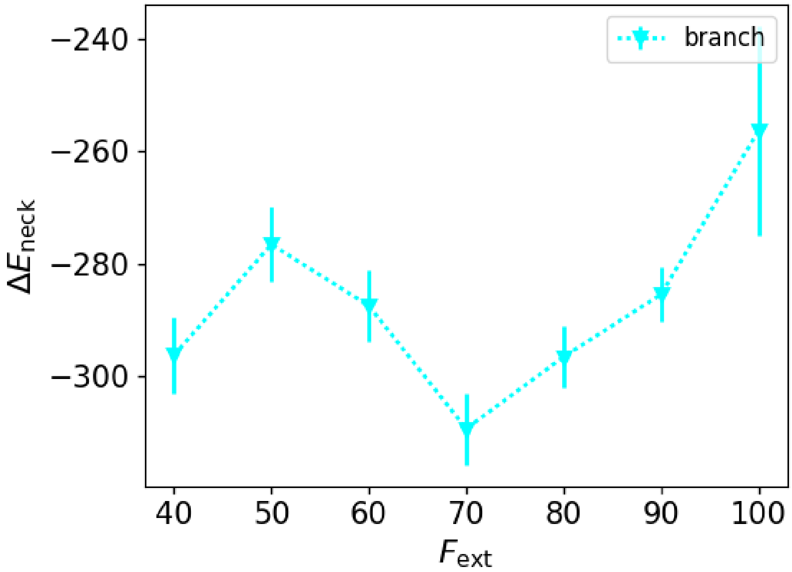

(b) Neck energy ΔE_{neck}.

Figure 7.11: Energies of cap, ΔE_{cap}, or neck structures, ΔE_{neck}, relative to corresponding tubular structures, according to Equations 7.8 and 7.10. The values were calculated for different external forces F_{ext} and hence tubes of different radii.

The energy difference of the neck, ΔE_{neck}, is shown in Figure 7.11b. The most important observation is that the neck energy is negative, and similarly the quantity $\Delta E = \Delta E_{\text{neck}} + \Delta E_{\text{cap}}$, which corresponds to the energy difference between the tubular and the branched structure, since the tube radii of the two structures are very similar. One can thus conclude that the branch structure is energetically more favorable due to its neck component. The neck energy itself systematically increases for increasing forces, mainly because it becomes smaller and thinner and thus more curved. The non-monotonicity that can be observed at $F_{\text{ext}} = 50 - 60$ appears to be relatively sensitive to the choice of the cutoff r_{cut}.

With this analysis, we can clearly show that the formation of a neck structure and a cap structure, i.e. the creation of a branch, is energetically favorable. Nevertheless, simulations indicated that this transition is connected to a significant energy barrier, as will be discussed in the next sections.

7.3 Transition between Branch and Tubular Structures

In the previous sections, it could be shown that branch and tubular structures have very similar properties. They have the same tube radii and lengths and also roughly the same curvature energy. In the following the transition between these two structures and the energy profile for the transition is investigated. These simulations are now again performed at $T = 1$.

First, the two simple transitions from a sphere to a tube and from a sphere to a branch are considered. Then the more interesting and complex transformations from a branch to a tubular structure and vice versa are investigated. All transitions are smooth, except for the one from a tube to a branch, which will therefore be investigated in more detail.

The curvature energy is given by Equation 3.8, as described in the previous chapters. In addition to this, the contribution from the external pulling force needs to be determined, which is given by the work performed by the external force to displace the outermost vertices, i.e. the ones to which the force is applied to:

$$W_i = \vec{F}_{\mathrm{ext},i} \Delta \vec{s}_i \tag{7.12}$$

where $\vec{F}_{\mathrm{ext},i}$ is the external force acting on vertex i and $\Delta\vec{s}_i$ the corresponding displacement of this vertex. The total work is given by the sum over all vertices j the force is applied to: $W = \sum_j W_j$.

7.3.1 Sphere to Tube/Branch

Starting form a spherical vesicle, opposing forces on two opposite beads were applied to obtain a tubular structure. The time evolution of the curvature energy, E_{cv}, due to this shape change, and the work due to the pulling, W, are shown in Figure 7.12a. The curvature energy (red) increases, but the overall energy of the system (green), i.e. the energy difference between the curvature energy and the work performed by the external force (blue), decreases and reaches a minimum.

For reference the total inner energy of the system is shown in black. This term also includes the energies from the bond, repulsive and area potentials, c.f. Equation 3.14. These contributions are, however, very small and roughly constant throughout the shape transformation. This shows that the important and relevant quantity is the curvature energy. In the further analysis, the curvature energy will therefore be considered, when comparing it to the work due to the external force W.

It is actually an interesting observation that the transition from the sphere to a tubular structure is very smooth, without any indicator for an energy barrier.

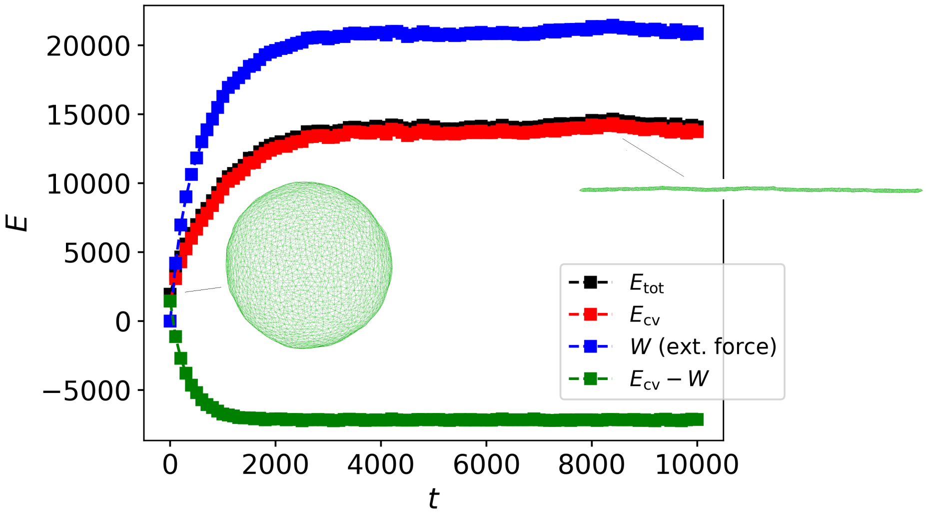

(a) Transition: Sphere - Tube

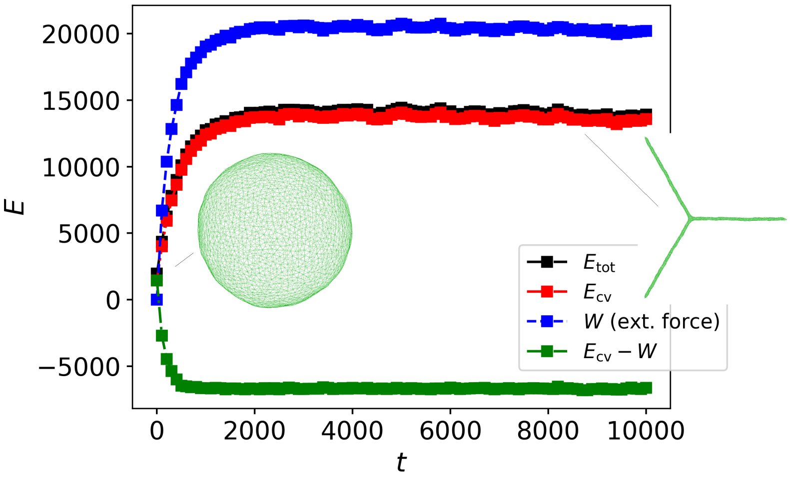

(b) Transition: Sphere - Branch

Figure 7.12: Time evolution of the curvature energy, E_{cv}, (red) due to the shape change from a spherical to a tubular/branched structure. The external force was $F_{\mathrm{ext}} = 90$ and the energy contribution due to the force, W, is shown in blue. The difference is given by the green curve as $E_{\mathrm{cv}} - W$.

Experimental results, in which a tube is pulled from a vesicle using optical tweezers at constant *speed*, clearly show the existence of a force maximum which has to be overcome to create the tube.[163;173] This is usually an indicator for an energy barrier. This discrepancy between experiments and simulations could either be connected to different constraints (Ref. 163 had a lipid reservoir, Ref. 173 was performed at $\nu = const.$) or to large pulling velocities in experiments. In future studies it would be interesting to also perform simulations with constant pulling velocities (instead of constant pulling forces) and investigate this observation in more detail.

For the transition from a sphere to a branch, the time evolution of the energy looks very similar, as shown in Figure 7.12b. The energy difference between the curvature energy, E_{cv}, and the work due to the displacement, W, also decreases and reaches a minimum. For different forces the energy profile looks very similar. The absolute values of the energies are, of course, different, but the overall shape and behavior is the same.

7.3.2 Branch to Tube

As a next step, the transition from a branch to a tubular structure is examined. Starting from a branch-like structure, the external force on one of the branches is released, while the other two forces pull in opposing directions. This leads to the retraction and finally absorption of the third branch, as illustrated in Figure 7.14. The final configuration is a tubular structure.

This transition occurs smoothly, which is reflected in the energy profile shown in Figure 7.13a. Releasing one of the branches leads to a brief decrease in the curvature energy, because the released branch and the newly formed tube are thicker and hence less strongly curved than the original branch structure. As soon as the tube then starts to elongate and becomes thinner, the curvature energy increases again and roughly reaches the value it initially had. The energy difference, $E_{\mathrm{cv}} - W$, is monotonically decreasing, showing that a new final configuration, minimizing the overall energy, is reached. Similar structures and profiles where obtained for other forces.

In Figure 7.13b the time evolution of the curvature for the transition is shown. This curvature is measured using the renormalized area difference Δa, c.f. Equation 3.23.

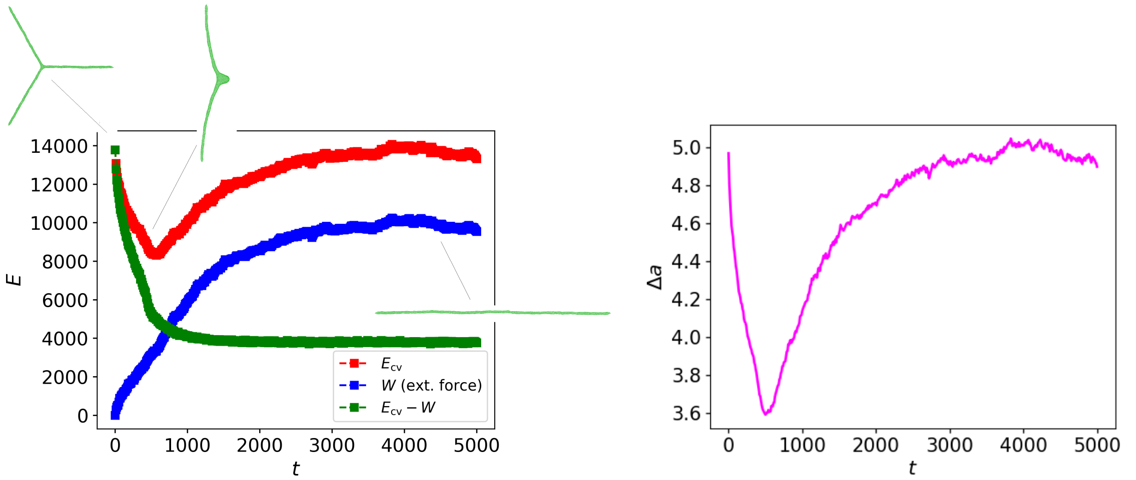

(a) Time evolution of the curvature energy, E_{cv}, (red) due to the shape change from a branch to a tubular structure. The external force was $F_{\mathrm{ext}} = 90$ and the energy contribution due to the force, W, is shown in blue. The difference is given by the green curve as $E_{\mathrm{cv}} - W$.

(b) Time evolution of the curvature of the system, measured using the renormalized area difference, Δa, introduced in Section 3.4.1.

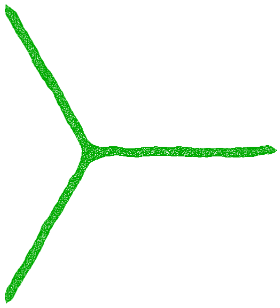

(a) Initial branch structure ($t = 0$).

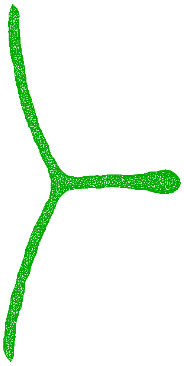

(b) Intermediate structure; right tube starts to retract ($t = 200$).

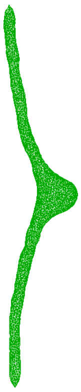

(c) Intermediate structure; right tube is almost absorbed ($t = 440$).

(d) Final tubular structure ($t = 2000$).

Figure 7.14: Snapshots of the conformational change from a branch to a tubular structure.

The time evolution of the curvature has basically the same shape as the curvature energy, E_{cv}, shown in Figure 7.13a. The dip in the curvature is an indicator, that this transition could be suppressed by a constraint on the overall curvature of the system, which will be further discussed and investigated in Section 7.4.4.

7.3.3 Tube to Branch

The above described transformation from a branch to a tubular structure occurred smoothly. However, when looking at the transition the other way around it is not as direct. When attempting to pull out a third tube from a tubular structure, using the same external force as needed to stabilize the original system, the tube deforms, but never reaches a branched structure. The system rather gets stuck in a wide v-shape configuration, as shown in Figure 7.15.

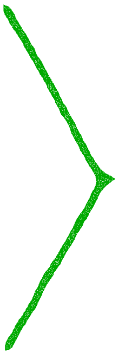

Figure 7.15: Final configuration for the transition from a tube to a branch structure. The system gets stuck in this v-shaped configuration, when using the same external force as needed to stabilize the original system.

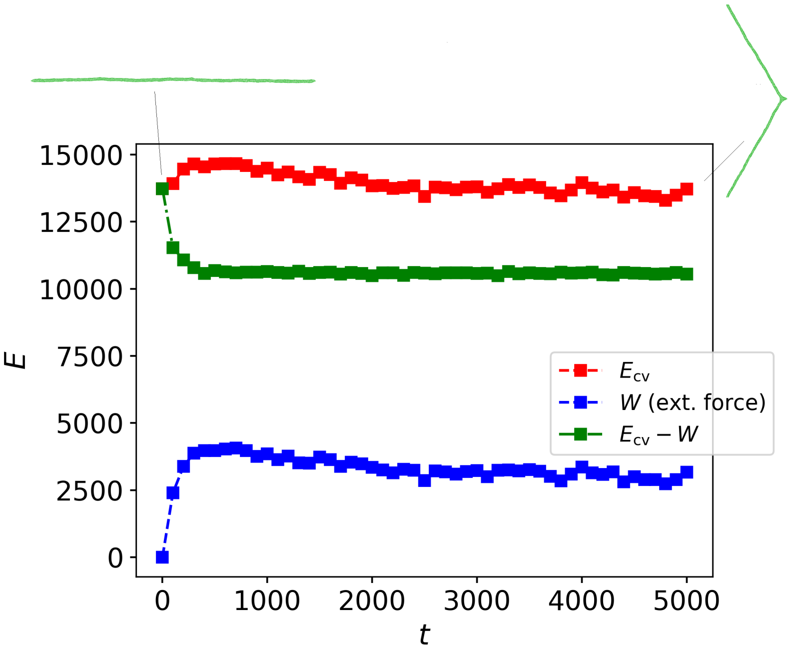

Figure 7.16: Time evolution of the curvature energy, E_{cv}, (red) due to the attempted shape change from a tube to a branched structure. The external force was $F_{\text{ext}} = 90$ and the energy contribution due to the force, W, is shown in blue. The energy difference is given by the green curve as $E_{\text{cv}} - W$.
The tube deforms, but the branch structure is not reached.

This is also confirmed when looking at the time evolution of the energy as shown in Figure 7.16. Deforming the tube leads to an initial increase in the curvature energy, but it then settles again on the original value. There seems to be some kind of energy barrier that has to be overcome to pull out the third tube, and the force needed to simply stabilize the branch does not seem to be sufficient to overcome this energy barrier. This is a very important observation, that might have interesting implications for the branching of tubular networks. The question is how much additional force has to be invested to overcome this initial energy barrier.

To determine the strength of the force necessary to pull out a tube, F_{ext} was increased stepwise by increments of $\Delta F_{\text{ext}} = 1$, to see for which forces the third tube starts to form. Tubes created with external forces between $F_{\text{ext}} = 60 - 100$ were investigated. The third force, pulling out the additional tube was then steadily increased. For all forces, the third tube formed when the third force was increased by $\Delta F_{\text{ext}} \approx 3 - 4$. This is approximately $4 - 6\,\%$ higher than the force needed for stabilization. We can therefore identify the existence of an energy barrier, but it appears that only a slight increase of the pulling force is required to overcome this barrier.

7.4 Stability of Tubular and Branched Structures

In this section the stability of the tubular and branched structures is investigated. First, the angles between the tubes of a branch were varied. Then, the stability of the tubular and branched structure was tested by releasing the external forces but keeping the reduced volume ν fixed. Finally, we also studied whether their stability can be improved by setting a constraint on the overall curvature of the system.

7.4.1 Varying the Angle between the Arms - Fixed Direction

It was analyzed how a branched structure is transformed if the angles between the three arms of the branch are varied. The stable branches simulated above had a perfect 120° angle between all three branches. By varying this angle, the following three systems, illustrated in Figure 7.17, were investigated:

(i) The angle of one of the tubes was slightly varied by $\Delta\varphi$.

(ii) The angle between two of the tubes was varied, so that the new angle between these two tubes is α and the other two angles are $180° - \alpha/2$.

(iii) Starting from a branched structure, the direction of the pulling force is changed, so that one angle is now 180° and the other two 90°.

It should be noted that the forces in these systems do not completely balance each other any more, which means there is a small excess force in one direction. The respective systems therefore slightly shift towards the direction of this excess force, this, however, does not affect the outcome with respect to coalescence.

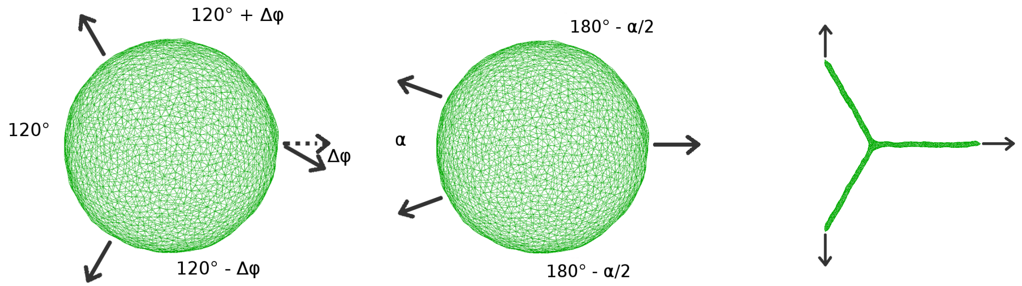

(a) System (i) (b) System (ii) (c) System (iii)

Figure 7.17: Sketch of the different systems used to investigate the stability of branched structures.

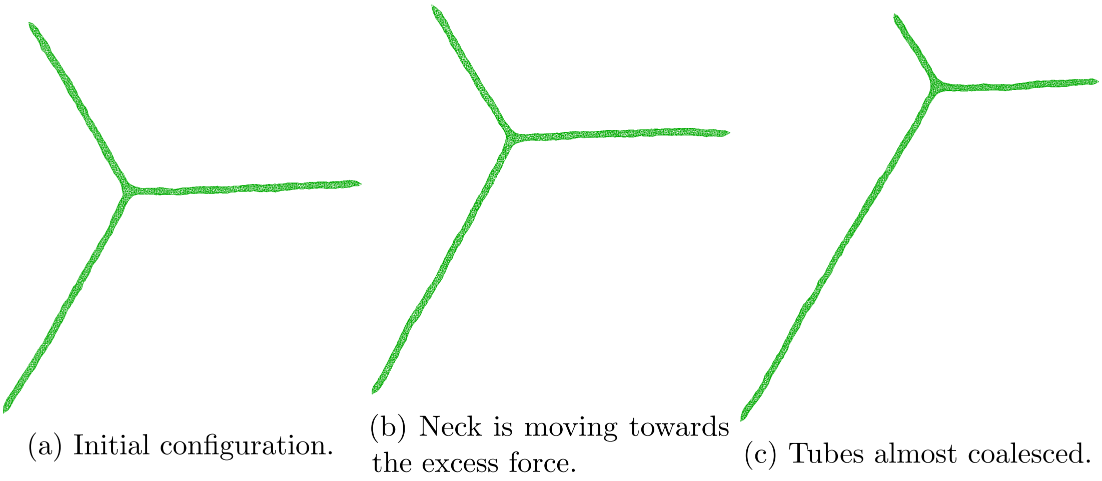
(a) Initial configuration.
(b) Neck is moving towards the excess force.
(c) Tubes almost coalesced.

Figure 7.18: Intermediate configurations obtained by varying the angle $\Delta\varphi$. The end configuration is a long tube ($\Delta\varphi = 3°$; $F_{\text{ext}} = 90$).

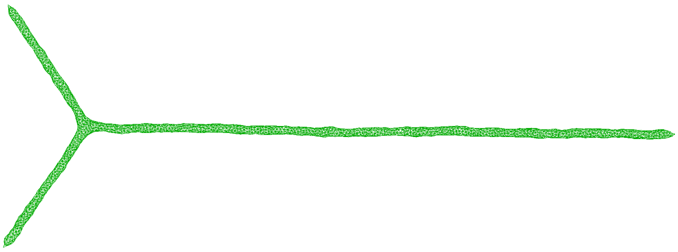

Figure 7.19: Intermediate configuration, obtained by varying the angel between two tubes. The two tubes eventually coalesce and the final configuration is one long tube ($\alpha = 108°$; $F_{\text{ext}} = 90$).

System (i)

For large variations of the angle $\Delta\varphi$, coalescence of two of the tubes occurs very quickly. These are the two tubes with the smallest angle between them. For smaller angle variations, the system seems stable initially, but coalescence occurs eventually. This is illustrated in Figure 7.18. One can observe that the neck gradually moves in the direction of the excess force, trying to minimize the energy of the system, by preserving the 120° angle between all three arms. In the end, this is not possible because the direction of the forces is fixed, so this point can never be reached and the neck eventually reaches the end of the tube and vanishes.

System (ii)

In this setup coalescence also quickly occurs for angles α far below 120°. For smaller variations the process is much slower, but in the end two tubes coalesce and the final configuration is one long tube. A snapshot of an intermediate configuration is shown in Figure 7.19.

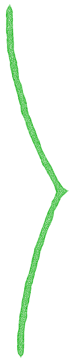

Figure 7.20: Final stable configuration reached in system (iii), $F_{\text{ext}} = 70$.

System (iii)

In this setup, the third tube progressively vanishes and is absorbed by the system. In this case the final configuration is, however, not a straight long tube, but a bent tube as shown in Figure 7.20. This happened for all forces analyzed. One can clearly say that in this case of angle deviation, with an external force fixing the pulling direction, the branch structure is not stable.

7.4.2 Varying the Angle between the Arms - Fixed Anchor

One could clearly observe that none of the systems analyzed above are stable, because the neck structure is moving towards the excess force, trying to maintain a 120° angle between the arms, to minimize the overall curvature energy of the system. The directions of the forces are, however, fixed, which means this point can never be reached. Instead the neck structure eventually reaches the end of the tube, hence one long tube forms.

To confirm this hypothesis, we set up another system, where instead of keeping the directions for the forces fixed, the forces were oriented towards three points chosen on an imaginary big outer sphere, to see how the system evolves. One can in fact observe the same movement of the neck as before, but this time the energetically most favorable configuration with 120° between the tubes can in fact be reached.

Some snapshots of the time evolution of this process are shown in Figure 7.21. The points were positioned in such a way that the initial angles between the forces were 180° and 90°, so similar to the setup in system (iii) discussed above, but with fixed points instead of directions. This allowed the system to rearrange and reach a stable configuration with 120° between all three arms, as shown in Figure 7.21c. The outcome of all simulations was the same, wherever the points were placed on the hypothetical outer sphere. In all setups, the angle between the three tubes in the final configuration was 120°, the only difference was the length of the individual arms.

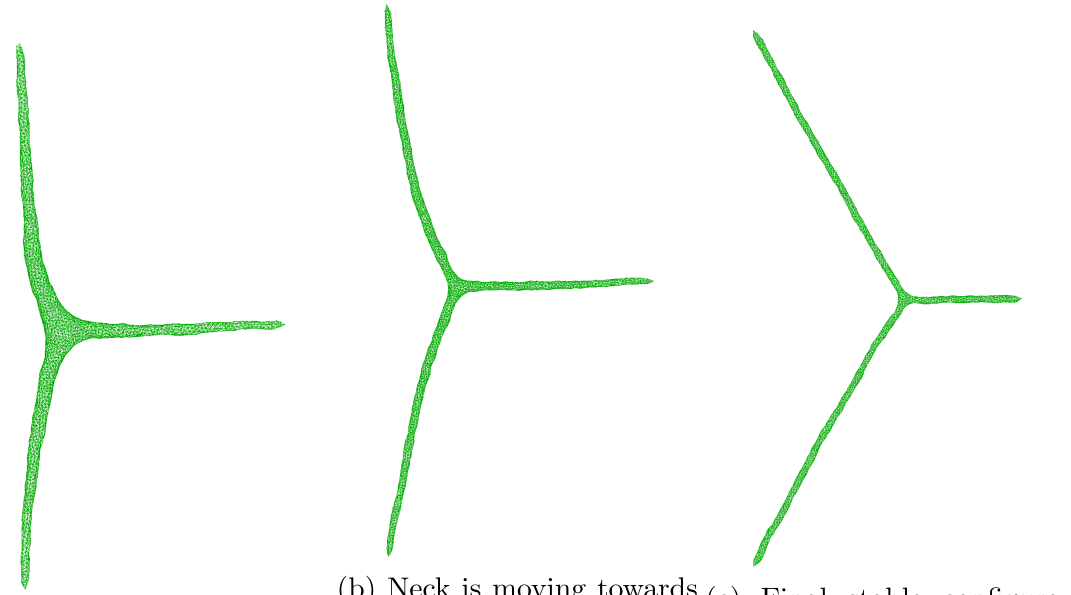

(a) Initial configuration.

(b) Neck is moving towards the center between the three points.

(c) Final stable configuration.

Figure 7.21: Snapshots of the time evolution of a branched structure, where the external forces were pointing towards three fixed points on a hypothetical big outer sphere. The neck structure moves towards the center of these points, such that the angel between all three arms is 120°, which minimizes the energy of the system ($F_{\text{ext}} = 110$).

7.4.3 Fixing the Reduced Volume while Releasing the External Force

It was further investigated if it is possible to stabilize the tubular and branched structures by a mechanism other than an external force. Therefore, simulations were performed starting from a tube or branch for which the reduced volume of the system was kept fixed, but the external force no longer applied. For the analyzed reduced volumes ($\nu < 0.3$) the tube and branch structures are not the energetically most favorable configurations, this would be a stromatocyte (see Figure 4.1f). They could, nevertheless, be local energy minima in which the system is trapped. Metastable tubes stabilized with this mechanism have previously been reported in Ref. 113.

Tube

Investigations of the tubular structure indicate that some of the tubes are actually metastable. In fact, for thicker tubes with $\nu > 0.19$ no transition to a stromatocyte could be observed, even for very long simulation times. When releasing the pulling force, the tubes start to bend slightly, but they keep their tubular shape, as exemplarily shown in Figure 7.22.

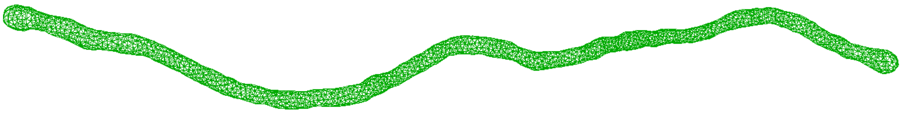

Figure 7.22: Tube stabilized by keeping the reduced volume fixed at $\nu = 0.19$. No external forces are applied. The tube is not perfectly straight any more, as it was when applying the force, but it keeps its tubular shape.

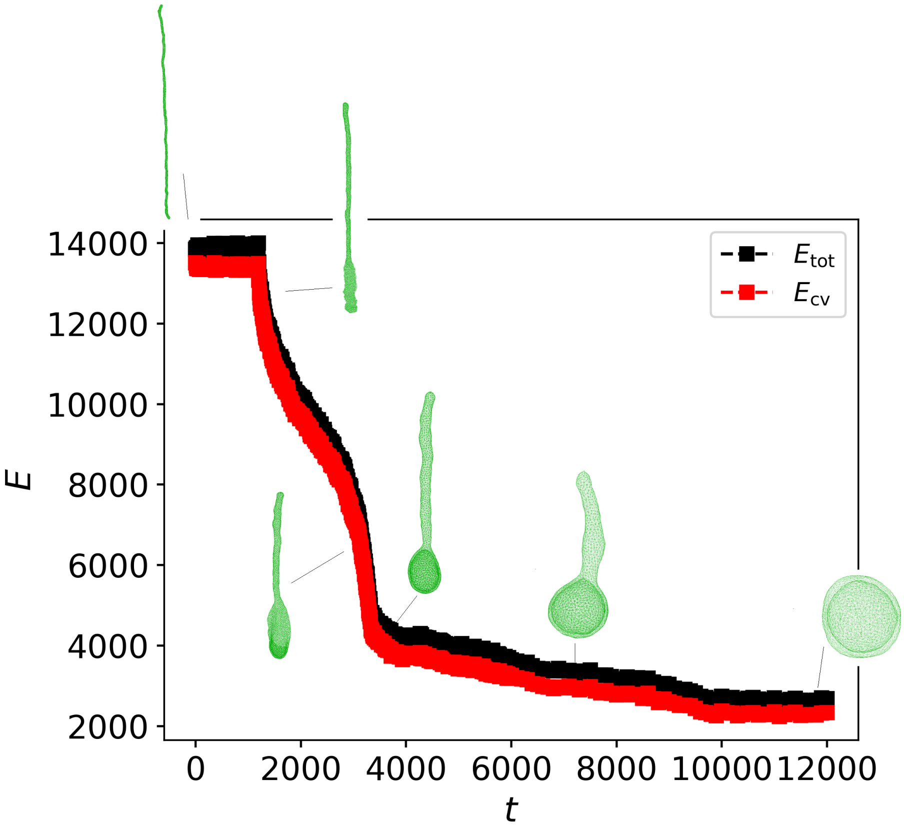

Figure 7.23: Time evolution of the energy for the transition from a tube to a stromatocyte. The reduced volume was kept fixed, while the external force was released. The force needed to stabilize the original tube was $F_{\text{ext}} = 90$ and the reduced volume is $\nu = 0.15$. The tube does not transform immediately, but it eventually starts to flatten and wrap around itself to form a stromatocyte. The intermediate configuration, a stromatocyte with a tube protruding from it, is stable for a relatively long time.

Thinner tubes, with $\nu \lesssim 0.16$, seem to be metastable initially. However, at some point the system starts to form a thin sheet-like structure at one end, which is the onset for the transformation into a stromatocyte. These sheet structures get broader and eventually start to wrap around themselves, so that the structure almost looks like a spoon. This 'spoon' then evolves into a stromatocyte with a tube protruding from it. This intermediate configuration can be observed for a long time, until the tube is eventually completely absorbed into the stromatocyte.

This transition and the corresponding time evolution of the energy are exemplarily shown in Figure 7.23. The tube is metastable initially, which is confirmed by the curvature energy being roughly constant at the beginning. At some point, the formation of the sheet starts, which causes a rapid drop in the curvature energy until a stromatocyte with a tube protruding from it is formed. This tube is then slowly absorbed and the energy continues to decrease smoothly, until a pure stromatocyte is formed and the system is in its energetically most favorable configuration. The point at which the formation of the sheet started was not always the same, but varied for each simulation. It is also very interesting to see that, even though the tubes are instable, they maintain their initial tubular structure for much longer timescales than the branch structure, where the whole transformation process took only about $t \approx 1500$, as will be discussed below.

Our observation of the formation of stromatocytes from tubes is in contrast to the simulation results reported in Ref. 113, where (meta)stable tubes were observed for all reduced volumes. It is possible that the simulations performed in this reference were simply not long enough to observe the long-time deformation process described above (c.f. Figure 7.23). It could, however, also be caused by a slightly different implementation of the triangulated membrane model, which has been reported to affect some configurations, particularly if the discretization of the membrane is poor.[112] Although it would definitely be interesting to further investigate this, we are confident to conclude from our model with suitable discretization that the above described transition is indeed physical and the tube becomes unstable.

Branched Structures

The simulations revealed that the branch structures are actually very unstable. When releasing the external force, the branch immediately starts to deform and turn into a stromatocyte. This was the case for all reduced volumes, $0.3 > \nu > 0.1$, investigated. An exemplary time evolution of the transformation can be found in Figure 7.24, which shows the energy profile and the corresponding conformations of the system.

First, the region around the neck starts to broaden and flatten, which seems to be the weak spot of the structure. Triggered by this, one of the tubes starts to

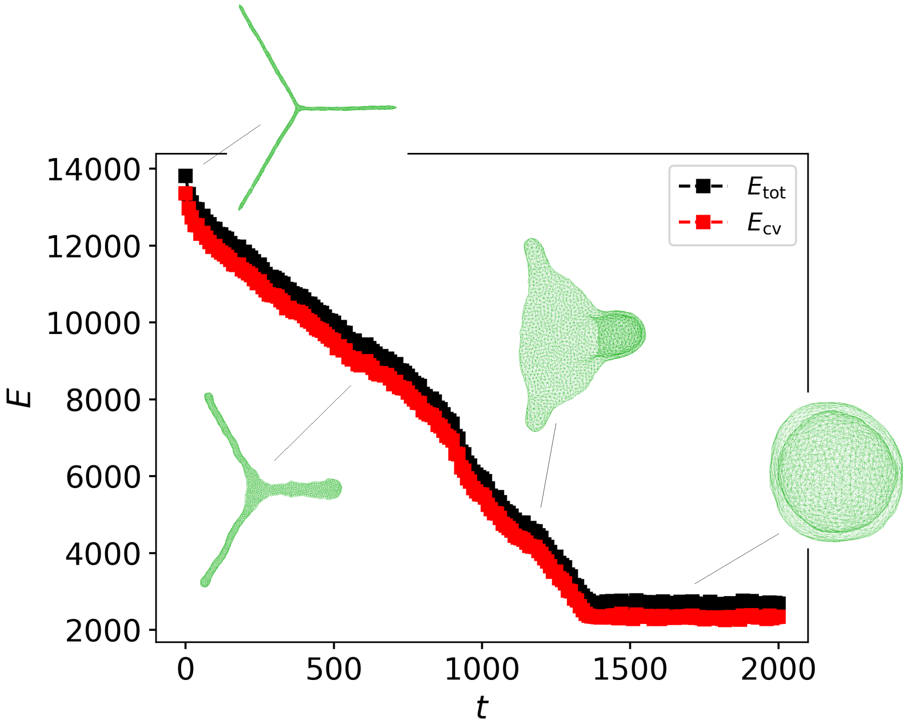

Figure 7.24: Time evolution of the energy for the transition from a branch to a stromatocyte. The reduced volume was kept fixed, while the external force was released. The force needed to stabilize the original branch was $F_{\mathrm{ext}} = 90$ and the reduced volume is $\nu = 0.15$.

get broader and flatter and eventually opens up to wrap around itself to form the opening for the stromatocyte. Finally, the other two arms get absorbed gradually into the stromatocyte.

The stromatocytes formed are clearly the energetically most favorable configurations for the given low reduced volumes. This is confirmed by the time evolution of the energy profile. The important and nontrivial observation here is that the branch structure is not even metastable. The fact that it cannot be stabilized by the reduced volume alone indicates that there has to be another type of stabilizing mechanism to form (meta)stable tubular membrane networks. In the following we will show that such a mechanism could be given by bilayer asymmetries or curvature inducing proteins.

7.4.4 Fixing the Overall Curvature

We have found that the constraint of fixing the reduced volume alone is not sufficient to stabilize tubular and branched structures. Therefore, an additional constraint on the overall curvature of the system was set, to further control the system. This can be motivated by proteins that can induce a spontaneous curvature of the membrane, as discussed in Chapter 2,[6;16–20] or by a difference in the area of the two layers of

Structure	Reduced Volume ν	Additional Constraint	Δa
sphere	1.0	-	1.0
prolate vesicle	0.8	-	1.0
oblate vesicle	0.6	-	1.0
stromatocyte	0.3	-	0.8
stromatocyte	0.2	-	0.2
tube	0.44	$F_{\text{ext}} = 30$	1.8
tube	0.26	$F_{\text{ext}} = 50$	2.8
tube	0.19	$F_{\text{ext}} = 70$	3.9
tube	0.14	$F_{\text{ext}} = 90$	4.9
branch	0.5	$F_{\text{ext}} = 30$	1.6
branch	0.27	$F_{\text{ext}} = 50$	2.8
branch	0.19	$F_{\text{ext}} = 70$	3.8
branch	0.14	$F_{\text{ext}} = 90$	4.9

Table 7.1: Typical values for the overall curvature of the structures, represented by the renormalized area difference Δa. Higher values indicate stronger overall curvature.

the lipid bilayer, which also induces curvature. In the simulations, this additional curvature is introduced by setting a constraint on the renormalized area difference Δa introduced in Section 3.3.1. This can be modeled by adding an additional potential to the overall energy of the system. In the ADE model (c.f. Section 3.3.1) this term has the same shape as the potentials that were used for controlling the area and volume.

We adopt this model here, therefore the constraint potential has the form:

$$U_{\Delta a} = \frac{1}{2} k_{\Delta a} (\Delta a - \Delta a_0)^2 \tag{7.13}$$

where $k_{\Delta a}$ indicates the strength of the constraint, Δa is the renormalized area difference calculated by Equation 3.23 and Δa_0 the target value. The strength of the constraint was set to $k_{\Delta a} = 1$ in all simulations.

In Table 7.1 some typical values of Δa for the structures investigated previously are given. For a sphere the area difference is one (by definition). For the tube and branch structures Δa is significantly larger than one, because they are thinner and thus clearly more strongly curved. Interestingly, Δa is smaller than one for the stromatocytes. This is the case because the inner sphere is curved in the other direction than the outer sphere, so these contributions compensate each other.

In Figure 7.25 the change of the area difference Δa for the transition from a tube/branch to a stromatocyte is shown (the corresponding energy profiles are given in Figures 7.23 and 7.24). As expected, one can observe a clear and significant drop in the overall curvature, which suggests, that fixing the overall curvature of the system could suppress this transition.

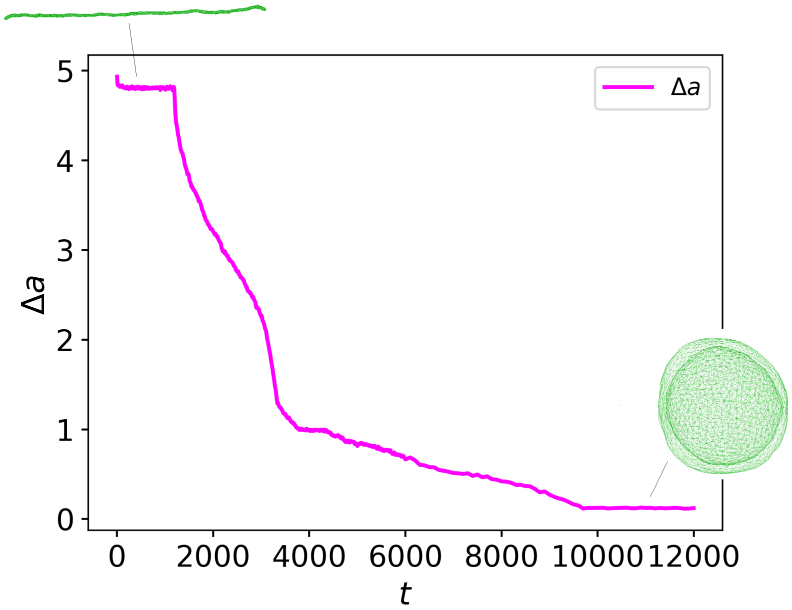

(a) Tube to stromatocyte

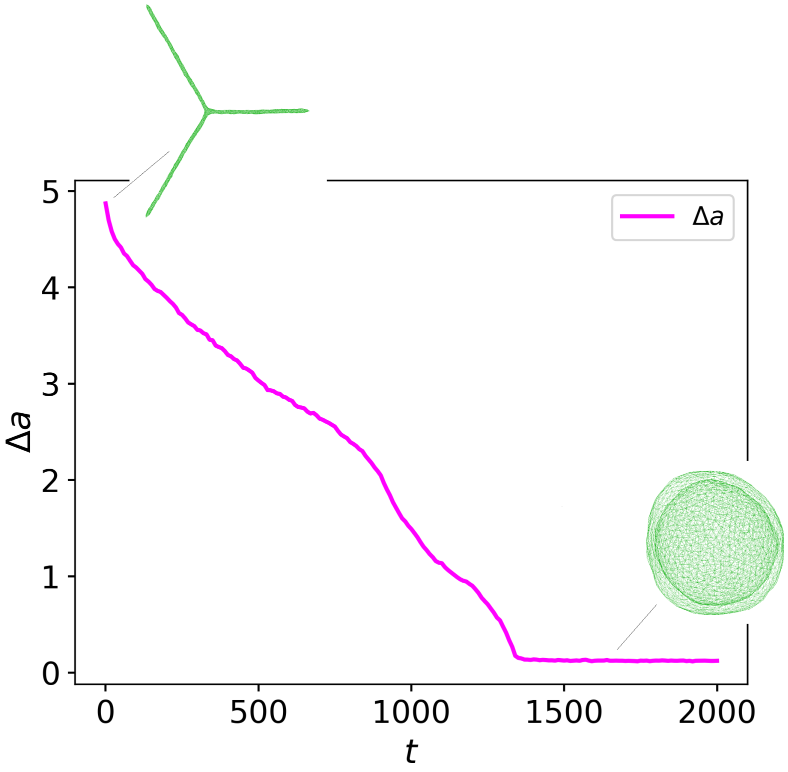

(b) Branch to stromatocyte

Figure 7.25: Time evolution of the renormalized area difference, Δa, for the transition from a tube/branch to a stromatocyte (Original structure: $F_{\text{ext}} = 90$; $\nu = 0.14$).

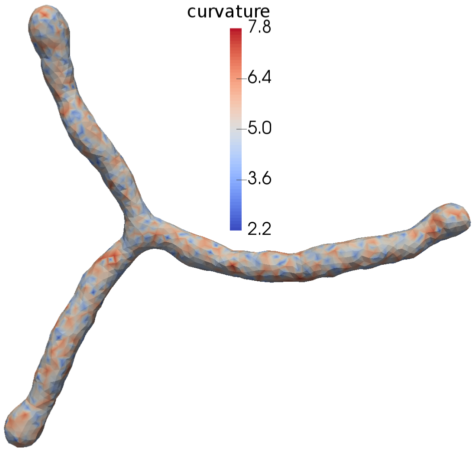

(a) branch: $\nu = 0.27$; $\Delta a_0 = 2.8$

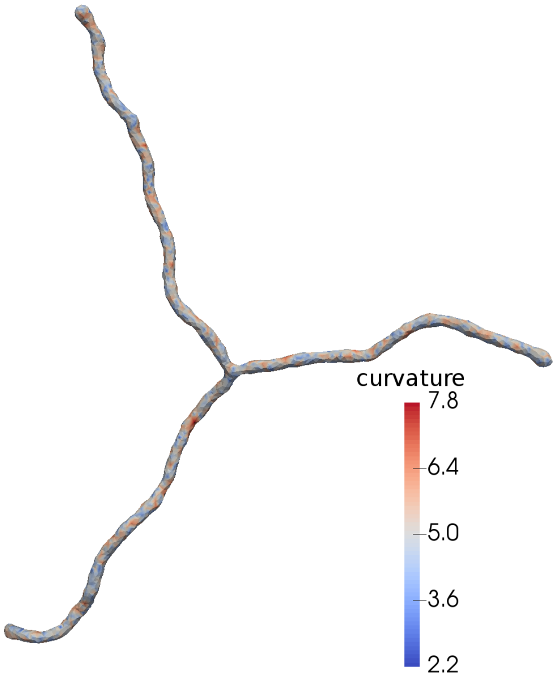

(b) branch: $\nu = 0.14$; $\Delta a_0 = 4.9$

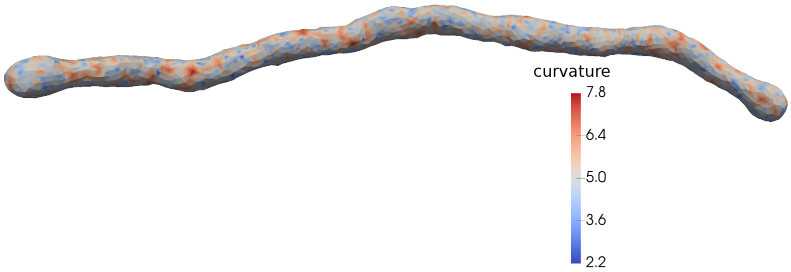

(c) tube: $\nu = 0.27$; $\Delta a_0 = 2.8$

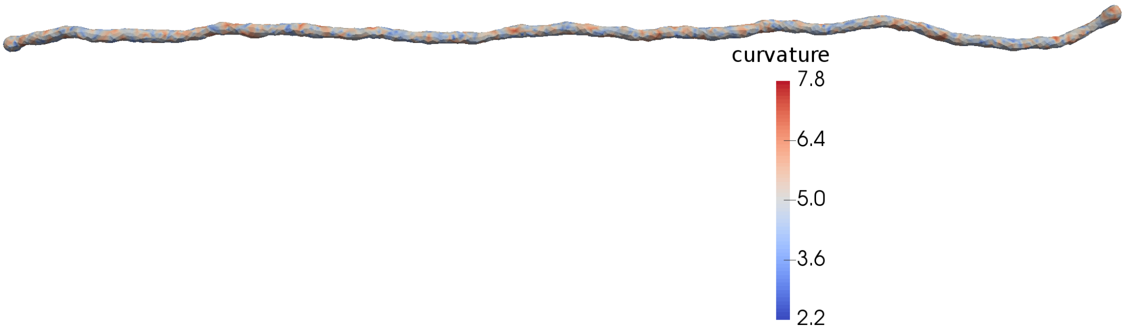

(d) tube: $\nu = 0.14$; $\Delta a_0 = 4.9$

Figure 7.26: Snapshots of tube and branch structures stabilized by fixing the reduced volume ν and the overall curvature of the system Δa.

We therefore performed simulations with fixed Δa_0, using the potential in Equation 7.13. The branched and tubular structures were simulated setting Δa_0 to the corresponding steady state values, determined with the externally applied pulling forces. This, in fact, stabilizes both the tube and the branch structures. Some snapshots are shown in Figure 7.26, in which the color indicates the strength of the curvature.

Both structures are not perfectly straight any more, but slightly bent due to entropic reasons. The overall conformation (tube or branch), however, is (meta)stable. This shows that by setting a constraint on the overall curvature via Δa, one can control and stabilize structures which were initially unstable. This is a very important observation, because it explains how tubular networks in nature can exist, although we have shown that branches become unstable as soon as a fixed anchor is removed.

8

Conclusions and Outlook

In this thesis, a dynamically-triangulated membrane model was employed to investigate conformational changes of biological membranes on large scales. The model is based on a continuum description, in which the membrane is described as a smoothly curved surface and the energetics are derived from the Helfrich theory. This general description allows to access significantly larger length and time scales than typical atomistic or coarse-grained simulations can reach.

In the first part, the model was tested and validated. Tubular structures protruding from vesicles were simulated by applying an external force. In nature, this is one possible generation mechanism. We classified the lengths and radii of the tubes obtained for different forces and validated them using analytical approximations and other data from the literature. Our results were further complemented using a direct minimization scheme for the Helfrich Hamiltonian and closed spherical vesicles, exploiting the rotational symmetry of the problem. All in all, the results obtained by the different methods were consistent, but the analysis also revealed small discrepancies and potential limitations of the different models.

In the second part, the focus lay on branched structures, which are omnipresent in biological cells, mostly in the form of individual branched tubes or complex network structures. We could clearly show that the neck region of a branched structure, i.e. the point where the three tubes of a branch meet, is energetically favorable compared to a simple tubular structure, because the neck is less strongly curved. We could, however, identify three problems when it comes to the formation and stability of branched structures. First, the creation of the neck appears to require the transition over a significant energy barrier, making it more difficult to create such branches compared to tubular structures, although the latter are energetically less favorable. Second, in all simulations we could observe that the branches are only stable if the angle between the incoming tubes is exactly 120°, in agreement with experimental observations, where only these angles were found to be stable. As soon as this constraint was not fulfilled, the neck started to move in a zipper-like mechanism, which often led to a disintegration of the neck when it reached the end of the tube. Third, the branched structures are actually very unstable, different from what is known for most tubular structures. As soon as the force generating them is released, the arms immediately start to retract, which suggests that there has to be another stabilizing mechanism. Our first attempt was fixing the area and volume ratio, i.e. the reduced volume ν, of the systems and then releasing the external force. This technique stabilized thick tubular structures, but thin tubes and branches are still unstable. The latter transform into stromatocytes, the energetically most favorable configuration for low reduced volumes. We therefore added an additional constraint to fix and control the overall curvature of the structures. In nature this could be caused by an area difference between the two layers of the lipid bilayer, or by proteins that affect the curvature. Fixing both the reduced volume and the overall curvature allowed, in fact, to stabilize all tubular and branched structures. These results show that the branched networks observed in nature need to be either anchored to other structures within the cell (e.g. organelles or filaments), stabilized by proteins controlling the curvature or have significant bilayer asymmetries. It is of course likely, that in nature a combination of the different mechanisms occurs.

The model employed is generally very suited for investigating membrane dynamics on large scales. In this thesis, only a few problems could be addressed, but there are many more potential applications for the model. One is simulating double walled vesicles, i.e. one smaller vesicle inside a bigger one, and observing conformational changes of the inner vesicle by varying its area. This has already been analyzed briefly in a Bachelor's thesis written in our group[174] and could be expanded upon further. Another interesting task worth pursuing is adding more detail to the model. So far it is very general, assuming the same properties (stiffness, bending rigidity etc.) homogeneously distributed across the whole structure. Biological membranes are, however, much more detailed and complicated, having various domains with different properties. This task is, in fact, currently undertaken in a Master's thesis in our group, by attributing different stiffnesses and spontaneous curvatures to individual vertices. This allows to observe the rearrangement of regions, and can be used for generating (and stabilizing) tubular and sheet like structures. It could also be worth performing more simulations with a finer discretization, to investigate thinner structures and get more precise values for the energies of the different structures and their components. Undoubtedly, membrane dynamics is a very interesting and active field of research, where computer simulations could significantly contribute to a better understanding complementary to experiments.

A

Shapes of Final Configurations

A.1 Simulations of Vesicles - Tube Formation

This is an overview of the shapes of the final stable configuration for a vesicle with one or two external forces applied.

One External Force

$\nu = 0.6$:

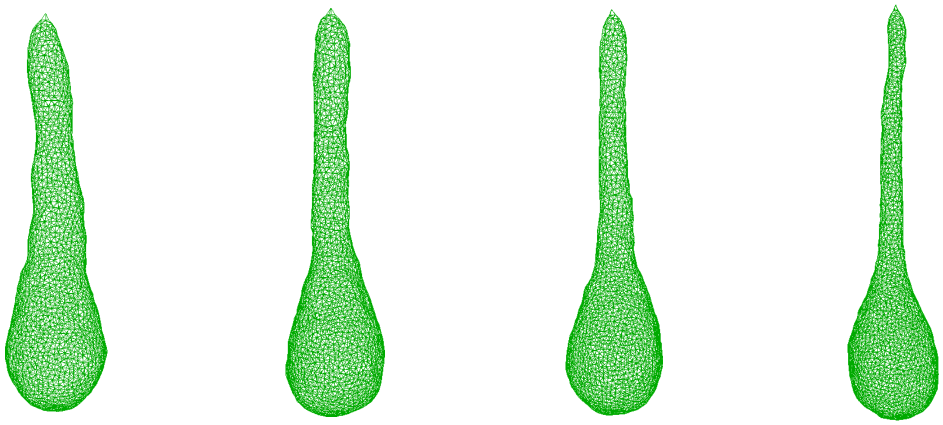

(a) $F_{\text{ext}} = 40$ (b) $F_{\text{ext}} = 50$ (c) $F_{\text{ext}} = 60$ (d) $F_{\text{ext}} = 70$

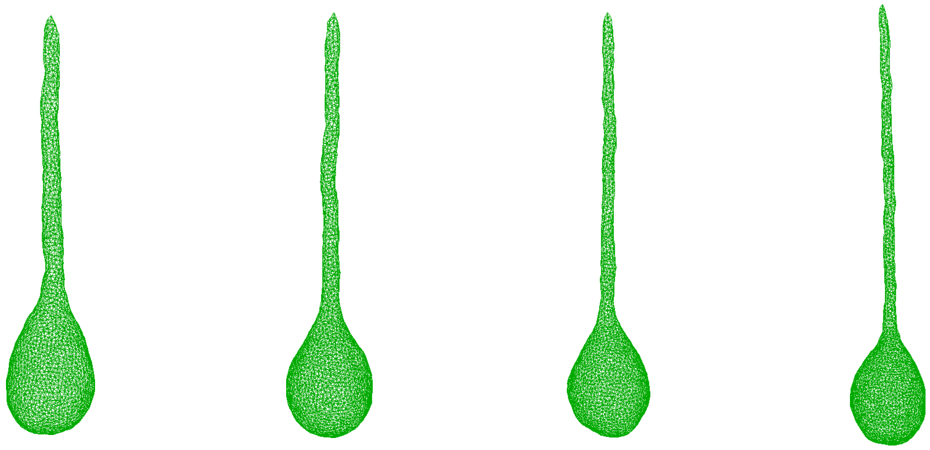

(e) $F_{\text{ext}} = 80$ (f) $F_{\text{ext}} = 90$ (g) $F_{\text{ext}} = 100$ (h) $F_{\text{ext}} = 110$

Figure A.1: Final stable configurations for a vesicle with one external force F_{ext} applied ($\nu = 0.6$).

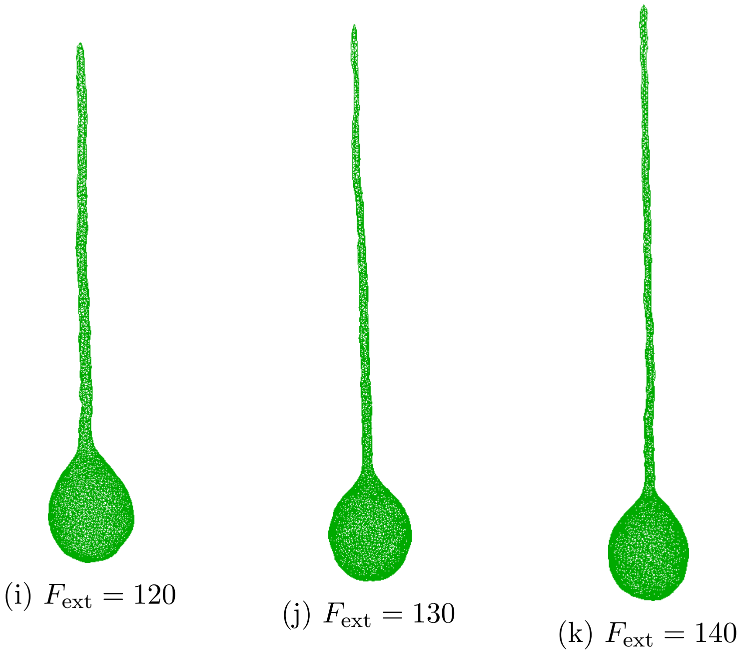

(i) $F_{\text{ext}} = 120$ (j) $F_{\text{ext}} = 130$ (k) $F_{\text{ext}} = 140$

Figure A.1: Final stable configurations for a vesicle with one external force F_{ext} applied ($\nu = 0.6$).

$\nu = 0.7$:

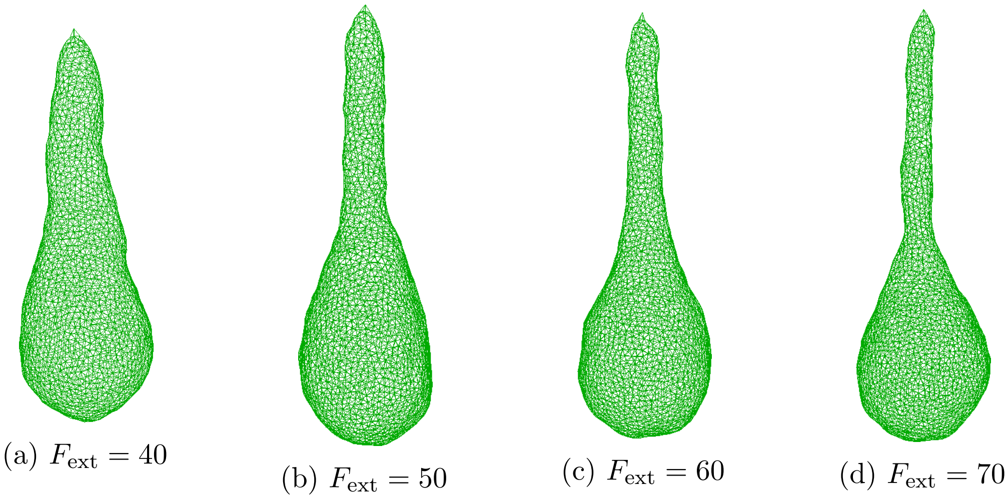

(a) $F_{\text{ext}} = 40$ (b) $F_{\text{ext}} = 50$ (c) $F_{\text{ext}} = 60$ (d) $F_{\text{ext}} = 70$

Figure A.2: Final stable configurations for a vesicle with one external force F_{ext} applied ($\nu = 0.7$).

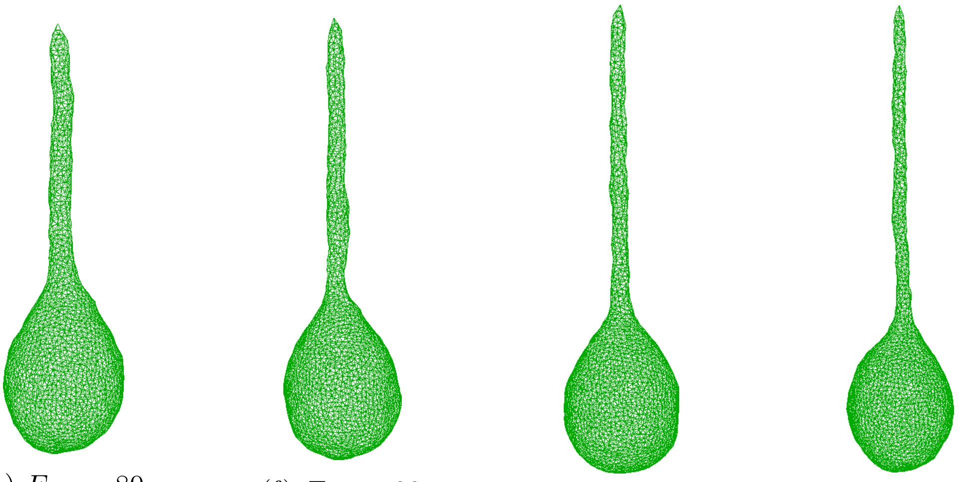

(e) $F_{\text{ext}} = 80$ (f) $F_{\text{ext}} = 90$ (g) $F_{\text{ext}} = 100$ (h) $F_{\text{ext}} = 110$

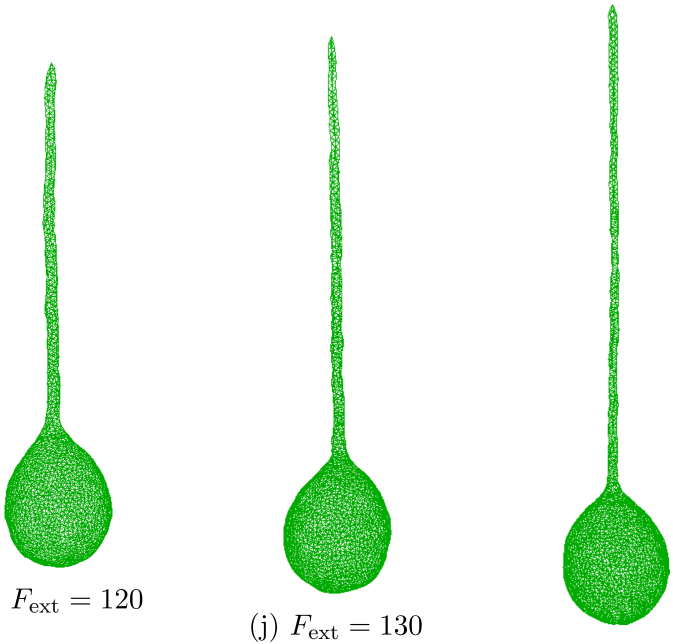

(i) $F_{\text{ext}} = 120$ (j) $F_{\text{ext}} = 130$ (k) $F_{\text{ext}} = 140$

Figure A.2: Final stable configurations for a vesicle with one external force F_{ext} applied ($\nu = 0.7$).

$\nu = 0.8$:

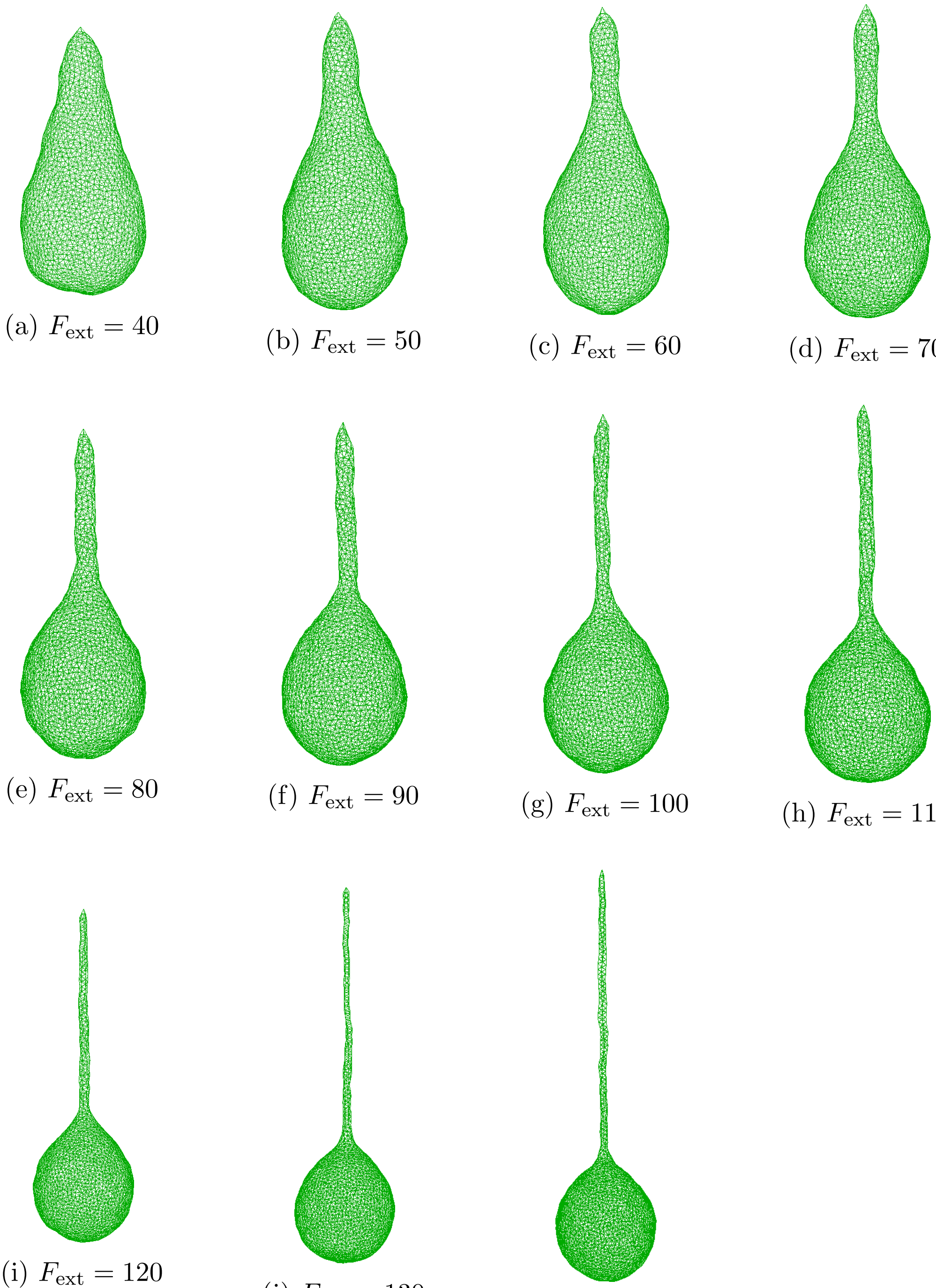

(a) $F_{\text{ext}} = 40$ (b) $F_{\text{ext}} = 50$ (c) $F_{\text{ext}} = 60$ (d) $F_{\text{ext}} = 70$

(e) $F_{\text{ext}} = 80$ (f) $F_{\text{ext}} = 90$ (g) $F_{\text{ext}} = 100$ (h) $F_{\text{ext}} = 110$

(i) $F_{\text{ext}} = 120$ (j) $F_{\text{ext}} = 130$ (k) $F_{\text{ext}} = 140$

Figure A.3: Final stable configurations for a vesicle with one external force F_{ext} applied ($\nu = 0.8$).

Two External Forces

$\nu = 0.6$:

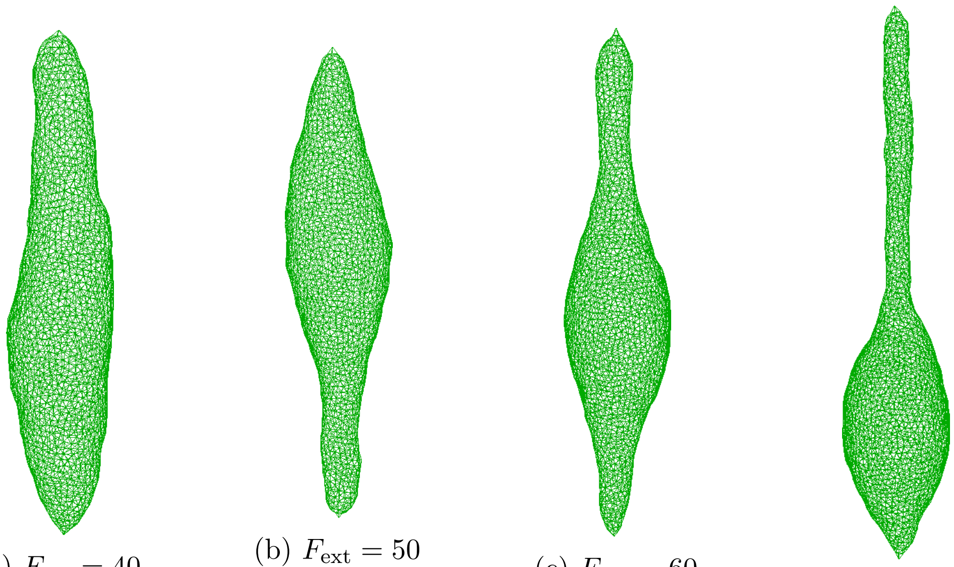

(a) $F_{\text{ext}} = 40$ (b) $F_{\text{ext}} = 50$ (c) $F_{\text{ext}} = 60$ (d) $F_{\text{ext}} = 70$

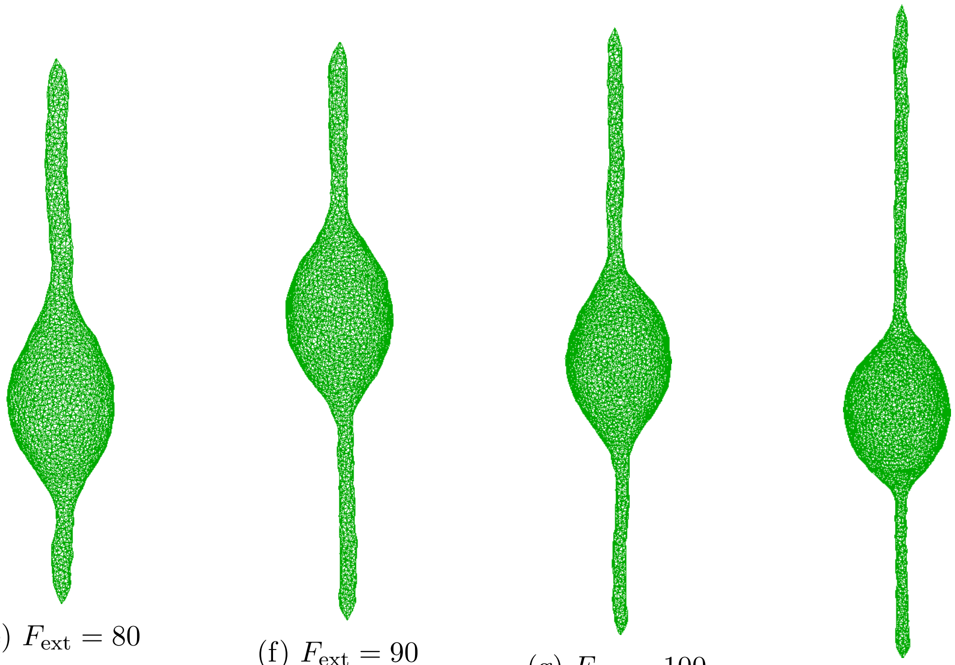

(e) $F_{\text{ext}} = 80$ (f) $F_{\text{ext}} = 90$ (g) $F_{\text{ext}} = 100$ (h) $F_{\text{ext}} = 110$

Figure A.4: Final stable configurations for a vesicle with two external forces F_{ext} applied ($\nu = 0.6$).

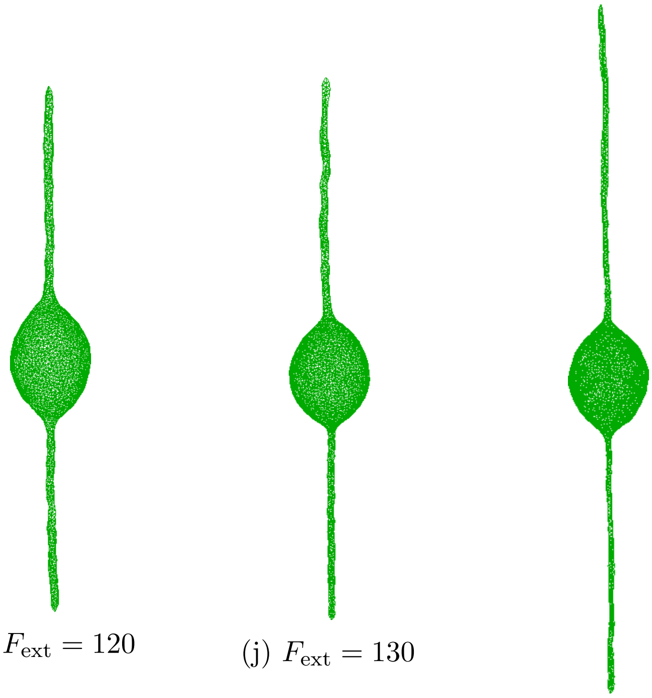

(i) $F_{\text{ext}} = 120$ (j) $F_{\text{ext}} = 130$ (k) $F_{\text{ext}} = 140$

Figure A.4: Final stable configurations for a vesicle with two external forces F_{ext} applied ($\nu = 0.6$).

$\nu = 0.7$:

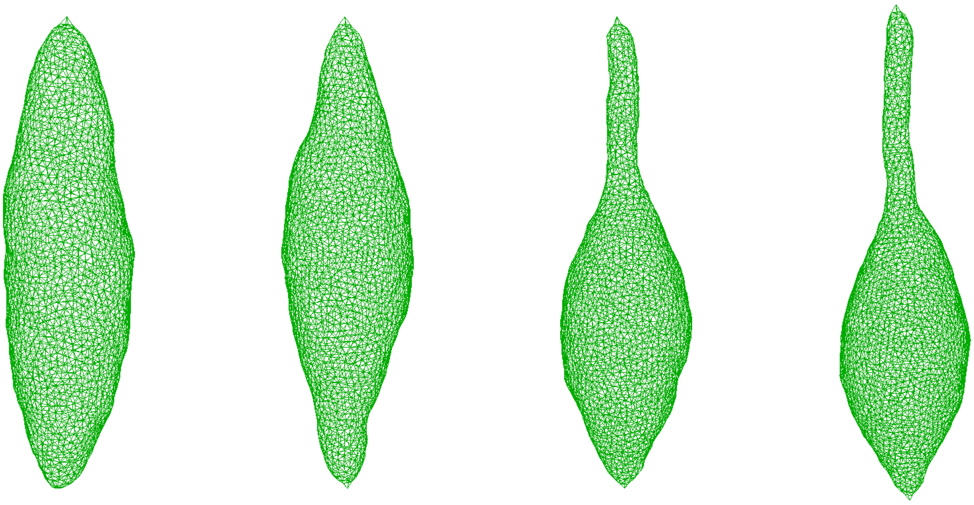

(a) $F_{\text{ext}} = 40$ (b) $F_{\text{ext}} = 50$ (c) $F_{\text{ext}} = 60$ (d) $F_{\text{ext}} = 70$

Figure A.5: Final stable configurations for a vesicle with two external forces F_{ext} applied ($\nu = 0.7$).

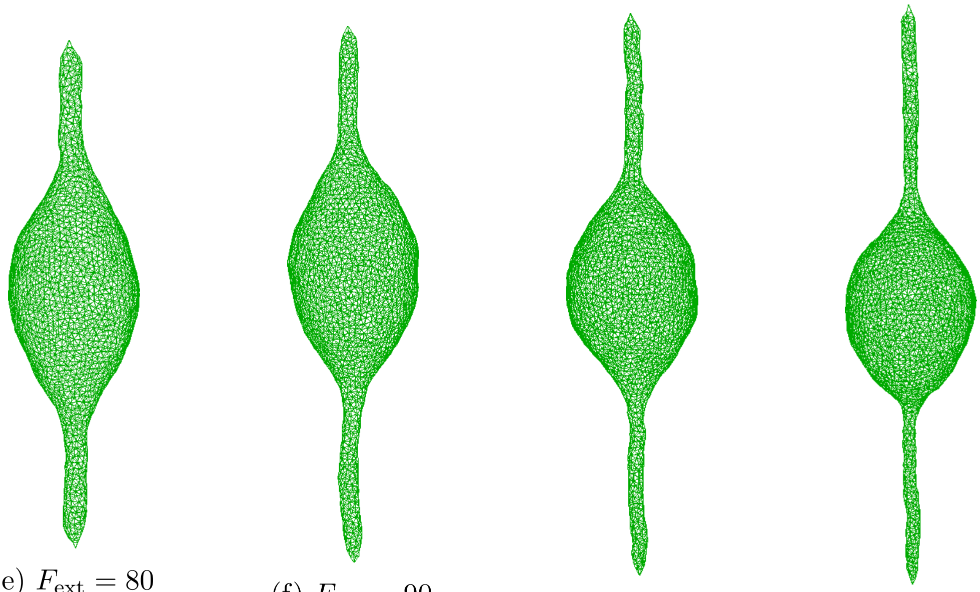

(e) $F_{\text{ext}} = 80$ (f) $F_{\text{ext}} = 90$ (g) $F_{\text{ext}} = 100$ (h) $F_{\text{ext}} = 110$

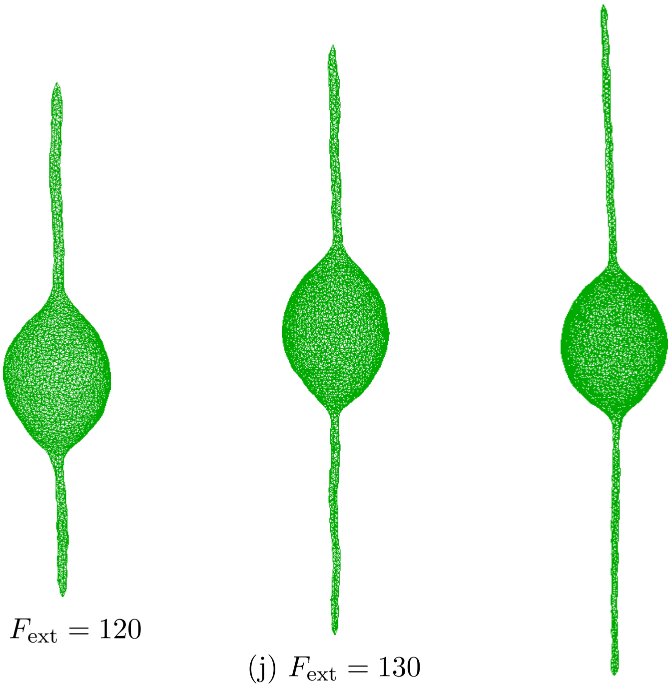

(i) $F_{\text{ext}} = 120$ (j) $F_{\text{ext}} = 130$ (k) $F_{\text{ext}} = 140$

Figure A.5: Final stable configurations for a vesicle with two external forces F_{ext} applied ($\nu = 0.7$).

$\nu = 0.8$:

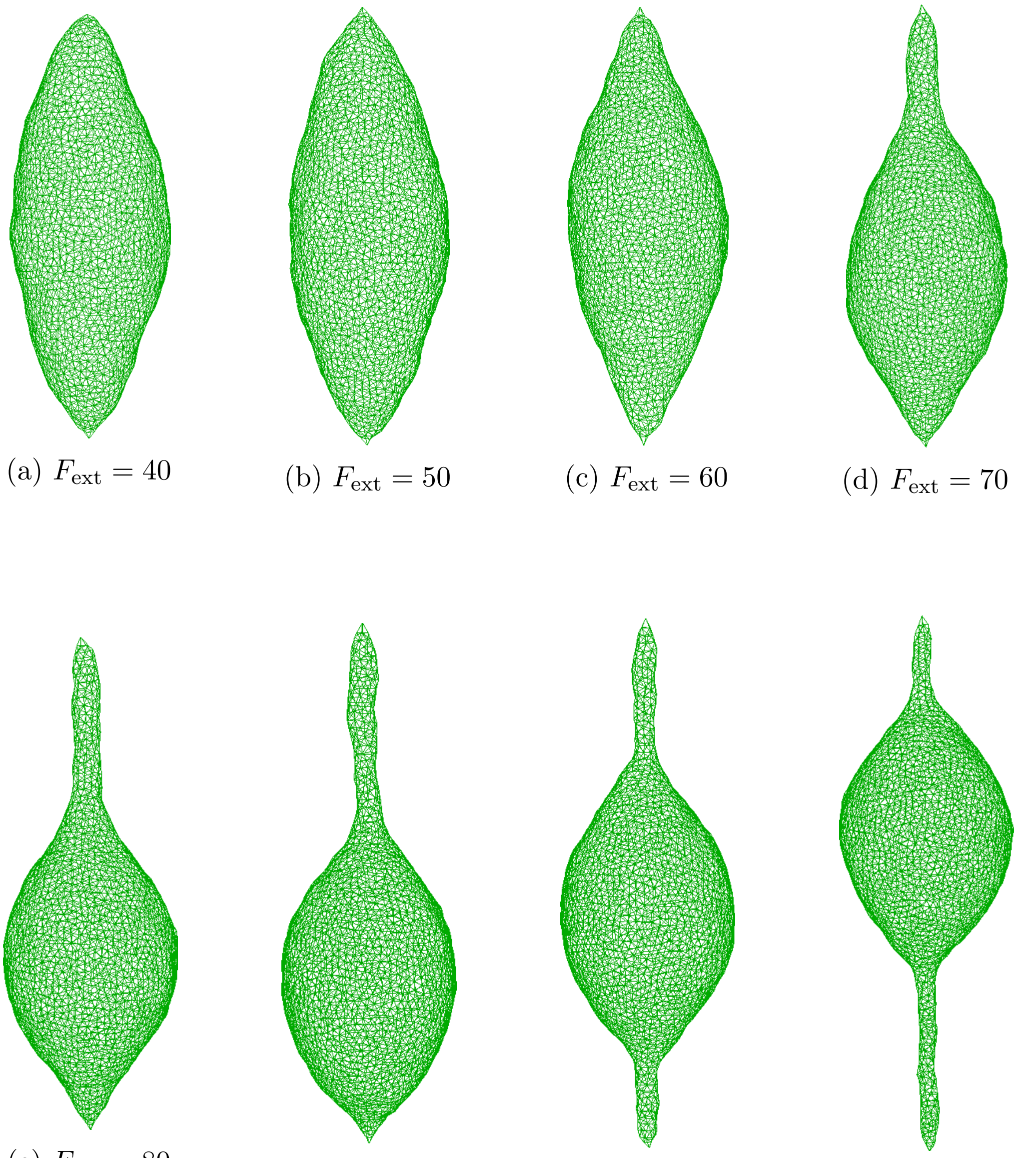

(a) $F_{\text{ext}} = 40$ (b) $F_{\text{ext}} = 50$ (c) $F_{\text{ext}} = 60$ (d) $F_{\text{ext}} = 70$

(e) $F_{\text{ext}} = 80$ (f) $F_{\text{ext}} = 90$ (g) $F_{\text{ext}} = 100$ (h) $F_{\text{ext}} = 110$

Figure A.6: Final stable configurations for a vesicle with two external forces F_{ext} applied ($\nu = 0.8$).

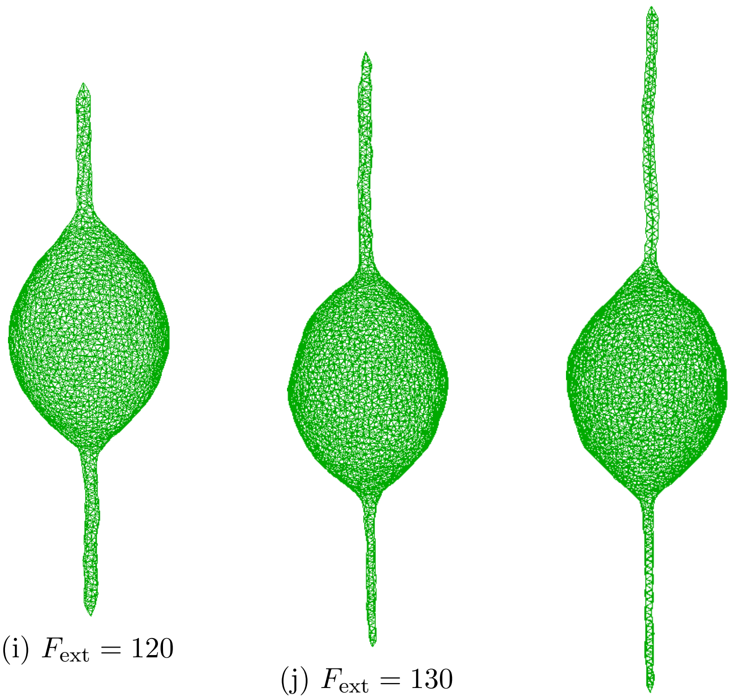

(i) $F_{\text{ext}} = 120$

(j) $F_{\text{ext}} = 130$

(k) $F_{\text{ext}} = 140$

Figure A.6: Final stable configurations for a vesicle with two external forces F_{ext} applied ($\nu = 0.8$).

A.2 Vesicle with Tubes - Direct Minimization

This is an overview of the shapes obtained by direct minimization.

$\nu = 0.6$:

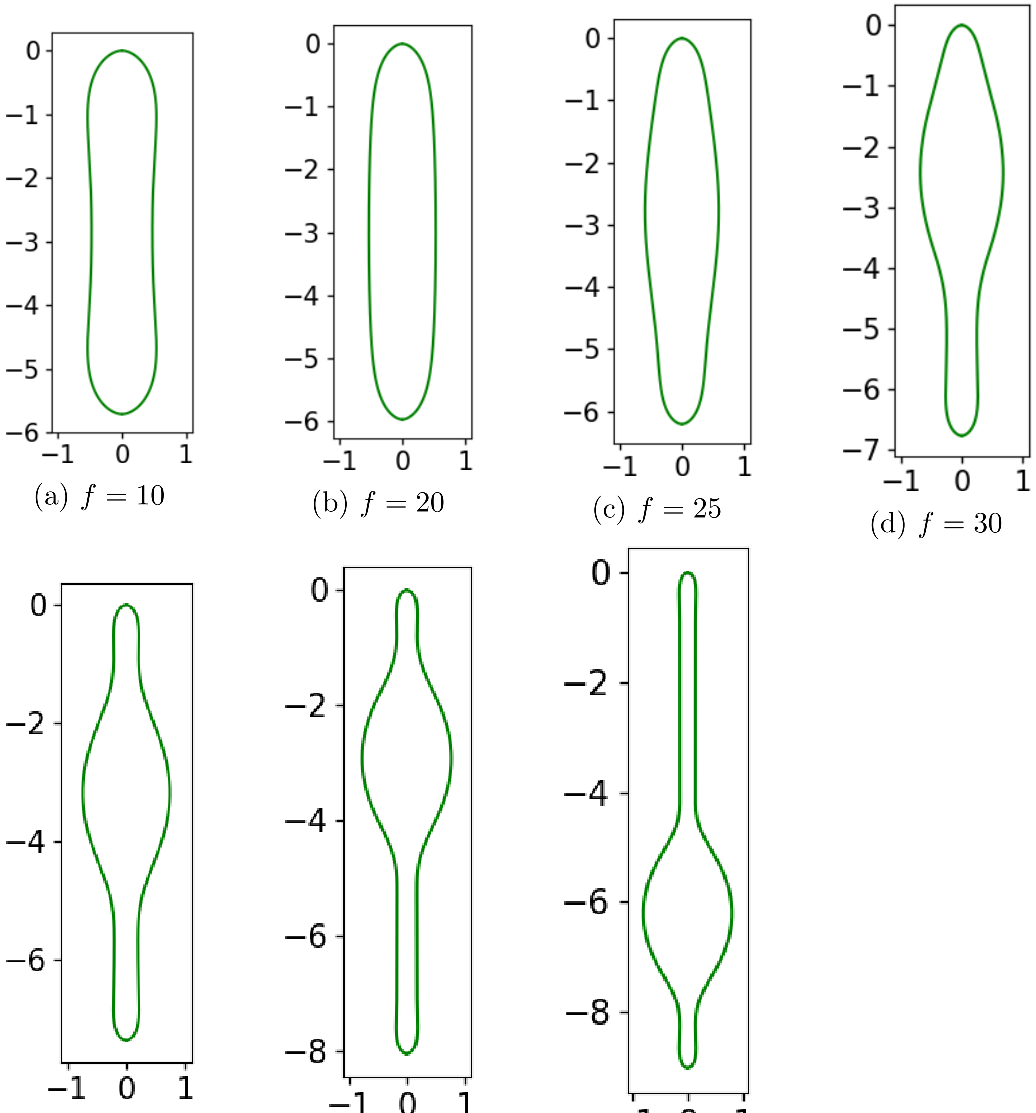

(a) $f = 10$ (b) $f = 20$ (c) $f = 25$ (d) $f = 30$

(e) $f = 35$ (f) $f = 40$ (g) $f = 50$

Figure A.7: Shapes obtained from direct minimization for different forces f ($\nu = 0.6$).

$\nu = 0.7$:

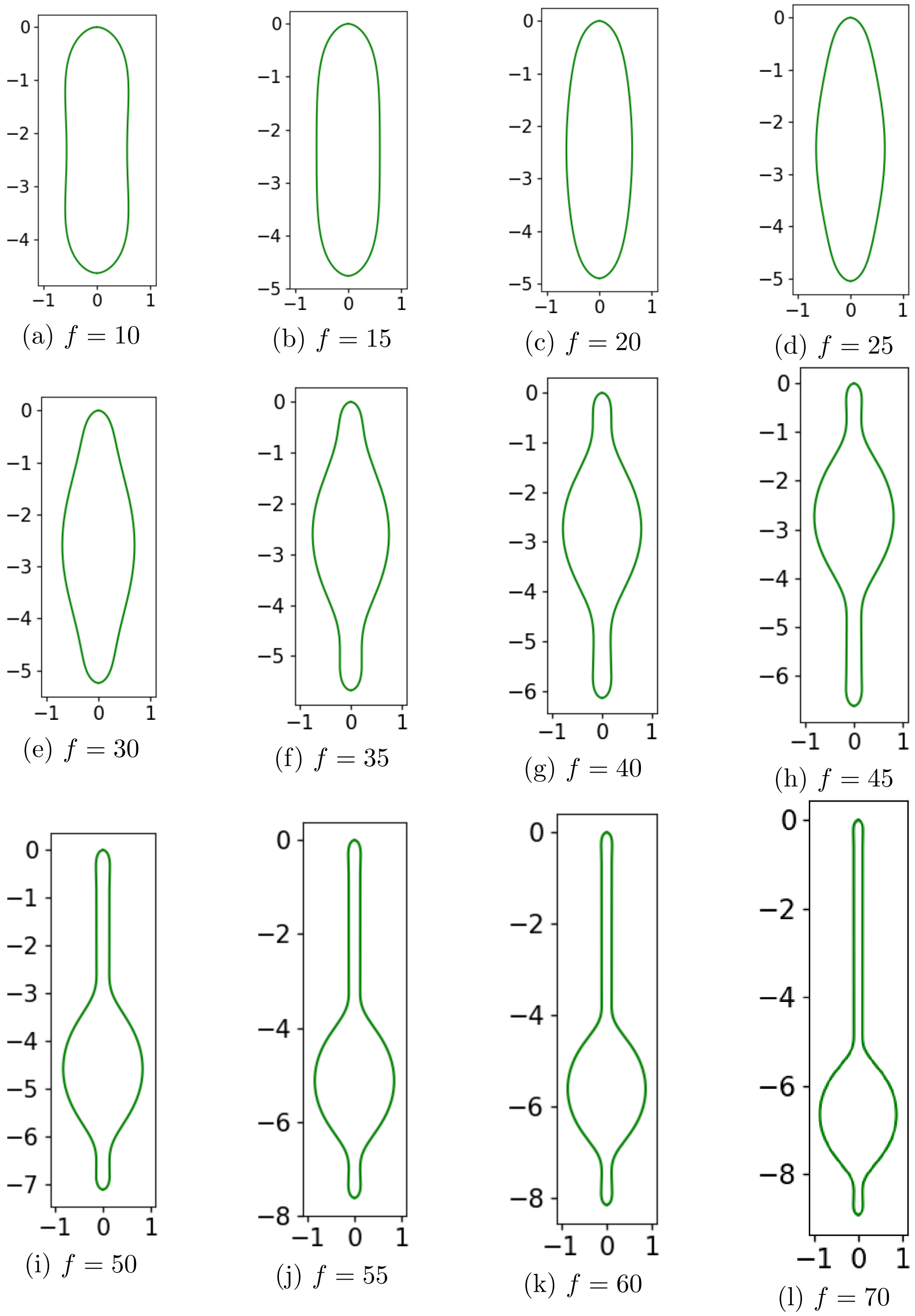

(a) $f = 10$ (b) $f = 15$ (c) $f = 20$ (d) $f = 25$

(e) $f = 30$ (f) $f = 35$ (g) $f = 40$ (h) $f = 45$

(i) $f = 50$ (j) $f = 55$ (k) $f = 60$ (l) $f = 70$

Figure A.8: Shapes obtained from direct minimization for different forces f ($\nu = 0.7$).

$\nu = 0.8$:

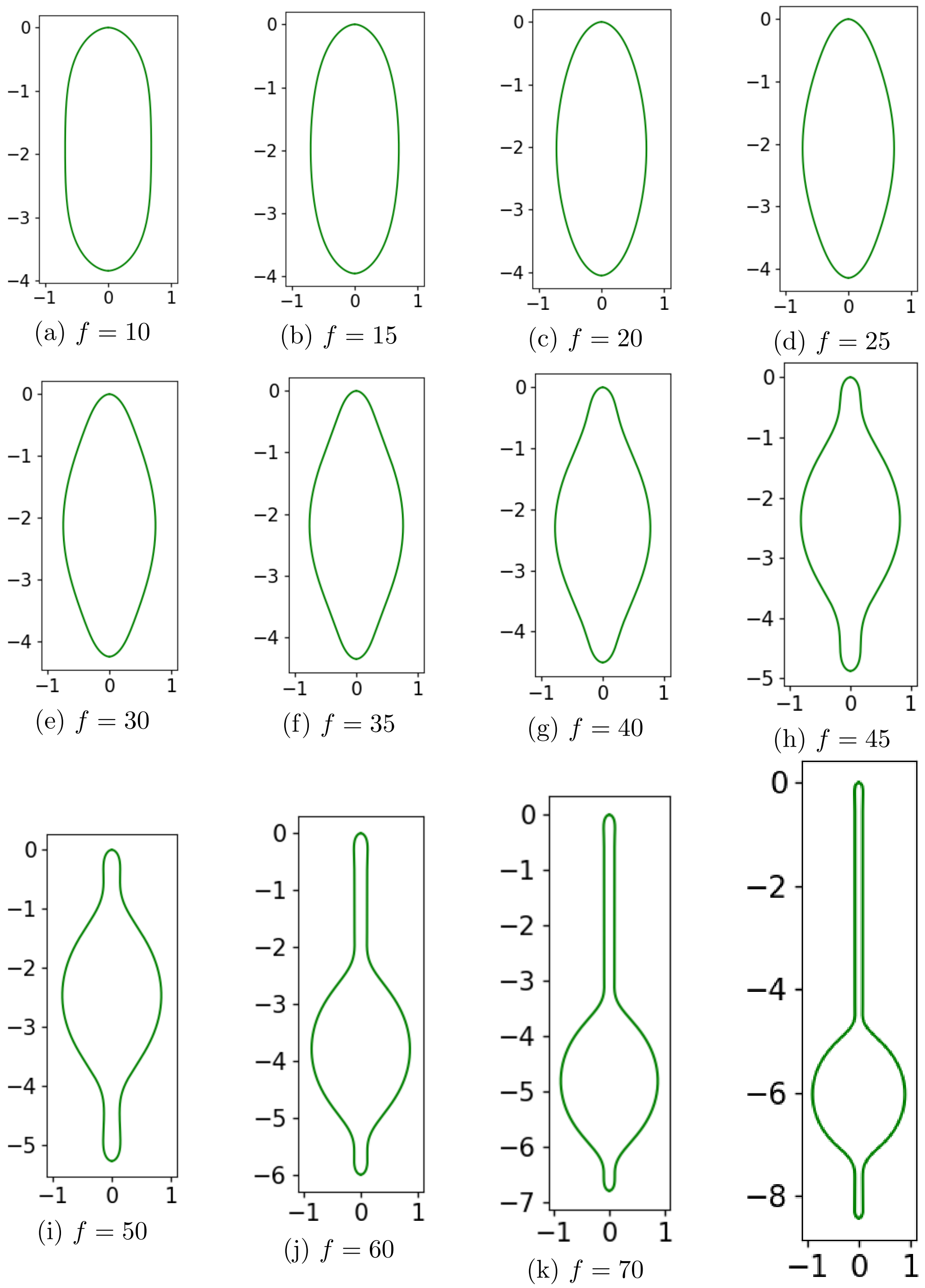

(a) $f = 10$ (b) $f = 15$ (c) $f = 20$ (d) $f = 25$

(e) $f = 30$ (f) $f = 35$ (g) $f = 40$ (h) $f = 45$

(i) $f = 50$ (j) $f = 60$ (k) $f = 70$ (l) $f = 90$

Figure A.9: Shapes obtained from direct minimization for different forces f ($\nu = 0.8$).

B

Derivations and Mathematical Background

B.1 Helfrich Hamiltonian

For calculating the mean and Gaussian curvature of the Helfrich Hamiltonian, methods from differential geometry are used.

A two-dimensional surface embedded in three-dimensional space can be described by by a function $\vec{r}(x_1, x_2)$ with a parameterization of the surface given by x_1 and x_2. For each point on the surface (x_1, x_2) two tangent vectors can be defined:

$$\vec{e_i} \equiv \frac{\partial \vec{r}}{\partial x_i} \qquad \text{for } i = 1, 2 \tag{B.1}$$

The normal vector is then given by:

$$\vec{n} \equiv \frac{\vec{e_1} \times \vec{e_2}}{\|\vec{e_1} \times \vec{e_2}\|} \tag{B.2}$$

The metric tensor that characterizes the local geometry of the surface, the first fundamental form, is now given by:

$$g_{ij} = \vec{e_i} \cdot \vec{e_j} \tag{B.3}$$

From this the area element of the surface can be calculated:

$$\mathrm{d}A = \sqrt{\det g_{ij}}\mathrm{d}x_1\mathrm{d}x_2 \tag{B.4}$$

The curvature tensor, the second fundamental form, is given by:

$$h_{ij} = \frac{\partial^2 \vec{r}}{\partial x_i \partial x_j} \cdot \vec{n} \tag{B.5}$$

The mean and Gaussian curvature are then given by the trace and determinant of the curvature tensor:

$$K = \mathrm{Tr}(h^i_j) = c_1 + c_2 \tag{B.6}$$

$$K_{\mathrm{G}} = \mathrm{Det}(h^i_j) = c_1 c_2 \tag{B.7}$$

where h^i_j is

$$h^i_j = h_{ik} g^{kj} \qquad \text{with} \qquad g^{kj} = (g^{-1})_{kj} \tag{B.8}$$

and c_1 and c_2 its eigenvalues.

As described in the main part of this thesis, we define c_1 and c_2 such that they are positive for a sphere.

B.2 Equilibrium Tube Radius

The equilibrium tube radius R_0 can directly be derived from the Helfrich Hamiltonian given in Equation 3.8. For the following derivation only the tubular part of the vesicle is considered. For a constant area, as it is the case for the system in the final stable configurations, this Hamiltonian simplifies to

$$H = \frac{\kappa}{2}\frac{A}{R^2} \tag{B.9}$$

where R is the radius of the tube. For a tube of length L the tube radius is given by $R = \frac{A}{2\pi L}$. Equation B.9 can therefore be rewritten as

$$H = \frac{2\kappa\pi^2 L^2}{A} \tag{B.10}$$

The external force F_{ext} needed to maintain a tube of stable length L is given by the derivative of equation B.10 with respect to L:

$$\begin{aligned} F_{\text{ext}} &= \frac{\partial H}{\partial L} \\ &= \frac{4\kappa\pi^2 L}{A} = \frac{2\pi\kappa}{R} \end{aligned} \tag{B.11}$$

The equilibrium tube radius is therefore given by:

$$R_0 = \frac{2\pi\kappa}{F_{\text{ext}}} \propto \frac{1}{F_{\text{ext}}} \tag{B.12}$$

B.3 Shape Equations

B.3.1 Mean and Gaussian Curvature

It will be shown that, given the parameterization introduced in Chapter 5.1.1, the mean and Gaussian curvature can be expressed as follows:

$$K = \frac{\sin(\psi)}{x} + \dot{\psi} \tag{B.13}$$

$$K_{\mathrm{G}} = \frac{\dot{\psi}\sin(\psi)}{x} \tag{B.14}$$

For this the derivatives of r with respect to S and ϕ are needed:

$$\frac{\partial r}{\partial S} = \begin{pmatrix} \dot{x}\cos(\phi) \\ \dot{x}\sin(\phi) \\ \dot{z} \end{pmatrix}, \quad \frac{\partial r}{\partial \phi} = \begin{pmatrix} -x\sin(\phi) \\ x\cos(\phi) \\ 0 \end{pmatrix}, \quad \frac{\partial^2 r}{\partial S^2} = \begin{pmatrix} \ddot{x}\cos(\phi) \\ \ddot{x}\sin(\phi) \\ \ddot{z} \end{pmatrix},$$
$$\frac{\partial^2 r}{\partial \phi^2} = \begin{pmatrix} -x\cos(\phi) \\ -x\sin(\phi) \\ 0 \end{pmatrix} \text{ and } \frac{\partial^2 r}{\partial S \partial \phi} = \frac{\partial^2 r}{\partial \phi \partial S} = \begin{pmatrix} -\dot{x}\sin(\phi) \\ \dot{x}\cos(\phi) \\ 0 \end{pmatrix} \tag{B.15}$$

This allows to calculate the unit normal:

$$\vec{n} := \frac{\frac{\partial r}{\partial \phi} \times \frac{\partial r}{\partial S}}{\|\frac{\partial r}{\partial \phi} \times \frac{\partial r}{\partial S}\|} = \begin{pmatrix} \dot{z}\cos(\phi) \\ \dot{z}\sin(\phi) \\ -\dot{x} \end{pmatrix} \tag{B.16}$$

Now the first and second fundamental form I and II can be derived to calculate the Weingarten map L. This is needed to calculate K and K_{G}. In the following $\langle\, ,\, \rangle$ denotes the scalar product.

$$I = \begin{bmatrix} \langle \frac{\partial r}{\partial \phi}, \frac{\partial r}{\partial \phi} \rangle & \langle \frac{\partial r}{\partial \phi}, \frac{\partial r}{\partial S} \rangle \\ \langle \frac{\partial r}{\partial S}, \frac{\partial r}{\partial \phi} \rangle & \langle \frac{\partial r}{\partial S}, \frac{\partial r}{\partial S} \rangle \end{bmatrix} = \begin{bmatrix} x^2 & 0 \\ 0 & 1 \end{bmatrix} \tag{B.17}$$

$$II = \begin{bmatrix} \langle n, \frac{\partial^2 r}{\partial \phi^2} \rangle & \langle n, \frac{\partial^2 r}{\partial \phi \partial S} \rangle \\ \langle n, \frac{\partial^2 r}{\partial S \partial \phi} \rangle & \langle n, \frac{\partial^2 r}{\partial S^2} \rangle \end{bmatrix} = \begin{bmatrix} x\sin\psi & 0 \\ 0 & \dot{\psi} \end{bmatrix} \tag{B.18}$$

From this the following Weingarten-map can be determined:

$$L = (I)^{-1}(II) = \begin{bmatrix} \frac{\sin\psi}{x} & 0 \\ 0 & \dot{\psi} \end{bmatrix} \tag{B.19}$$

Finally this allows to calculate K and K_{G}:

$$K = \mathrm{Tr}(L) = \frac{\sin\psi}{x} + \dot{\psi}, \qquad K_{\mathrm{G}} = \mathrm{Det}(L) = \frac{\sin\psi}{x}\dot{\psi} \tag{B.20}$$

The differential $\mathrm{d}A$ is given by:

$$\mathrm{d}A = \sqrt{g}\mathrm{d}\phi dS = x\mathrm{d}\phi\mathrm{d}S \tag{B.21}$$

with Gram's determinant $g = \|\frac{\partial r}{\partial \phi} \times \frac{\partial r}{\partial S}\|^2$.

B.3.2 Gauss-Bonnet Theorem

Integrating over the Gaussian curvature on a closed surface gives a constant contribution according to the Gauss-Bonnet theorem.[102] In our case one obtains the following value:

$$\oint K_{\mathrm{G}}\mathrm{d}A = \int_0^{2\pi} \mathrm{d}\phi \int_{S_0}^{S_1} \mathrm{d}Sx\frac{\dot{\psi}\sin\psi}{x} = 2\pi\int_{S_0}^{S_1} \dot{\psi}\sin\psi\mathrm{d}S = 2\pi[-\cos(\psi(S))]_{S_0}^{S_1} = 4\pi \tag{B.22}$$

Since one is typically only interested in energy differences and not in absolute values, this constant contribution can therefore be neglected.

B.3.3 Derivation of the Shape Equations

This calculation has been performed previously in e.g. Refs. 143; 151 without the additional term $-\bar{f}\sin\psi$ and the results including an external force are reported in Ref. 138. This derivation will be repeated including the contribution from the external force, to show, how these equations can be obtained and expressed in our representation.

In order to derive the shape equations the following function has to be minimized:

$$F = 2\pi\kappa\int_{S_0}^{S_1} LdS \tag{B.23}$$

with

$$L = \frac{x}{2}\left(\frac{\sin\psi}{x} + \dot{\psi} - K_0\right)^2 + \bar{\Sigma}x + \frac{\bar{P}}{2}x^2\sin\psi + \gamma(\dot{x} - \cos\psi) + \eta(\dot{z} + \sin\psi) - \bar{f}\sin\psi \tag{B.24}$$

The variation of F thus yields:

$$\begin{aligned}\delta F = \int_{S_0}^{S_1} \Bigg[&\left(\delta\psi\frac{\partial L}{\partial\psi} + \delta\dot{\psi}\frac{\partial L}{\partial\dot{\psi}}\right) + \left(\delta x\frac{\partial L}{\partial x} + \delta\dot{x}\frac{\partial L}{\partial\dot{x}}\right) + \left(\delta z\frac{\partial L}{\partial z} + \delta\dot{z}\frac{\partial L}{\partial\dot{z}}\right) \\ &+ \left(\delta\gamma\frac{\partial L}{\partial\gamma} + \delta\dot{\gamma}\frac{\partial L}{\partial\dot{\gamma}}\right) + \left(\delta\eta\frac{\partial L}{\partial\eta} + \delta\dot{\eta}\frac{\partial L}{\partial\dot{\eta}}\right)\Bigg]\mathrm{d}S\end{aligned} \tag{B.25}$$

Using integration by parts and noting that $\frac{\partial L}{\partial \dot\gamma} = \frac{\partial L}{\partial \dot\eta} = 0$ this leads to

$$\begin{aligned}\delta F = \int_{S_0}^{S_1} \Bigg[&\left(\frac{\partial L}{\partial \psi} - \frac{\mathrm{d}}{\mathrm{d}S}\frac{\partial L}{\partial \dot\psi}\right)\delta\psi + \left(\frac{\partial L}{\partial x} - \frac{\mathrm{d}}{\mathrm{d}S}\frac{\partial L}{\partial \dot x}\right)\delta x + \left(\frac{\partial L}{\partial z} - \frac{\mathrm{d}}{\mathrm{d}S}\frac{\partial L}{\partial \dot z}\right)\delta z \\ &+ \delta\gamma\frac{\partial L}{\partial \gamma} + \delta\eta\frac{\partial L}{\partial \eta}\Bigg]\mathrm{d}S \\ &- \left[\mathcal{H}\delta S\right]_{S_0}^{S_1} + \left[\delta\psi\frac{\partial L}{\partial \dot\psi}\right]_{S_0}^{S_1} + \left[\delta x\frac{\partial L}{\partial \dot x}\right]_{S_0}^{S_1} + \left[\delta z\frac{\partial L}{\partial \dot z}\right]_{S_0}^{S_1} = 0\end{aligned} \tag{B.26}$$

with

$$\mathcal{H} := -L + \dot\psi\frac{\partial L}{\partial \dot\psi} + \dot x\frac{\partial L}{\partial \dot x} + \dot z\frac{\partial L}{\partial \dot z} \tag{B.27}$$

For this relation to hold, the following conditions given in the integral in equation B.26 need to be fulfilled.

$$\frac{\partial L}{\partial \psi} - \frac{\mathrm{d}}{\mathrm{d}S}\frac{\partial L}{\partial \dot\psi} = 0, \quad \frac{\partial L}{\partial x} - \frac{\mathrm{d}}{\mathrm{d}S}\frac{\partial L}{\partial \dot x} = 0, \quad \frac{\partial L}{\partial z} - \frac{\mathrm{d}}{\mathrm{d}S}\frac{\partial L}{\partial \dot z} = 0, \quad \frac{\partial L}{\partial \gamma} = 0, \quad \frac{\partial L}{\partial \eta} = 0 \tag{B.28}$$

Solving these equations, one obtains the shape equations. From the boundary conditions in equation B.26, one then obtains additional constraints.

Looking at the first equation in B.28 one obtains:

$$\frac{\partial L}{\partial \psi} = x\left(\frac{\sin\psi}{x} + \dot\psi - K_0\right)\frac{\cos\psi}{x} + \frac{\bar P}{2}x^2\cos\psi + \gamma\sin\psi + \eta\cos\psi - \bar f\cos\psi \tag{B.29}$$

$$\frac{\partial L}{\partial \dot\psi} = x\left(\frac{\sin\psi}{x} + \dot\psi - K_0\right) \tag{B.30}$$

$$\frac{\mathrm{d}}{\mathrm{d}S}\frac{\partial L}{\partial \dot\psi} = \dot x\left(\frac{\sin\psi}{x} + \dot\psi - K_0\right) + x\left(\frac{\dot\psi\cos\psi}{x} - \frac{\dot x\sin\psi}{x^2} + \ddot\psi\right) \tag{B.31}$$

Equating these relations one obtains the first shape equation:

$$x\ddot\psi = \frac{\sin\psi\cos\psi}{x} + \frac{\bar P x^2}{2}\cos\psi + \gamma\sin\psi + \eta\cos\psi - \dot\psi\cos\psi - \bar f\cos\psi \tag{B.32}$$

From the second equation in B.28 one obtains:

$$\frac{\partial L}{\partial x} = \frac{1}{2}\left(\frac{\sin\psi}{x} + \dot\psi - K_0\right)^2 - \frac{\sin\psi}{x}\left(\frac{\sin\psi}{x} + \dot\psi - K_0\right) + \bar\Sigma + \bar P x\sin\psi \tag{B.33}$$

$$\frac{\partial L}{\partial \dot x} = \gamma \tag{B.34}$$

$$\frac{\mathrm{d}}{\mathrm{d}S}\frac{\partial L}{\partial \dot x} = \dot\gamma \tag{B.35}$$

Which leads to the second shape equation:

$$\dot{\gamma} = \frac{1}{2}(\dot{\psi} - K_0)^2 - \frac{\sin^2\psi}{2x^2} + \bar{\Sigma} + \bar{P}x\sin\psi \tag{B.36}$$

From the third equation in B.28 one obtains:

$$\frac{\partial L}{\partial z} = 0 \tag{B.37}$$

$$\frac{\partial L}{\partial \dot{z}} = \eta \tag{B.38}$$

$$\frac{\mathrm{d}}{\mathrm{d}S}\frac{\partial L}{\partial \dot{z}} = \dot{\eta} \tag{B.39}$$

Which leads to

$$\dot{\eta} = 0 \tag{B.40}$$

The fourth and fifth equation in B.28 directly lead to the last two shape equations:

$$\frac{\partial L}{\partial \gamma} = \dot{x} - \cos\psi = 0 \tag{B.41}$$

$$\frac{\partial L}{\partial \eta} = \dot{z} + \sin\psi = 0 \tag{B.42}$$

From the boundary terms in equation B.26 one obtains additional constraints and boundary conditions. For a closed vesicle with spherical topology we require $x(0) = x(S_1) = 0$ and $\psi(0) = 0, \psi(S_1) = \pi$. The second and third boundary term thus directly vanish.

For the fourth boundary term to vanish, we require

$$\frac{\partial L}{\dot{z}} = \eta = 0 \tag{B.43}$$

and for the first boundary term to vanish, we require that $\mathcal{H}(0) = \mathcal{H}(S_1) = 0$ and therefore $\gamma(0) = \gamma(S_1) = 0$.

Taking all these considerations into account one obtains the shape equations given in Equations 5.18 - 5.24.

B.4 Correction to the Tube Length

To determine how good a thin tube can be approximated by a triangular mesh structure, as it is used in the simulations, one can perform a simple geometric analysis. This will also allow to calculate a correction for the tube length, for thin radii.

Let us consider the cross section of a tube as illustrated in Figure B.1. For an ideal tube this would be a perfect circle. Approximated by a triangular mesh, this cross section would (roughly) be a regular polygon with n edges, depending on the radius R of the tube. c is the chord length of a circular segment, s the arc length and α the central angle of the circular sector.

Let us now assume that the perfect tube and the tube approximated by the mesh have the same area A. Then we can say that:

$$A = \text{const.} = L_{\bigcirc} U_{\bigcirc} = L_{\pentagon} U_{\pentagon} \tag{B.44}$$

where L is the tube length, U the circumference of the cross section and $\bigcirc$ and $\pentagon$ stand for the ideal tube and the approximated tube respectively.

This means that the length of the polygon tube is given by:

$$L_{\pentagon} = L_{\bigcirc} \frac{U_{\bigcirc}}{U_{\pentagon}} = L_{\bigcirc} \frac{ns}{nc} \approx L_{\bigcirc} s \tag{B.45}$$

where the chord length is the average bond length in the simulations, which is $a \approx 1$. The arc length is given by $s = R\alpha$ and the angle α can be determined using simple trigonometric relations. This leads to:

$$L_{\pentagon} \approx L_{\bigcirc} R\alpha = L_{\bigcirc} 2R \arcsin\left(\frac{1}{2R}\right) \tag{B.46}$$

This way, one obtains a correction term for the tube length depending on the radius. For a tube of radius $R = 2$ this correction is $\approx 1\%$, so quite small. However, for a thin tube with radius $R = 1$ it is already $\approx 5\%$.

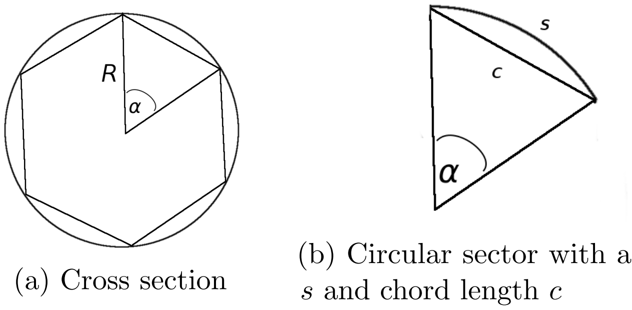

(a) Cross section

(b) Circular sector with arc length s and chord length c

Figure B.1: Cross section of a tube, approximated by a polygon.

C

Simulation of the Vesicle Movement

A simple model was devised to investigate vesicle motion induced by tubule generation. This model has been created to investigate a potential correlation between stromules and chloroplast movement.[48] Different chloroplast movement patterns have also been observed in mutant plants, where a chloroplast anchoring protein was targeted.[175;176] With our simple model we can mimic these movement patterns which could help to find and characterize the underlying mechanisms and thus improve our current understanding of stromule formation and function.

The model consists of a small vesicle confined within a larger sphere. Tubes extending from the vesicle to the outer sphere exert a force on the vesicle and thus induce motion. The anchoring points of the tubes are randomly created on the small vesicle's surface and annihilated with a certain rate. This enables us to investigate the vesicle mobility depending on the average number of tubes and the creation rate.

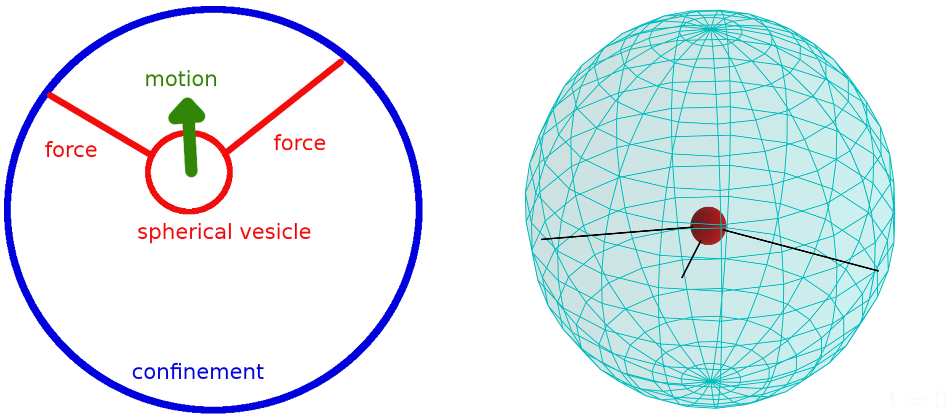

(a) Illustration of the model.

(b) 3D snapshot of a simulation.

Figure C.1: A small vesicle is confined within a big sphere to investigate vesicle movement. Tubes protruding from the vesicle exert a force.

C.1 Trajectories

The vesicle movement is modeled using overdamped Brownian motion:

$$\vec{x}_{n+1} = \vec{x}_n + \Delta t \vec{v}_{n+1} \tag{C.1}$$

$$\vec{v}_{n+1} = \mu \sum \vec{F}_{\text{ext}} + \sqrt{24\mu k_{\text{B}} T \frac{1}{\Delta t}} R(t) \tag{C.2}$$

where $\vec{x}_n$ is the position and $\vec{v}_n$ the velocity of the small vesicle at step n. The timestep is Δt and and the mobility $\mu = \frac{1}{6\pi\eta r_{\text{in}}}$. k_{B} is the Boltzmann constant, T the temperature of the system and $R(t)$ uniformly distributed random numbers between -0.5 and 0.5. $\vec{F}_{\text{ext}}$ is the external force exerted by the tubes. In our simulations we have set $k_{\text{B}}T = 1$ (which defines the unit of energy), the radius of the small vesicle to $r_{\text{in}} = 1$ (which sets the unit of length) and the shear viscosity $\eta = 1$ (which indirectly sets the unit of time). In these units we have chosen $\Delta t = 0.001$, the radius of the outer sphere $r_{\text{out}} = 10$ and the deletion/creation rate 10^{-2}. The average number of tubes N_{T} will be varied in the following analysis.

The model is illustrated in Figure C.1, in which a small vesicle (red) is confined by a larger sphere (blue). The tubes protruding from the vesicle exert a force, $\vec{F}_{\text{ext}}$, and pull it towards the boundary marked by the outer sphere. Figure C.1b shows an exemplary snapshot of a simulation run with three tubes attached to the vesicle. To illustrate the motion of the vesicle a projection of the particle trajectory onto a plane can be found in Figure C.2. One can clearly observe two different scales on which the motion takes place. Short clustered motion due to thermal fluctuations and directed motions on larger scales induced by the external pulling of the tubes.

Our model is reminiscent of a continuous-time random walk (CTRW),[177] in which the motion of a particle is described by a stochastic jump process, characterized by distributions for the jump lengths and the waiting times between individual jumps. Clearly our model is not equivalent to the CTRW because, first, we have the diffusive-like motion during the individual jumps, and second, the motion of the vesicle is confined by the large sphere which serves as the anchoring agent. Nevertheless in the following we will characterize the dynamics of our model using waiting time, jump length and jump angle distributions.

C.2 Characterizing the Stochastic Jump Process

When simulating the vesicle with different parameters, e.g. average number of tubes N_{T}, amplitude of the force $|\vec{F}_{\text{ext}}|$ or creation rate, one could observe different behaviors of the trajectories. We therefore started investigating the step length distribution of different trajectories. For this we first smoothed the trajectories

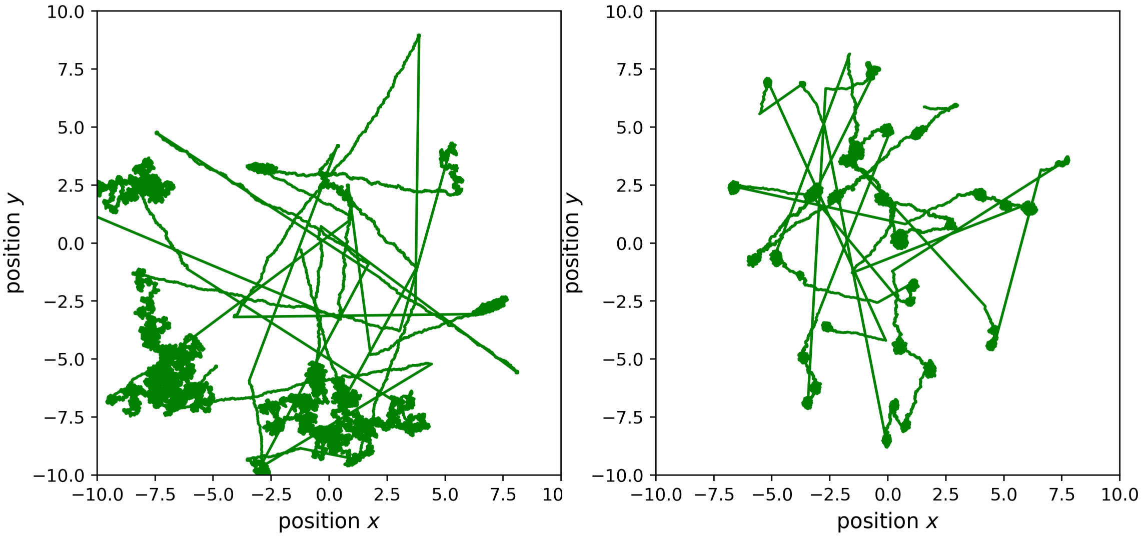

(a) $N_\mathrm{T} = 1$ (b) $N_\mathrm{T} = 6$

Figure C.2: Projection of the vesicle trajectory onto a plane.

using the Ramer Douglas Peucker algorithm[178;179] to identify individual jumps. We then calculate the length of the jumps, the angle between two subsequent jumps and the waiting time between the jumps.

A histogram of an exemplary jump length distribution can be found in Figure C.3. One can observe a clear correlation between the number of tubes and the occurrence of long individual jumps. We find that the smaller the average number of tubes connected to the vesicle is, the more pronounced is the tail of the jump length distribution. This is to be expected, because more tubes means that the creation of an additional tube becomes less significant and thus induces less pronounced jumps.

Different from the idealized CTRW our model shows a pronounced correlation between individual jumps, which is visible in the probability distribution for the angle between two subsequent jumps (see Figure C.4). This distribution is clearly not flat, but shows a pronounced maximum at angles around 60°. Furthermore, one can observe a second local maximum at large angles $> 160°$. The latter strongly depends on the average number of tubes connecting to the vesicle making it an ideal measure to fit the parameter N_T to experimental observations.

The waiting time distribution, shown in Figure C.5, appears to be largely independent of the average numbers of tubes N_T and exponential for long times, corresponding to the Poisson process that was used as input for the creation and annihilation process. This is important, because it shows that our data analysis is indeed able to properly extract the jump process. Only for small times, we observe a deviation from the exponential, which clearly originates from the smoothing algorithm. The waiting time distribution is therefore ideal to extract properties of tube formation and annihilation from experiments, e.g. the rates connected to these processes.

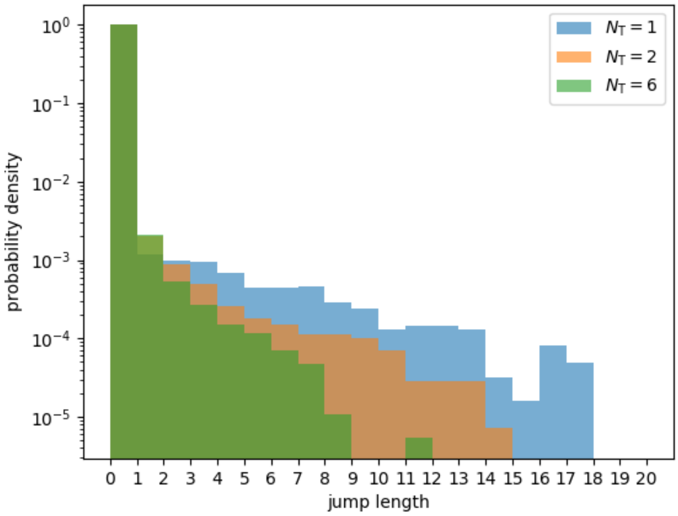

Figure C.3: Histogram of the jump length distribution for different average numbers of tubes N_{T}.

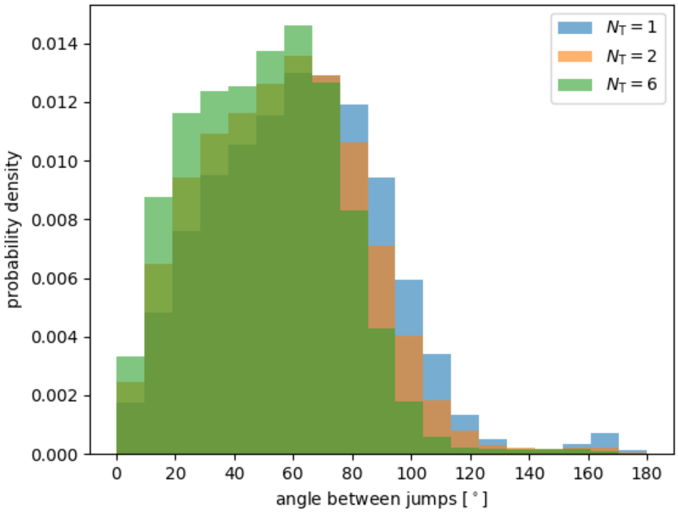

Figure C.4: Histogram of the angle between subsequent jumps for different average numbers of tubes N_{T}.

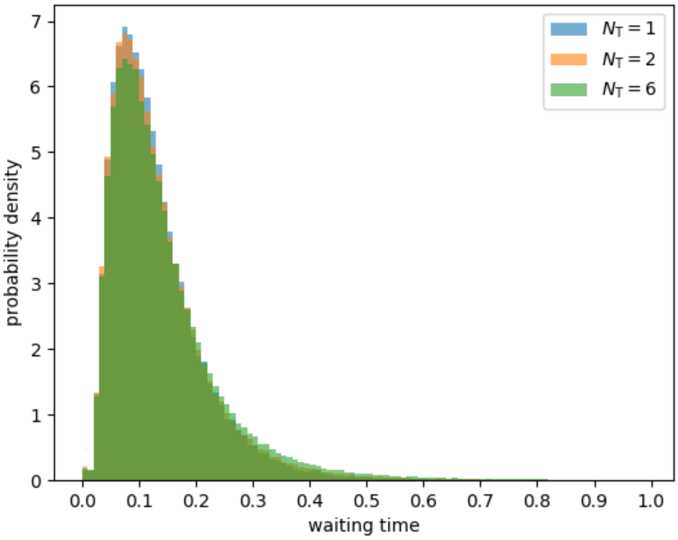

Figure C.5: Histogram of the waiting time between jumps for different average numbers of tubes N_T.

The data discussed above is preliminary and will clearly benefit from better statistics, however, we believe that our model is a powerful tool to investigate dynamic properties of tube/stromule formation in cells by analysis of the anomalous diffusion of individual vesicles and comparisons between our model and experimental measurements.

D

Source Code for the Direct Minimization

This is the source code used for the direct minimization method presented in Section 5.3. For this the software package ACADO toolkit was used.[161;162] More information and useful examples can be found under `http://www.acadotoolkit.org/`.

The input files 'x.txt', 'u.txt' and 'p.txt' contain initial guesses about the configuration. 'x.txt' contains the coordinates, but it can be empty for the first run. It can be useful to load a configuration, when going to a finer discretization. 'u.txt' contains the initial guess for u, which can simply be set to one and 'p.txt' can roughly be set to π. These initial guesses can of course be varied and should be adapted to fit the respective problem.

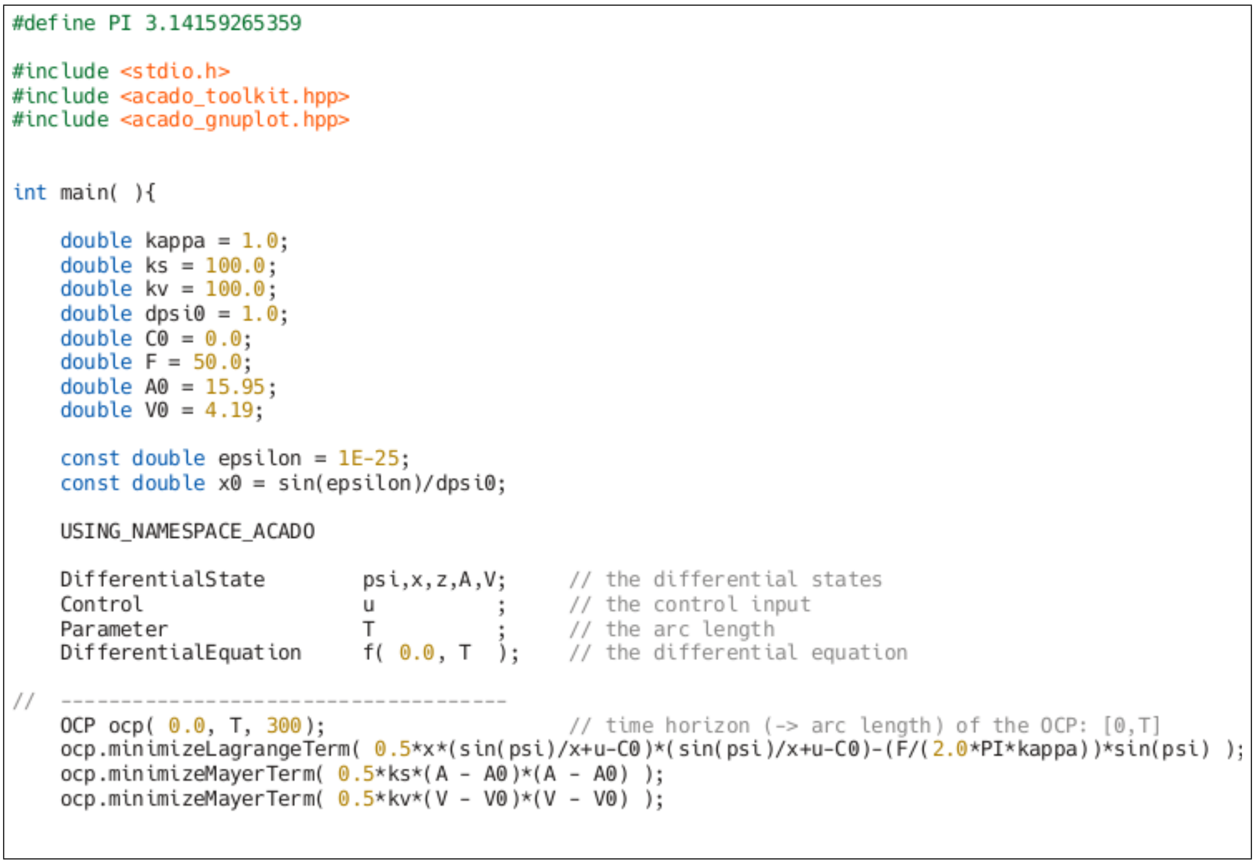

```
#define PI 3.14159265359

#include <stdio.h>
#include <acado_toolkit.hpp>
#include <acado_gnuplot.hpp>


int main( ){

    double kappa = 1.0;
    double ks = 100.0;
    double kv = 100.0;
    double dpsi0 = 1.0;
    double C0 = 0.0;
    double F = 50.0;
    double A0 = 15.95;
    double V0 = 4.19;

    const double epsilon = 1E-25;
    const double x0 = sin(epsilon)/dpsi0;

    USING_NAMESPACE_ACADO

    DifferentialState        psi,x,z,A,V;     // the differential states
    Control                  u          ;     // the control input
    Parameter                T          ;     // the arc length
    DifferentialEquation     f( 0.0, T  );    // the differential equation

//  -------------------------------------
    OCP ocp( 0.0, T, 300);                    // time horizon (-> arc length) of the OCP: [0,T]
    ocp.minimizeLagrangeTerm( 0.5*x*(sin(psi)/x+u-C0)*(sin(psi)/x+u-C0)-(F/(2.0*PI*kappa))*sin(psi) );
    ocp.minimizeMayerTerm( 0.5*ks*(A - A0)*(A - A0) );
    ocp.minimizeMayerTerm( 0.5*kv*(V - V0)*(V - V0) );
```

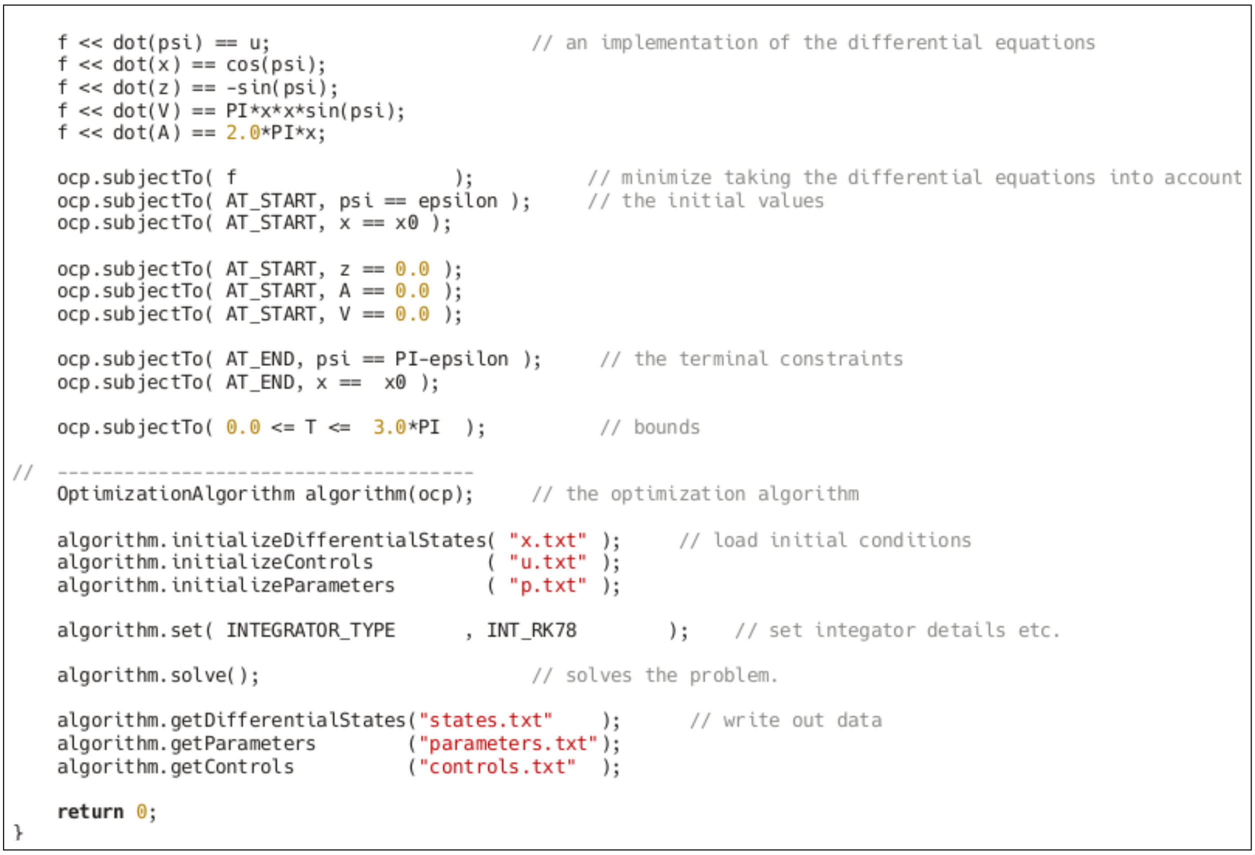

```
    f << dot(psi) == u;                       // an implementation of the differential equations
    f << dot(x) == cos(psi);
    f << dot(z) == -sin(psi);
    f << dot(V) == PI*x*x*sin(psi);
    f << dot(A) == 2.0*PI*x;

    ocp.subjectTo( f                   );          // minimize taking the differential equations into account
    ocp.subjectTo( AT_START, psi == epsilon );     // the initial values
    ocp.subjectTo( AT_START, x == x0 );

    ocp.subjectTo( AT_START, z == 0.0 );
    ocp.subjectTo( AT_START, A == 0.0 );
    ocp.subjectTo( AT_START, V == 0.0 );

    ocp.subjectTo( AT_END, psi == PI-epsilon );     // the terminal constraints
    ocp.subjectTo( AT_END, x ==  x0 );

    ocp.subjectTo( 0.0 <= T <=  3.0*PI  );          // bounds

//  -------------------------------------
    OptimizationAlgorithm algorithm(ocp);     // the optimization algorithm

    algorithm.initializeDifferentialStates( "x.txt" );      // load initial conditions
    algorithm.initializeControls          ( "u.txt" );
    algorithm.initializeParameters        ( "p.txt" );

    algorithm.set( INTEGRATOR_TYPE      , INT_RK78        );    // set integrator details etc.

    algorithm.solve();                        // solves the problem.

    algorithm.getDifferentialStates("states.txt"    );      // write out data
    algorithm.getParameters        ("parameters.txt");
    algorithm.getControls          ("controls.txt"  );

    return 0;
}
```

Figure D.1: Source code used for the direct minimization method.

Bibliography

[1] Enkavi, G.; Javanainen, M.; Kulig, W.; Róg, T.; Vattulainen, I. Multiscale Simulations of Biological Membranes: The Challenge To Understand Biological Phenomena in a Living Substance. *Chemical Reviews* **2019**, *119*.

[2] Structure of a typical plant cell. `https://en.wikipedia.org/wiki/Cell_(biology)#/media/File:Plant_cell_structure-en.svg`, Accessed: 2020-07-06.

[3] Alberts, B.; Bray, D.; Lewis, J.; Raff, M.; Roberts, K.; Watson, J. *Molecular biology of the cell*, 5th ed.; Garland Science: New York, 2008.

[4] Lipid bilayer. `https://en.wikipedia.org/wiki/Cell_membrane#/media/File:Cell_membrane_detailed_diagram_4.svg`, Accessed: 2020-07-13.

[5] Upadhyaya, A.; Sheetz, M. Tension in Tubulovesicular Networks of Golgi and Endoplasmic Reticulum Membranes. *Biophysical journal* **2004**, *86*, 2923–8.

[6] Shibata, Y.; Hu, J.; Kozlov, M. M.; Rapoport, T. A. Mechanisms Shaping the Membranes of Cellular Organelles. *Annual Review of Cell and Developmental Biology* **2009**, *25*, 329–354.

[7] Mollenhauer, H.; Morre, D. The tubular network of the Golgi apparatus. *Histochemistry and Cell Biology* **1998**, *109*, 533–543.

[8] Lü, L.; Niu, L.; Hu, J. "At last in" the physiological roles of the tubular ER network. *Biophysics Reports* **2020**, *6*.

[9] Aloupis, G.; Langerman, S.; Soss, M.; Toussaint, G. Algorithms for bivariate medians and a Fermat–Torricelli problem for lines. *Computational Geometry* **2003**, *26*, 69 – 79, The Thirteenth Canadian Conference on Computational Geometry - CCCG'01.

[10] Lobovkina, T.; Dommersnes, P.; Joanny, J. F.; Bassereau, P.; Karlsson, M.; Orwar, O. Mechanical tweezer action by self-tightening knots in surfactant nanotubes. *Proceedings of the National Academy of Sciences of the United States of America* **2004**, *101 21*, 7949–53.

[11] Lobovkina, T.; Dommersnes, P.; Joanny, J.-F. m. c.; Hurtig, J.; Orwar, O. Zipper Dynamics of Surfactant Nanotube Y Junctions. *Phys. Rev. Lett.* **2006**, *97*, 188105.

[12] Karlsson, M.; Sott, K.; Davidson, M.; Cans, A.-S.; Linderholm, P.; Chiu, D.; Orwar, O. Formation of geometrically complex lipid nanotube-vesicle networks of higher-order topologies. *Proceedings of the National Academy of Sciences* **2002**, *99*, 11573–11578.

[13] Lobovkina, T.; Dommersnes, P.; Tiourine, S.; Joanny, J.; Orwar, O. Shape optimization in lipid nanotube networks. *The European physical journal. E, Soft matter* **2008**, *26*, 295–300.

[14] Aubert, J. H.; Kraynik, A. M.; Rand, P. B. Aqueous Foams. *Scientific American* **1986**, *254*, 74–83.

[15] Roux, A. The physics of membrane tubes: soft templates for studying cellular membranes. *Soft Matter* **2013**, *9*, 6726–6736.

[16] Tsafrir, I.; Caspi, Y.; Guedeau-Boudeville, M.-A.; Arzi, T.; Stavans, J. Budding and Tubulation in Highly Oblate Vesicles by Anchored Amphiphilic Molecules. *Phys. Rev. Lett.* **2003**, *91*, 138102.

[17] Campelo, F.; McMahon, H. T.; Kozlov, M. M. The Hydrophobic Insertion Mechanism of Membrane Curvature Generation by Proteins. *Biophysical Journal* **2008**, *95*, 2325 – 2339.

[18] Frost, A.; Unger, V. M.; De Camilli, P. The BAR Domain Superfamily: Membrane-Molding Macromolecules. *Cell* **2009**, *137*, 191 – 196.

[19] Voeltz, G. K.; Prinz, W. A.; Shibata, Y.; Rist, J. M.; Rapoport, T. A. A Class of Membrane Proteins Shaping the Tubular Endoplasmic Reticulum. *Cell* **2006**, *124*, 573 – 586.

[20] Hu, J.; Shibata, Y.; Voss, C.; Shemesh, T.; Li, Z.; Coughlin, M.; Kozlov, M. M.; Rapoport, T. A.; Prinz, W. A. Membrane Proteins of the Endoplasmic Reticulum Induce High-Curvature Tubules. *Science* **2008**, *319*, 1247–1250.

[21] Footer, M. J.; Kerssemakers, J. W. J.; Theriot, J. A.; Dogterom, M. Direct measurement of force generation by actin filament polymerization using an optical trap. *Proceedings of the National Academy of Sciences* **2007**, *104*, 2181–2186.

[22] Roux, A.; Koster, G.; Lenz, M.; Sorre, B.; Manneville, J.-B.; Nassoy, P.; Bassereau, P. Membrane curvature controls dynamin polymerization. *Proceedings of the National Academy of Sciences* **2010**, *107*, 4141–4146.

[23] Miyata, H.; Hotani, H. Morphological changes in liposomes caused by polymerization of encapsulated actin and spontaneous formation of actin bundles. *Proceedings of the National Academy of Sciences* **1992**, *89*, 11547–11551.

[24] Miyata, H.; Nishiyama, S.; Akashi, K.-i.; Kinosita, K. Protrusive growth from giant liposomes driven by actin polymerization. *Proceedings of the National Academy of Sciences* **1999**, *96*, 2048–2053.

[25] Derényi, I.; Jülicher, F.; Prost, J. Formation and Interaction of Membrane Tubes. *Phys. Rev. Lett.* **2002**, *88*, 238101.

[26] Koster, G.; VanDuijn, M.; Hofs, B.; Dogterom, M. Membrane tube formation from giant vesicles by dynamic association of motor proteins. *Proceedings of the National Academy of Sciences* **2003**, *100*, 15583–15588.

[27] Leduc, C.; Campàs, O.; Zeldovich, K. B.; Roux, A.; Jolimaitre, P.; Bourel-Bonnet, L.; Goud, B.; Joanny, J.-F.; Bassereau, P.; Prost, J. Cooperative extraction of membrane nanotubes by molecular motors. *Proceedings of the National Academy of Sciences* **2004**, *101*, 17096–17101.

[28] Campàs, O.; Leduc, C.; Bassereau, P.; Casademunt, J.; Joanny, J.-F.; Prost, J. Coordination of Kinesin Motors Pulling on Fluid Membranes. *Biophysical Journal* **2008**, *94*, 5009 – 5017.

[29] Du, W. et al. Kinesin 1 Drives Autolysosome Tubulation. *Developmental Cell* **2016**, *37*, 326 – 336.

[30] Saraste, J.; Prydz, K. A New Look at the Functional Organization of the Golgi Ribbon. *Frontiers in Cell and Developmental Biology* **2019**, *7*, 171.

[31] Sowinski, S.; Jolly, C.; Berninghausen, O.; Purbhoo, M.; Chauveau, A.; Köhler, K.; Oddos, S.; Eissmann, P.; Brodsky, F.; Hopkins, C.; Önfelt, B.; Sattentau, Q.; Davis, D. Membrane nanotubes physically connect T cells over long distances presenting a novel route for HIV-1 transmission. *Nature Cell Biology* **2008**, *10*, 211–219.

[32] Gözen, I.; Jesorka, A. Lipid nanotube networks: Biomimetic Cell-to-Cell Communication and Soft-Matter Technology. *Nanofabrication* **08 May. 2015**,

[33] Köhler, R.; Hanson, M. Plastid tubules of higher plants are tissue-specific and developmentally regulated. *Journal of cell science* **2000**, *113 (Pt 1)*, 81–9.

[34] Pyke, K.; Howells, C. Plastid and Stromule Morphogenesis in Tomato. *Annals of botany* **2002**, *90*, 559–66.

[35] Kwok, E. Y.; Hanson, M. R. Microfilaments and microtubules control the morphology and movement of non-green plastids and stromules in Nicotiana tabacum. *The Plant Journal* **2003**, *35*, 16–26.

[36] Kwok, E.; Hanson, M. In vivo analysis of interactions between GFP-labeled microfilaments and plastid stromules. *BMC plant biology* **2004**, *4*, 2.

[37] Kwok, E. Y.; Hanson, M. R. GFP-labelled Rubisco and aspartate aminotransferase are present in plastid stromules and traffic between plastids. *Journal of Experimental Botany* **2004**, *55*, 595–604.

[38] Waters, M. T.; Fray, R. G.; Pyke, K. A. Stromule formation is dependent upon plastid size, plastid differentiation status and the density of plastids within the cell. *The Plant Journal* **2004**, *39*, 655–667.

[39] Natesan, S. K. A.; Sullivan, J. A.; Gray, J. C. Stromules: a characteristic cell-specific feature of plastid morphology. *Journal of Experimental Botany* **2005**, *56*, 787–797.

[40] Holzinger, A.; Buchner, O.; Lütz, C.; Hanson, M. Temperature-sensitive formation of chloroplast protrusions and stromules in mesophyll cells of Arabidopsis thaliana. *Protoplasma* **2007**, *230*, 23–30.

[41] Schattat, M.; Barton, K.; Baudisch, B.; Klösgen, R. B.; Mathur, J. Plastid Stromule Branching Coincides with Contiguous Endoplasmic Reticulum Dynamics. *Plant Physiology* **2011**, *155*, 1667–1677.

[42] Hanson, M. R.; Sattarzadeh, A. Stromules: Recent Insights into a Long Neglected Feature of Plastid Morphology and Function. *Plant Physiology* **2011**, *155*, 1486–1492.

[43] Osteryoung, K. W.; Pyke, K. A. Division and Dynamic Morphology of Plastids. *Annual Review of Plant Biology* **2014**, *65*, 443–472.

[44] Caplan, J.; Kumar, A.; Park, E.; Padmanabhan, M.; Hoban, K.; Modla, S.; Czymmek, K.; Dinesh-Kumar, S. Chloroplast Stromules Function during Innate Immunity. *Developmental cell* **2015**, *34*.

[45] Brunkard, J. O.; Runkel, A. M.; Zambryski, P. C. Chloroplasts extend stromules independently and in response to internal redox signals. *Proceedings of the National Academy of Sciences* **2015**, *112*, 10044–10049.

[46] Ho, J.; Theg, S. M. The Formation of Stromules In Vitro from Chloroplasts Isolated from Nicotiana benthamiana. *PLOS ONE* **2016**, *11*, 1–14.

[47] Erickson, J. L.; Kantek, M.; Schattat, M. H. Plastid-Nucleus Distance Alters the Behavior of Stromules. *Frontiers in Plant Science* **2017**, *8*, 1135.

[48] Kumar, A. S.; Park, E.; Nedo, A.; Alqarni, A.; Ren, L.; Hoban, K.; Modla, S.; McDonald, J. H.; Kambhamettu, C.; Dinesh-Kumar, S. P.; Caplan, J. L. Stromule extension along microtubules coordinated with actin-mediated anchoring guides perinuclear chloroplast movement during innate immunity. *eLife* **2018**, *7*, e23625.

[49] Mullineaux, P. M.; Exposito-Rodriguez, M.; Laissue, P. P.; Smirnoff, N.; Park, E. Spatial chloroplast-to-nucleus signalling involving plastid nuclear complexes and stromules. *Philosophical Transactions of the Royal Society B: Biological Sciences* **2020**, *375*, 20190405.

[50] Haberlandt, G. *Die Chlorophyllkörper der Selaginellen*; Neubauer, 1888; pp 291–308.

[51] Senn, G. *Die Gestalts- und Lageveränderung der Pflanzen-Chromatophoren*; W. Engelmann, 1908.

[52] Köhler, R. H.; Cao, J.; Zipfel, W. R.; Webb, W. W.; Hanson, M. R. Exchange of Protein Molecules Through Connections Between Higher Plant Plastids. *Science* **1997**, *276*, 2039–2042.

[53] Hanson, M. R.; Hines, K. M. Stromules: Probing Formation and Function. *Plant Physiology* **2018**, *176*, 128–137.

[54] Metropolis, N.; Ulam, S. The Monte Carlo Method. *Journal of the American Statistical Association* **1949**, *44*, 335–341.

[55] Metropolis, N.; Rosenbluth, A. W.; Rosenbluth, M. N.; Teller, A. H.; Teller, E. Equation of State Calculations by Fast Computing Machines. *The Journal of Chemical Physics* **1953**, *21*, 1087–1092.

[56] Alder, B. J.; Wainwright, T. E. Phase Transition for a Hard Sphere System. *The Journal of Chemical Physics* **1957**, *27*, 1208–1209.

[57] Alder, B. J.; Wainwright, T. E. Studies in Molecular Dynamics. I. General Method. *The Journal of Chemical Physics* **1959**, *31*, 459–466.

[58] Corey, R. A.; Stansfeld, P. J.; Sansom, M. S. The energetics of protein–lipid interactions as viewed by molecular simulations. *Biochemical Society Transactions* **2019**, *48*, 25–37.

[59] Reynwar, B.; Illya, G.; Harmandaris, V.; Müller, M.; Kremer, K.; Deserno, M. Aggregation and vesiculation of membrane proteins by curvature-mediated interactions. *Nature* **2007**, *447*, 461–464.

[60] Nguyen, T. H.; Zhang, C.; Weichselbaum, E.; Knyazev, D. G.; Pohl, P.; Carloni, P. Interfacial water molecules at biological membranes: Structural features and role for lateral proton diffusion. *PLOS ONE* **2018**, *13*, 1–14.

[61] Bennett, W.; Sapay, N.; Tieleman, D. Atomistic Simulations of Pore Formation and Closure in Lipid Bilayers. *Biophysical journal* **2014**, *106*, 210–9.

[62] Huang, K.; Garcia, A. Free Energy of Translocating an Arginine-Rich Cell-Penetrating Peptide across a Lipid Bilayer Suggests Pore Formation. *Biophysical journal* **2013**, *104*, 412–20.

[63] Moiset, G.; Cirac, A. D.; Stuart, M. C. A.; Marrink, S.-J.; Sengupta, D.; Poolman, B. Dual Action of BPC194: A Membrane Active Peptide Killing Bacterial Cells. *PLoS ONE* **2013**, *8*.

[64] Dror, R. O.; Pan, A. C.; Arlow, D. H.; Borhani, D. W.; Maragakis, P.; Shan, Y.; Xu, H.; Shaw, D. E. Pathway and mechanism of drug binding to G-protein-coupled receptors. *Proceedings of the National Academy of Sciences* **2011**, *108*, 13118–13123.

[65] Maffeo, C.; Bhattacharya, S.; Yoo, J.; Wells, D.; Aksimentiev, A. Modeling and simulation of ion channels. *Chemical Reviews* **2012**, *112*, 6250–6284.

[66] Polley, A.; Vemparala, S.; Rao, M. Atomistic Simulations of a Multicomponent Asymmetric Lipid Bilayer. *The Journal of Physical Chemistry B* **2012**, *116*, 13403–13410.

[67] Gu, R.-X.; Baoukina, S.; Tieleman, D. P. Phase Separation in Atomistic Simulations of Model Membranes. *Journal of the American Chemical Society* **2020**, *142*, 2844–2856.

[68] Alimohamadi, H.; Rangamani, P. Modeling Membrane Curvature Generation due to Membrane-Protein Interactions. *Biomolecules* **2018**, *8*.

[69] Ramakrishnan, N.; Bradley, R. P.; Tourdot, R. W.; Radhakrishnan, R. Biophysics of membrane curvature remodeling at molecular and mesoscopic lengthscales. *Journal of Physics: Condensed Matter* **2018**, *30*, 273001.

[70] Marrink, S.; Corradi, V.; Souza, P.; Ingólfsson, H.; Tieleman, D.; Sansom, M. Computational Modeling of Realistic Cell Membranes. *Chemical reviews* **2019**, *119*, 6184–6226.

[71] Marrink, S. J.; de Vries, A. H.; Mark, A. E. Coarse Grained Model for Semiquantitative Lipid Simulations. *The Journal of Physical Chemistry B* **2004**, *108*, 750–760.

[72] Marrink, S. J.; Risselada, H. J.; Yefimov, S.; Tieleman, D. P.; de Vries, A. H. The MARTINI Force Field: Coarse Grained Model for Biomolecular Simulations. *The Journal of Physical Chemistry B* **2007**, *111*, 7812–7824.

[73] Simunovic, M.; Srivastava, A.; Voth, G. A. Linear aggregation of proteins on the membrane as a prelude to membrane remodeling. *Proceedings of the National Academy of Sciences* **2013**, *110*, 20396–20401.

[74] Noguchi, H. Membrane tubule formation by banana-shaped proteins with or without intermediate network structure. *Scientific Reports* **2015**, *6*.

[75] Tian, F.; Yue, T.; Dong, W.; Yi, X.; Zhang, X. Size-dependent formation of membrane nanotubes: continuum modeling and molecular dynamics simulations. *Phys. Chem. Chem. Phys.* **2018**, *20*, 3474–3483.

[76] Goetz, R.; Lipowsky, R. Computer simulations of bilayer membranes: Self-assembly and interfacial tension. *The Journal of Chemical Physics* **1998**, *108*, 7397–7409.

[77] Xu, R.; Wang, Z.-l.; He, X.-h. Mesoscale Simulation of Vesiculation of Lipid Droplets. *Chinese Journal of Chemical Physics* **2014**, *27*, 663–671.

[78] Meinhardt, S.; Vink, R. L. C.; Schmid, F. Monolayer curvature stabilizes nanoscale raft domains in mixed lipid bilayers. *Proceedings of the National Academy of Sciences* **2013**, *110*, 4476–4481.

[79] Lenz, O.; Schmid, F. Structure of Symmetric and Asymmetric "Ripple" Phases in Lipid Bilayers. *Phys. Rev. Lett.* **2007**, *98*, 058104.

[80] West, B.; Schmid, F. Fluctuations and elastic properties of lipid membranes in the gel Lβ' state: a coarse-grained Monte Carlo study. *Soft Matter* **2010**, *6*, 1275–1280.

[81] Noguchi, H. Solvent-free coarse-grained lipid model for large-scale simulations. *The Journal of Chemical Physics* **2011**, *134*, 055101.

[82] Yuan, H.; Huang, C.; Li, J.; Lykotrafitis, G.; Zhang, S. One-particle-thick, solvent-free, coarse-grained model for biological and biomimetic fluid membranes. *Phys. Rev. E* **2010**, *82*, 011905.

[83] Pasqua, A.; Maibaum, L.; Oster, G.; Fletcher, D. A.; Geissler, P. L. Large-scale simulations of fluctuating biological membranes. *The Journal of Chemical Physics* **2010**, *132*, 154107.

[84] Noguchi, H. Acceleration and suppression of banana-shaped-protein-induced tubulation by addition of small membrane inclusions of isotropic spontaneous curvatures. *Soft Matter* **2017**, *13*, 7771–7779.

[85] Fu, S.-P.; Peng, Z.; Yuan, H.; Kfoury, R.; Young, Y.-N. Lennard-Jones type pair-potential method for coarse-grained lipid bilayer membrane simulations in LAMMPS. *Computer Physics Communications* **2016**,

[86] Sadeghi, M.; Weikl, T. R.; Noé, F. Particle-based membrane model for mesoscopic simulation of cellular dynamics. *The Journal of Chemical Physics* **2018**, *148*, 044901.

[87] Weichsel, J.; Geissler, P. L. The More the Tubular: Dynamic Bundling of Actin Filaments for Membrane Tube Formation. *PLOS Computational Biology* **2016**, *12*, 1–13.

[88] Vierheller, J.; Neubert, W.; Falcke, M.; Gilbert, S.; Chamakuri, N. A multiscale computational model of spatially resolved calcium cycling in cardiac myocytes: from detailed cleft dynamics to the whole cell concentration profiles. *Frontiers in Physiology* **2015**, *6*, 255.

[89] Davtyan, A.; Simunovic, M.; Voth, G. A. The mesoscopic membrane with proteins (MesM-P) model. *The Journal of Chemical Physics* **2017**, *147*, 044101.

[90] Pezeshkian, W.; Hansen, A. G.; Johannes, L.; Khandelia, H.; Shillcock, J. C.; Kumar, P. B. S.; Ipsen, J. H. Membrane invagination induced by Shiga toxin B-subunit: from molecular structure to tube formation. *Soft Matter* **2016**, *12*, 5164–5171.

[91] Pezeshkian, W.; König, M.; Marrink, S. J.; Ipsen, J. H. A Multi-Scale Approach to Membrane Remodeling Processes. *Frontiers in Molecular Biosciences* **2019**, *6*, 59.

[92] Pezeshkian, W.; König, M.; Wassenaar, A. T.; Marrink, J. S. Backmapping triangulated surfaces to coarse-grained membrane models. *Nature communications* **2020**, *11*, 2296.

[93] Frenkel, D.; Smit, B. *Understanding molecular simulation : from algorithms to applications. 2nd ed*; 1996; Vol. 50.

[94] Swope, W. C.; Andersen, H. C.; Berens, P. H.; Wilson, K. R. A computer simulation method for the calculation of equilibrium constants for the formation of physical clusters of molecules: Application to small water clusters. **1982**, *76*, 637–649.

[95] Verlet, L. Computer "Experiments" on Classical Fluids. I. Thermodynamical Properties of Lennard-Jones Molecules. *Phys. Rev.* **1967**, *159*, 98–103.

[96] Langevin, P. Sur la théorie du mouvement brownien. *C. R. Acad. Sci.* **1908**, *146*, 530–533.

[97] Allen, M.; Tildesley, D. *Computer Simulation of Liquids*; Oxford Science Publ; Clarendon Press, 1989.

[98] Canham, P. The minimum energy of bending as a possible explanation of the biconcave shape of the human red blood cell. *Journal of Theoretical Biology* **1970**, *26*, 61 – 81.

[99] Helfrich, W. Elastic Properties of Lipid Bilayers: Theory and Possible Experiments. *Zeitschrift für Naturforschung* **1973**, *28C*, 693–703.

[100] Evans, E. A. Bending resistance and chemically induced moments in membrane bilayers. *Biophysical journal* **1974**, *14*, 923–931.

[101] Idema, T. *Physics of Life - IFF Spring School Lecture notes*; 2018; pp C1.3 – C.15.

[102] Carmo, M. D. *Differential Geometry of Curves and Surfaces*; Prentice Hall, 1976.

[103] Sheetz, M.; Singer, S. Biological membranes as bilayer couples. A molecular mechanism of drug-erythrocyte interactions. *Proceedings of the National Academy of Sciences of the United States of America* **1974**, *71*, 4457—4461.

[104] Svetina, S.; Zeks, B. Membrane bending energy and shape determination of phospholipid vesicles and red blood cells. *European biophysics journal : EBJ* **1989**, *17*, 101—111.

[105] Bozic, B.; Svetina, S.; Zeks, B.; Waugh, R. Role of lamellar membrane structure in tether formation from bilayer vesicles. *Biophysical journal* **1992**, *61*, 963—973.

[106] Wiese, W.; Harbich, W.; Helfrich, W. Budding of lipid bilayer vesicles and flat membranes. *Journal of Physics: Condensed Matter* **1992**, *4*, 1647–1657.

[107] Heinrich, V.; Svetina, S. c. v.; Žekš, B. c. v. Nonaxisymmetric vesicle shapes in a generalized bilayer-couple model and the transition between oblate and prolate axisymmetric shapes. *Phys. Rev. E* **1993**, *48*, 3112–3123.

[108] Miao, L.; Seifert, U.; Wortis, M.; Döbereiner, H.-G. Budding transitions of fluid-bilayer vesicles: The effect of area-difference elasticity. *Phys. Rev. E* **1994**, *49*, 5389–5407.

[109] Kantor, Y.; Nelson, D. R. Crumpling transition in polymerized membranes. *Phys. Rev. Lett.* **1987**, *58*, 2774–2777.

[110] Gompper, G.; Kroll, D. M. Network models of fluid, hexatic and polymerized membranes. *Journal of Physics: Condensed Matter* **1997**, *9*, 8795–8834.

[111] Jülicher, F. The morphology of vesicles of higher topological genus: conformal degeneracy and conformal modes. *Journal de Physique II* **1996**, *6*, 1797–1824.

[112] Bian, X.; Litvinov, S.; Koumoutsakos, P. Bending models of lipid bilayer membranes: Spontaneous curvature and area-difference elasticity. *Computer Methods in Applied Mechanics and Engineering* **2020**, *359*, 112758.

[113] Bahrami, A. H.; Hummer, G. Formation and Stability of Lipid Membrane Nanotubes. *ACS Nano* **2017**, *11*, 9558–9565.

[114] Hoore, M.; Yaya, F.; Podgorski, T.; Wagner, C.; Gompper, G.; Fedosov, D. A. Effect of spectrin network elasticity on the shapes of erythrocyte doublets. *Soft Matter* **2018**, *14*, 6278–6289.

[115] Ramakrishnan, N.; Sunil Kumar, P.; Ipsen, J. H. Membrane-Mediated Aggregation of Curvature-Inducing Nematogens and Membrane Tubulation. *Biophysical Journal* **2013**, *104*, 1018–1028.

[116] Bahrami, A. H.; Lipowsky, R.; Weikl, T. R. Tubulation and Aggregation of Spherical Nanoparticles Adsorbed on Vesicles. *Phys. Rev. Lett.* **2012**, *109*, 188102.

[117] Li, B.; Abel, S. M. Shaping membrane vesicles by adsorption of a semiflexible polymer. *Soft Matter* **2018**, *14*, 185–193.

[118] Šarić, A.; Cacciuto, A. Mechanism of Membrane Tube Formation Induced by Adhesive Nanocomponents. *Phys. Rev. Lett.* **2012**, *109*, 188101.

[119] Vahid, A.; Šarić, A.; Idema, T. Curvature variation controls particle aggregation on fluid vesicles. *Soft Matter* **2017**, *13*, 4924–4930.

[120] Sunil Kumar, P. B.; Gompper, G.; Lipowsky, R. Budding Dynamics of Multicomponent Membranes. *Phys. Rev. Lett.* **2001**, *86*, 3911–3914.

[121] Noguchi, H.; Gompper, G. Fluid Vesicles with Viscous Membranes in Shear Flow. *Phys. Rev. Lett.* **2004**, *93*, 258102.

[122] Noguchi, H.; Gompper, G. Dynamics of fluid vesicles in shear flow: Effect of membrane viscosity and thermal fluctuations. *Phys. Rev. E* **2005**, *72*, 011901.

[123] Euler, L. *Novi Commentarii academiae scientiarum Petropolitanae* **1758**, *4*, 109–140.

[124] G. Gompper,; D.M. Kroll, Random Surface Discretizations and the Renormalization of the Bending Rigidity. *J. Phys. I France* **1996**, *6*, 1305–1320.

[125] Itzykson, C.; Abad, J.; Asorey, M.; Cruz, A. Proceedings of the GIFT seminar, Jaca 85. **1986**,

[126] Rawicz, W.; Olbrich, K.; McIntosh, T.; Needham, D.; Evans, E. Effect of Chain Length and Unsaturation on Elasticity of Lipid Bilayers. *Biophysical Journal* **2000**, *79*, 328 – 339.

[127] Stillinger, F. H.; Weber, T. A. Computer simulation of local order in condensed phases of silicon. *Phys. Rev. B* **1985**, *31*, 5262–5271.

[128] Brünger, A.; Brooks, C. L.; Karplus, M. Stochastic boundary conditions for molecular dynamics simulations of ST2 water. *Chemical Physics Letters* **1984**, *105*, 495 – 500.

[129] Ahrens, J.; Geveci, B.; Law, C. ParaView: An End-User Tool for Large-Data Visualization. The Visualization Handbook. 2005.

[130] Seifert, U.; Lipowsky, R. Morphology of vesicles. *Structure and Dynamics of Membranes* **1995**, *1*, 403–463.

[131] Bo, L.; Waugh, R. Determination of bilayer membrane bending stiffness by tether formation from giant, thin-walled vesicles. *Biophysical journal* **1989**, *55 3*, 509–17.

[132] Laplace, P. *Méchanique céleste - Suppl. to the 10th edition*; 1806.

[133] Young, T. An essay on the cohesion of fluids. *Phil. Trans. R. Soc. Lond.* **1805**, *95*, 65–87.

[134] Diamant, H. Model-free thermodynamics of fluid vesicles. *Phys. Rev. E* **2011**, *84*, 061123.

[135] Powers, T. R.; Huber, G.; Goldstein, R. E. Fluid-membrane tethers: Minimal surfaces and elastic boundary layers. *Phys. Rev. E* **2002**, *65*, 041901.

[136] Deuling, H.; Helfrich, W. The curvature elasticity of fluid membranes : A catalogue of vesicle shapes. *J. Phys. France* **1976**, *37*, 1335–1345.

[137] Deuling, H.; Helfrich, W. Red blood cell shapes as explained on the basis of curvature elasticity. *Biophysical Journal* **1976**, *16*, 861 – 868.

[138] Bozic, B.; Svetina, S.; Zeks, B. Theoretical analysis of the formation of membrane microtubes on axially strained vesicles. *Phys. Rev. E* **1997**, *55*, 5834–5842.

[139] Jülicher, F.; Seifert, U. Shape equations for axisymmetric vesicles: A clarification. *Phys. Rev. E* **1994**, *49*, 4728–4731.

[140] Zhong-can, O.-Y.; Helfrich, W. Bending energy of vesicle membranes: General expressions for the first, second, and third variation of the shape energy and applications to spheres and cylinders. *Phys. Rev. A* **1989**, *39*, 5280–5288.

[141] Deuling, H.; Helfrich, W. Phase diagrams and shape transformations of toroidal vesicles. *J. Phys. II France* **1993**, *3*, 1681–1705.

[142] Luke, J. C. A Method for the Calculation of Vesicle Shapes. *SIAM Journal on Applied Mathematics* **1982**, *42*, 333–345.

[143] Mathews, J. Axisymetrical equilibrium shapes of two-phase biologicalmembranes. M.Sc. thesis, University of Warwick, 2012.

[144] Jian-Guo, H.; Zhong-Can, O.-Y. Shape equations of the axisymmetric vesicles. *Phys. Rev. E* **1993**, *47*, 461–467.

[145] Jenkins, J. Static equilibrium configurations of a model red blood cell. *Journal of mathematical biology* **1977**, *4*, 149–69.

[146] Shibuya, A.; Saito, Y.; Hyuga, H. Morphology of Axisymmetric Vesicles with Encapsulated Filaments and Impurities. *Journal of the Physical Society of Japan* **2002**, *71*, 1780–1788.

[147] Wu, Z.; Yuan, H.; Zhang, X.; Yi, X. Sidewall contact regulating the nanorod packing inside vesicles with relative volumes. *Soft Matter* **2019**, *15*, 2552–2559.

[148] Yi, X.; Zou, G.; Gao, H. Mechanics of cellular packing of nanorods with finite and non-uniform diameters. *Nanoscale* **2018**, *10*, 14090–14099.

[149] Gozdz, W. Influence of Spontaneous Curvature and Microtubules on the Conformations of Lipid Vesicles. *The journal of physical chemistry. B* **2005**, *109*, 21145–9.

[150] Chen, J. Pulling or compressing a vesicle by force: Solution to the bending energy model. *Physical Review E* **2012**, *85*.

[151] Seifert, U.; Berndl, K.; Lipowsky, R. Shape transformations of vesicles: Phase diagram for spontaneous- curvature and bilayer-coupling models. *Phys. Rev. A* **1991**, *44*, 1182–1202.

[152] Blyth, M.; Pozrikidis, C. Solution space of axisymmetric capsules enclosed by elastic membranes. *European Journal of Mechanics - A/Solids* **2004**, *23*, 877 – 892.

[153] Smith, A.-S. c. v.; Sackmann, E.; Seifert, U. Pulling Tethers from Adhered Vesicles. *Phys. Rev. Lett.* **2004**, *92*, 208101.

[154] Heinrich, V.; Božič, B.; Svetina, S.; Žekš, B. Vesicle Deformation by an Axial Load: From Elongated Shapes to Tethered Vesicles. *Biophysical Journal* **1999**, *76*, 2056 – 2071.

[155] Umeda, T.; Nakajima, H.; Hotani, H. Theoretical Analysis of Shape Transformations of Liposomes Caused by Microtubule Assembly. *Journal of the Physical Society of Japan* **1998**, *67*, 682–688.

[156] Inc., W. R. Mathematica, Version 11.1. `https://www.wolfram.com/mathematica`, Champaign, IL, 2017.

[157] Runge, C. Ueber die numerische Auflösung von Differentialgleichungen. *Mathematische Annalen* **1895**, *46*, 167–178.

[158] Kutta, W. Beitrag zur näherungsweisen Integration totaler Differentialgleichungen. *Zeit. Math. Phys.* **1901**, *46*, 435–53.

[159] Goldstine, H. H. *A History of the Calculus of Variations from the 17th through the 19th Century*; Springer-Verlag: New York, 1980.

[160] E., B. A. Optimal Control—1950 to 1985. *IEEE Control Systems Magazine* **1996**, *16*, 26–33.

[161] Houska, B.; Ferreau, H.; Diehl, M. ACADO Toolkit – An Open Source Framework for Automatic Control and Dynamic Optimization. *Optimal Control Applications and Methods* **2011**, *32*, 298–312.

[162] Houska, B.; Ferreau, H.; Vukov, M.; Quirynen, R. ACADO Toolkit User's Manual. http://www.acadotoolkit.org, 2009–2013.

[163] Cuvelier, D.; Derényi, I.; Bassereau, P. Coalescence of Membrane Tethers: Experiments, Theory, and Applications. *Biophysical journal* **2005**, *88*, 2714–26.

[164] Li, S.; Yan, Z.; Luo, Z.; Xu, Y.; Huang, F.; Zhang, X.; Yi, X.; Yue, T. Mechanics of the Formation, Interaction, and Evolution of Membrane Tubular Structures. *Biophysical Journal* **2019**, *116*, 884 – 892.

[165] Stephens, D. J. Functional coupling of microtubules to membranes – implications for membrane structure and dynamics. *Journal of Cell Science* **2012**, *125*, 2795–2804.

[166] Heinrich, M.; Tian, A.; Esposito, C.; Baumgart, T. Dynamic sorting of lipids and proteins in membrane tubes with a moving phase boundary. *Proceedings of the National Academy of Sciences* **2010**, *107*, 7208–7213.

[167] Dasgupta, R.; Dimova, R. Inward and outward membrane tubes pulled from giant vesicles. *Journal of Physics D* **2014**, *47*, 282001.

[168] Prevost, C.; Zhao, H.; Manzi, J.; Lemichez, E.; Lappalainen, P.; Callan-Jones, A.; Bassereau, P. IRSp53 senses negative membrane curvature and phase separates along membrane tubules. *Nature Communications* **2015**, *6*.

[169] Gompper, G.; Kroll, D. M. Phase diagram and scaling behavior of fluid vesicles. *Phys. Rev. E* **1995**, *51*, 514–525.

[170] Koster, G.; Cacciuto, A.; Derényi, I.; Frenkel, D.; Dogterom, M. Force Barriers for Membrane Tube Formation. *Phys. Rev. Lett.* **2005**, *94*, 068101.

[171] Golushko, I.; Rochal, S. Tubular lipid membranes pulled from vesicles: Dependence of system equilibrium on lipid bilayer curvature. *Journal of Experimental and Theoretical Physics* **2016**, *122*, 169–175.

[172] Powers, R. E.; Wang, S.; Liu, T. Y.; Rapoport, T. A. Reconstitution of the tubular endoplasmic reticulum network with purified components. *Nature* **2017**, *543*, 257.

[173] Inaba, T.; Ishijima, A.; Honda, M.; Nomura, F.; Takiguchi, K.; Hotani, H. Formation and Maintenance of Tubular Membrane Projections Require Mechanical Force, but their Elongation and Shortening do not Require Additional Force. *Journal of molecular biology* **2005**, *348*, 325–33.

[174] Sonek, P. Simulation doppelwandiger Membranvesikel. Bachelor's Thesis, University of Mainz, Mainz, Germany, 2019.

[175] Sauber, S. Movement of fluorescently labeled organelles in Arabidopsis thaliana roots using light-sheet based fluorescence microscopy. M.Sc. thesis, Goethe University, Frankfurt am Main, 2016.

[176] Schleiff, E. personal communication, 2018, Goethe University, Frankfurt am Main, Germany.

[177] Montroll, E. W.; Weiss, G. H. Random Walks on Lattices. II. *Journal of Mathematical Physics* **1965**, *6*, 167–181.

[178] Ramer, U. An iterative procedure for the polygonal approximation of plane curves. *Computer Graphics and Image Processing* **1972**, *1*, 244 – 256.

[179] Douglas, D.; Peucker, T. Algorithms for the reduction of the number of points required for represent a digitzed line or its caricature. *Canadian Cartographer* **1973**, *10*.